

# Cutting Mechanics of the Gear Shaping Process

by

Andrew Katz

A thesis

presented to the University of Waterloo

in fulfillment of the

thesis requirement for the degree of

Master of Applied Science

in

Mechanical and Mechatronics Engineering

Waterloo, Ontario, Canada, 2017

© Andrew Katz 2017

## **AUTHOR'S DECLARATION**

I hereby declare that I am the sole author of this thesis. This is a true copy of the thesis, including any required final revisions, as accepted by my examiners.

I understand that my thesis may be made electronically available to the public.

## Abstract

In the machining industry, there is a constant need to increase productivity while also maintaining dimensional tolerances and good surface quality. For many classical machining operations (e.g. milling, turning, and broaching), research has been established that is able to predict the part quality based on process parameters, workpiece material, and the machine's dynamic characteristics. This allows process planners to design their programs virtually to maximize productivity while meeting the specified part quality. To accomplish this, it is necessary to predict the cutting forces during the machining operation. This can be done using analytical equations for a lot of operations; however, in more recent research for complicated processes (e.g. 5-axis milling, gear hobbing), this is done by calculating the cutter-workpiece engagement with geometric CAD modellers and calculating incremental cutting forces along the cutting edge. With knowledge of the cutting forces, static deflections and dynamic vibrations of the tool and workpiece can be calculated which is one of the most prominent contributors to dimensional part inaccuracies and poor surface quality in machining. The research presented in this thesis aims to achieve similar goals for the gear shaping process.

Gear shaping is one of the most prominent methods of machining cylindrical gears. More specifically, it is the most prominent method for generating internal gears which are a major component in planetary gear boxes. The gear shaping process uses a modified external gear as a cutting tool which reciprocates up and down to cut the teeth in the workpiece. Simultaneously, the tool and workpiece are also rotating proportionally to their gear ratio which emulate the rolling of two gears. During the beginning of each gear shaping pass, the tool is radially fed into the workpiece until the desired depth of cut is reached. In this study, the three kinematic components (reciprocating feed, rotary feed, and radial feed) are mathematically modelled using analytical equations and experimentally verified using captured CNC signals from the controller of a Liebherr LSE500 gear shaping machine.

To predict cutting forces in gear shaping, the cutter-workpiece engagement (CWE) is calculated at discrete time steps using a discrete solid modeller called ModuleWorks. From the CWE in dextral form, the two-dimensional chip geometry is reconstructed using Delaunay triangulation and alpha shape reconstruction which is then used to determine the undeformed chip area along the cutting edge. The cutting edge is discretized into nodes with varying cutting directions (tangential, feed, and radial), inclination angle, and rake angle. If engaged in cutting during a time step, each node contributes an incremental three dimensional force vector calculated with the oblique cutting force model. Using a 3-axis dynamometer, the cutting force

prediction algorithm was experimentally verified on a variety of processes and gears which included an internal spur gear, external spur gear, and external helical gear. The simulated and measured force profiles correlate very closely (about 3-10% RMS error) with the most error occurring in the external helical gear case. These errors may be attributable due to rubbing of the tool which is evident through visible gouges on the finished workpiece, tool wear on the helical gear shaper, and different cutting speed than the process for which the cutting coefficients were calibrated. More experiments are needed to verify the sources of error in the helical gear case.

To simulate elastic tool deflection in gear shaping, the tool's static stiffness is estimated from impact hammer testing. Then, based on the predicted cutting force, the elastic deflection of the tool is calculated at each time step. To examine the affect of tool deflection on the final quality of the gear, a virtual gear measurement module is developed and used to predict the involute profile deviations in the virtually machined part. Simulated and measured profile deviations were compared for a one-pass external spur gear process and a two-pass external spur gear process. The simulated profile errors correlate very well with the measured profiles on the left flank of the workpiece, however additional research is needed to improve the accuracy of the model on the right flank. Furthermore, the model also serves as a basis for future research in dyamic vibrations in gear shaping.

The above-mentioned algorithms have been implemented into a tool called ShapePRO (developed in C++). The software is meant for process planners to be able to simulate the gear shaping operation virtually and inspect the resulting quality of the gear. Accordingly, the user may iterate the process parameters to maximize productivity while meeting the customer's desired gear quality.

## **Acknowledgements**

I would like to thank my supervisors Professor Kaan Erkorkmaz and Professor Fathy Ismail for their continuous support, ideas, and enthusiasm during my studies. Their knowledge and guidance have been pivotal in my ability to reach my research goals.

I would like to thank Ontario Drive and Gear (Jamie McPherson, Bob Reiter, Jacob Van Dorp, Sash Rakanovic, and everyone else) who has graciously sponsored this project and provided invaluable resources such as machine time at their facility, material, tools, and general knowledge which has been essential in the success of the research.

I would also like to thank the MME technical staff, particularly Robert Wagner and Jason Benninger, for their assistance with experimental setups.

Finally, I would like to thank all my colleagues from the Precision Controls Laboratory, my friends, and my family for their continuous support during my degree.

## **Dedication**

To my parents.

## Table of Contents

<b>List of Figures.....</b>	<b>x</b>
<b>List of Tables .....</b>	<b>xiv</b>
<b>Nomenclature .....</b>	<b>xv</b>
<b>Chapter 1 Introduction.....</b>	<b>1</b>
1.1 Gear Shaping.....	1
1.2 Thesis Objectives .....	1
1.3 Thesis Layout.....	2
<b>Chapter 2 Literature Review .....</b>	<b>4</b>
2.1 Introduction.....	4
2.2 Classical Machining Literature .....	4
2.3 Gear Machining Literature .....	6
2.3.1 Gear Hobbing.....	6
2.3.2 Gear Shaping.....	8
2.4 Conclusions.....	9
<b>Chapter 3 Kinematics of Gear Shaping .....</b>	<b>10</b>
3.1 Introduction.....	10
3.2 Gear Terminology .....	11
3.3 Cutter and Workpiece Geometry .....	14
3.4 Kinematics .....	16
3.4.1 Coordinate Systems .....	16
3.4.2 Reciprocating Motion .....	18
3.4.3 Rotary Feed Motion .....	19
3.4.4 Radial Feed Motion .....	20
3.5 Experimental Validation .....	23
3.6 Conclusions.....	27
<b>Chapter 4 Cutting Force Prediction.....</b>	<b>28</b>
4.1 Introduction.....	28
4.2 Cutting Force Models.....	28
4.2.1 Orthogonal .....	28
4.2.2 Oblique.....	29

4.2.3 Orthogonal to Oblique .....	30
4.2.4 Exponential Chip Thickness .....	31
4.2.5 Kienzle .....	32
4.2.6 Generalized Model.....	32
4.3 Cutter-Workpiece Engagement.....	33
4.3.1 Multi-Dexel Representation.....	33
4.3.2 Material Removal Simulation .....	34
4.4 Tool Edge Discretization .....	35
4.4.1 Rake Face Model .....	36
4.4.2 Cutting Direction Calculation .....	40
4.5 Force Calculation .....	46
4.6 Experimental Validation .....	51
4.6.1 Experimental Setup.....	54
4.6.2 Cutting Coefficient Determination .....	55
4.6.3 Results.....	62
4.7 Conclusions.....	84
<b>Chapter 5 Elastic Deformation and Form Error Prediction .....</b>	<b>86</b>
5.1 Introduction.....	86
5.2 Elastic Deformation Model.....	86
5.2.1 Impact Hammer Testing .....	87
5.2.2 Deflection Calculation .....	92
5.3 Virtual Gear Measurement.....	93
5.3.1 Experimental Validation .....	95
5.4 Conclusions.....	106
<b>Chapter 6 ShapePRO Software .....</b>	<b>107</b>
6.1 Introduction.....	107
6.2 User Workflow.....	108
6.3 Virtual Gear Measurement.....	112
<b>Chapter 7 Conclusions and Future Work.....</b>	<b>113</b>
7.1 Conclusions.....	113
7.2 Future Work.....	114



**Bibliography ..... 115**

## List of Figures

Figure 1.1: Gear shaping process.....	1
Figure 2.1: 2D dynamic analysis in milling (from [27]).....	6
Figure 2.2: Cutting force prediction in HOB3D (from [39]).....	7
Figure 2.3: Influence of tool tip width and chip cross-section on tool wear (from [50]).....	9
Figure 3.1: Kinematic components in gear shaping.....	10
Figure 3.2: Transverse plane and normal plane in spur and helical gears. ....	12
Figure 3.3: Basic gear geometry .....	12
Figure 3.4: Gear tooth profile shift. ....	14
Figure 3.5: Gear shaper relief angles. ....	15
Figure 3.6: Comparison of spur gear shaper (from [56]) and helical gear shaper (from [57]). ....	15
Figure 3.7: Coordinate systems in gear shaping. ....	17
Figure 3.8: Reciprocating motion kinematics .....	18
Figure 3.9: Slider-crank vs pure sinusoidal motion. ....	19
Figure 3.10: Comparison of constant acceleration and linear acceleration infeed profiles. ....	22
Figure 3.11: Liebherr LSE500 Machine (from [59]). ....	24
Figure 3.12: Liebherr LSE500 Axes Labels (from [60]). ....	25
Figure 3.13: Position, velocity, and acceleration profiles of X1 axis during infeed.....	26
Figure 3.14: Comparison of simulated and captured X1, C1, C2, and ZL3 profiles. ....	27
Figure 4.1: Orthogonal cutting model.....	29
Figure 4.2: Oblique cutting model. ....	30
Figure 4.3: Single direction and two direction dixel representation of a circle (from [66]).....	34
Figure 4.4: Tool and workpiece representation in ModuleWorks engine.....	34
Figure 4.5: Cutter-workpiece engagement.....	35
Figure 4.6: Rake face model in spur gear shaping.....	36
Figure 4.7: Projection of transverse nodes onto rake face. ....	37
Figure 4.8: Rake face model in helical gear shaping. ....	38
Figure 4.9: Illustration of tooth angle ( $\gamma$ ). ....	39
Figure 4.10: Cutting velocity and directions in spur and helical shaping.....	41
Figure 4.11: Cutting direction calculation. ....	43
Figure 4.12: Local approximation of normal rake angle for curved rake face.....	45

Figure 4.13: Distribution of inclination and rake angles on single gear tooth with cutter rake angle of $5^\circ$ and helical angle of $25^\circ$ in helical gear shaper case. ....	46
Figure 4.14: Typical chip geometry in helical gear shaping case. ....	47
Figure 4.15: Reconstruction of two-dimensional chip cross-section. ....	48
Figure 4.16: Projection of triangles onto plane normal to tangential direction. ....	50
Figure 4.17: Finished workpiece (left) and tool (right) for internal spur gear case study. ....	53
Figure 4.18: Finished workpiece (left) and tool (right) for external spur gear case study. ....	53
Figure 4.19: Finished workpiece (left) and tool (right) for external helical gear case study. ....	53
Figure 4.20: Experimental setup for spur internal gear case. ....	54
Figure 4.21: Experimental setup for external gear cases. ....	55
Figure 4.22: Cubic search for shear stress, friction angle, shear angle. ....	56
Figure 4.23: Error contour plot for AISI 1141 steel at $\tau = 805.6$ [N/mm <sup>2</sup> ]. ....	58
Figure 4.24: Error contour plot for AISI 5130 steel at $\tau = 764.1$ [N/mm <sup>2</sup> ]. ....	58
Figure 4.25: Error contour plot for AISI 8620 steel at $\tau = 633.3$ [N/mm <sup>2</sup> ]. ....	59
Figure 4.26: Exponential chip model for AISI 1141 steel. ....	61
Figure 4.27: Exponential chip model for AISI 5130 steel. ....	61
Figure 4.28: Exponential chip model for AISI 8620 steel. ....	62
Figure 4.29: Comparison of simulated and measured cutting forces for internal spur gear, one-pass, AISI 1141 steel process. ....	64
Figure 4.30: Comparison of simulated and measured cutting forces for internal spur gear, one-pass, AISI 1141 steel process, zoomed in. ....	65
Figure 4.31: Comparison of simulated and measured cutting forces for internal spur gear, two-pass, AISI 1141 steel process. ....	67
Figure 4.32: Comparison of simulated and measured cutting forces for internal spur gear, two-pass, AISI 1141 steel process, zoomed in. ....	68
Figure 4.33: Comparison of simulated and measured cutting forces for internal spur gear, one-pass, AISI 5130 steel process. ....	69
Figure 4.34: Comparison of simulated and measured cutting forces for internal spur gear, one-pass, AISI 5130 steel process, zoomed in. ....	70
Figure 4.35: Comparison of simulated and measured cutting forces for internal spur gear, two-pass, AISI 5130 steel process. ....	71

Figure 4.36: Comparison of simulated and measured cutting forces for internal spur gear, two-pass, AISI 5130 steel process, zoomed in.....	72
Figure 4.37: Comparison of simulated and measured cutting forces for external spur gear, one-pass, AISI 8620 steel process. ....	74
Figure 4.38: Comparison of simulated and measured cutting forces for external spur gear, one-pass, AISI 8620 steel process, zoomed in.....	75
Figure 4.39: Comparison of simulated and measured cutting forces for external spur gear, two-pass, AISI 8620 steel process. ....	77
Figure 4.40: Comparison of simulated and measured cutting forces for external spur gear, two-pass, AISI 8620 steel process, zoomed in.....	78
Figure 4.41: Comparison of simulated and measured cutting forces for external helix gear, one-pass, AISI 8620 steel process. ....	80
Figure 4.42: Comparison of simulated and measured cutting forces for external helix gear, one-pass, AISI 8620 steel process, zoomed in.....	81
Figure 4.43: Gouges and scraping as seen on the finished external helix gear, one-pass process.....	82
Figure 4.44: Comparison of simulated and measured cutting forces for external helix gear, two-pass, AISI 8620 steel process. ....	83
Figure 4.45: Comparison of simulated and measured cutting forces for external helix gear, two-pass, AISI 8620 steel process, zoomed in.....	84
Figure 5.1: Elastic deformation of cutting tool due to cutting forces. ....	87
Figure 5.2: Measured and fit receptance FRF of the 5.08 module spur gear shaper.....	89
Figure 5.3: Measured and fit receptance FRF of the workpiece. ....	91
Figure 5.4: Scanning measurement of gears. ....	94
Figure 5.5: Profile errors in gear inspection. ....	95
Figure 5.6: Pitch deviation in gear inspection.....	95
Figure 5.7: Leading/left and Trailing/right flank in gear shaping.....	96
Figure 5.8: Comparison of measured and simulated profile deviations in external spur gear, one-pass process (Teeth 1-8). ....	98
Figure 5.9: Comparison of measured and simulated profile deviations in external spur gear, one-pass process (Teeth 9-16). ....	99

Figure 5.10: Comparison of measured and simulated profile deviations in external spur gear, one-pass process (Teeth 17-22). .....	100
Figure 5.11: Measured and simulated profile error metrics in external spur gear, one-pass process. ....	101
Figure 5.12: Comparison of measured and simulated profile deviations in external spur gear, two-pass process (Teeth 1-8). .....	102
Figure 5.13: Comparison of measured and simulated profile deviations in external spur gear, two-pass process (Teeth 9-16). .....	103
Figure 5.14: Comparison of measured and simulated profile deviations in external spur gear, two-pass process (Teeth 17-22). .....	104
Figure 5.15: Measured and simulated profile error metrics in external spur gear, two-pass process. ....	105
Figure 6.1: ShapePRO software main screen.....	107
Figure 6.2: ShapePRO workpiece configuration dialog. ....	108
Figure 6.3: ShapePRO material configuration dialog.....	109
Figure 6.4: ShapePRO tool configuration dialog.....	110
Figure 6.5: ShapePRO machine configuration dialog.....	111
Figure 6.6: ShapePRO process configuration dialog. ....	111
Figure 6.7: ShapePRO virtual gear measurement module.....	112

## List of Tables

Table 3.1: Cutting pass radial distances.....	20
Table 3.2: Cutting pass parameters and gear data for kinematic experimental validation.....	25
Table 4.1: Cutting pass parameters and gear data for internal spur case study.....	52
Table 4.2: Cutting pass parameters and gear data for external spur case study.....	52
Table 4.3: Cutting pass parameters and gear data for external helical case study.....	52
Table 4.4: Identified orthogonal to oblique coefficients.....	57
Table 4.5: Identified orthogonal exponential chip thickness coefficients.....	60
Table 4.6: RMS error for internal spur gear, one-pass, AISI 1141 steel process.....	63
Table 4.7: RMS error for internal spur gear, two-pass, AISI 1141 steel process.....	66
Table 4.8: RMS error for internal spur gear, one-pass, AISI 5130 steel process.....	69
Table 4.9: RMS error for internal spur gear, two-pass, AISI 5130 steel process.....	71
Table 4.10: RMS error for external spur gear, one-pass, AISI 8620 steel process.....	73
Table 4.11: RMS error for external spur gear, two-pass, AISI 8620 steel process.....	76
Table 4.12: RMS error for external helix gear, one-pass, AISI 8620 steel process.....	79
Table 4.13: RMS error for external helix gear, two-pass, AISI 8620 steel process.....	82
Table 5.1: Fit modes and static stiffness in $x$ direction of 5.08 module spur gear shaper.....	90
Table 5.2: Fit modes and static stiffness in $y$ direction of 5.08 module spur gear shaper.....	90
Table 5.3: Fit modes and static stiffness in $x$ direction of workpiece.....	92
Table 5.4: Fit modes and static stiffness in $y$ direction of workpiece.....	92

## Nomenclature

<u>Symbol</u>	<u>Definition</u>	<u>Units</u>
$\alpha$	Rake angle	°
$\alpha_n$	Normal rake angle	°
$a$	Undeformed chip area	mm <sup>2</sup>
$a_{\text{infeed}}$	Linear acceleration during infeed	mm/s <sup>2</sup>
$\beta$	Helix angle / friction angle	°
$b$	Gear face width / undeformed chip width	mm
$d_{p,b,a,d}$	Pitch / base / addendum / dedendum diameter	mm
$d_{\text{stroke}}$	Stroke length	mm
$d_{\text{top/bottom}}$	Tool top / bottom overrun length	
$\epsilon$	Gear type modification factor (+1 for external, -1 for internal)	
$f_{\text{cut}}$	Cutting stroke frequency	DS/min
$f_{\text{rotary}}$	Rotary feedrate	mm/DS
$f_{\text{radial}}$	Radial feedrate	mm/DS
$h$	Undeformed chip thickness	mm
$h_c$	Deformed chip thickness	mm
$h_{a,d}$	Addendum / dedendum height	
$i$	Inclination angle	°
$\eta$	Chip flow angle	°
$K_{x,y}$	Static tool stiffness in x / y direction	N/μm
$K_{tc}, K_{fc}, K_{rc}$	Cutting coefficients for orthogonal/oblique force model	N/mm <sup>2</sup>
$K_{te}, K_{fe}, K_{re}$	Edge coefficients for orthogonal/oblique force model	N/mm
$K_t, K_f, K_r, (p, q, r)$	Cutting coefficients for exponential chip thickness force model	N/mm <sup>2</sup> ( )
$K_u, K_v, (u, v)$	Cutting coefficients for Kienzle force model	N/mm <sup>2</sup> ( )
$m_{n/t}$	Normal / transverse module	mm
$N_{c,g}$	Number of teeth in cutter/gear	

$\psi_{n/t}$	Normal / transverse pressure angle	°
$R$	Gear ratio	
$r$	Radius / center-to-center distance	mm
$r_c$	Chip ratio	
$r_{p,b,a,d}$	Pitch / base / addendum / dedendum radius	mm
$r_{scrape}$	Scrape distance between tool and workpiece	mm
$r_{gc}$	Nominal center-to-center distance between tool and workpiece	mm
$s_p$	Circular tooth thickness at pitch diameter	mm
$\Delta$	Area of a triangle	mm <sup>2</sup>
$t_{infeed}$	Amount of time required for tool infeed	s
$t_{pass}$	Amount of time required for entire shaping pass	s
$\phi_{c,g}$	Cutter / gear rotation about z axis in machine coordinate system	rad
$\phi_{cg}$	Relative rotation between cutter and gear	rad
$V_c$	Cutting velocity	mm/s
$v_r$	Linear velocity during infeed	mm/s
$\omega_s$	Cutting stroke frequency	rad/s
$\omega_{c,g}$	Cutter/gear angular velocity about z axis	rad/s
$\omega_{cg}$	Relative angular velocity between cutter and gear	rad/s
$x$	Profile modification factor	
$z$	Vertical distance between bottom of tool and top of workpiece	mm



# Chapter 1

## Introduction

### 1.1 Gear Shaping

Gear shaping is one of the prominent methods of manufacturing cylindrical gears. It is a generating process which uses a modified cylindrical gear as a tool that axially reciprocates up and down to cut the teeth in the workpiece (shown in Figure 1.1). The cutter and workpiece continuously rotate during the cutting action which simulate the rolling of two gears and, at the beginning of the process, the cutter is radially fed into the workpiece until it reaches the final depth of cut. Compared to gear hobbing (which uses a worm gear cutter), gear shaping is generally not as productive, however is more versatile [1]. For example, gear hobbing is unable to generate internal gears or gears with geometric constraints which would interfere with a gear hob. Furthermore, gear shaping may be used as a finishing operation of hardened gears [2]. Therefore, it is important to have an understanding of the physics of the operation to improve productivity and the quality of the machined gears.

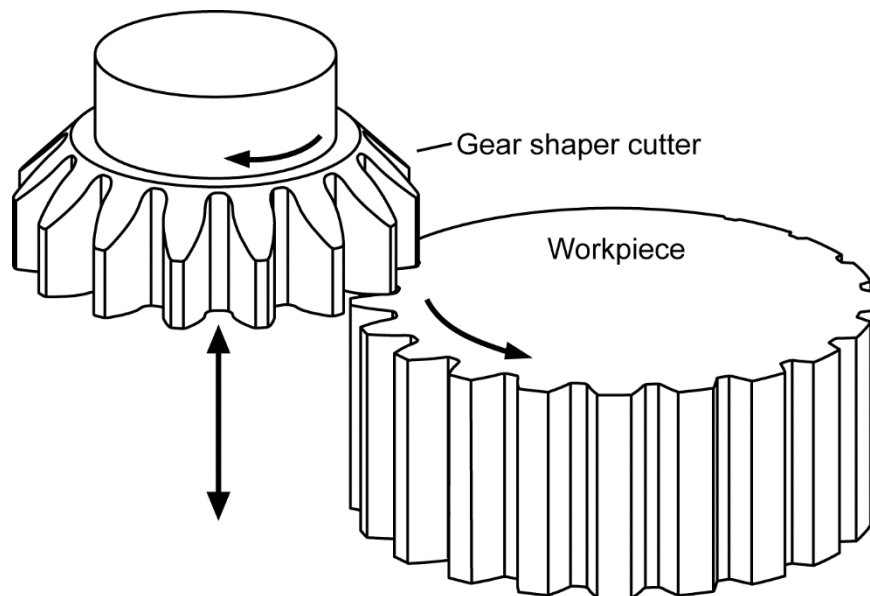


**Figure 1.1:** Gear shaping process.

### 1.2 Thesis Objectives

The objective of this thesis is to conduct research in the cutting mechanics of gear shaping which will serve as a basis for machining simulation tools that allow process planners to optimize their programs.

Specifically, the goal is to develop a virtual model of the gear shaping process which is capable of predicting the three-dimensional chip geometry, cutting forces, static tool/workpiece deflections, and vibrations.

### **1.3 Thesis Layout**

In Chapter 2, a literature review is presented on existing research in general and gear machining. In classical machining operations (such as turning, milling, and drilling), chip geometry and cutting forces can be calculated using analytical expressions. Furthermore, there exists thorough research in elastic tool deflections and dynamic (chatter) vibrations in these operations, which allow for accurate prediction of machined part quality. This allows for process planners to design their programs to maximize material removal rate while maintaining a specified part quality and avoiding chatter vibrations that would otherwise lead to premature tool wear/breakage. However, due to the complex kinematics and complicated cutter/workpiece geometries in gear shaping, there is a lack of research of the cutting mechanics in gear shaping, which has been the main motivation of this thesis.

The kinematics of the gear shaping are mathematically described in Chapter 3. Gears are normally manufactured in two to three passes; at least one roughing and one finishing pass. Each pass is defined by its cutting frequency (reciprocating motion), rotary feed (rolling of the cutter and workpiece), and radial feed which establishes the depth of cut for the pass. Using signals taken directly from the CNC controller of a Liebherr LSE500 gear shaping machine, the kinematics have been validated by comparing the measured and simulated position of the tool and workpiece.

Chapter 4 presents a model for predicting chip geometries and cutting forces in the gear shaping process. A discrete solid modeller that uses multi-dexel volume to represent the workpiece is used to calculate the cutter-workpiece engagement (CWE) at each time step during the process. The CWE is obtained in dexel format, and the chip cross-section is reconstructed using Delaunay triangulation and alpha shape method. By discretizing the tool cutting edge into nodes with varying cutting directions, inclination angle, and rake angle, incremental cutting forces are determined and integrated to obtain the force vector for the time step. Several case studies are presented which show good correlation between experimentally measured and simulated cutting forces in three directions. The most discrepancy occurred in the helical gear shaping cases where further study is needed to verify the sources of error.

A basic model for elastic deflection of the tool is presented in Chapter 5. The static stiffness at the bottom of the gear shaper cutter is characterized through modal hammer testing of the machine. Using the estimated stiffness, a feedback loop is established which calculates the deflection of the tool based on the cutting

forces at the previous time step. A virtual gear measurement system, which analyzes cross-sections of the gear, is used to calculate the profile deviations of the tooth profiles in the machined gears. Experimental measurements show good correlation between the simulated and measured profiles, however further research is needed to improve the simulated results.

Lastly, Chapter 6 gives an overview of the ShapePRO software which has been developed based on the presented research. ShapePRO is capable of predicting the cutting forces, tool deflections, and machined gear quality during gear shaping and is meant to be used as a tool for process planners in industry to optimize their programs.

## **Chapter 2**

### **Literature Review**

#### **2.1 Introduction**

In machining research, increasing the productivity (material removal rate), while maintaining or improving the quality of the machined workpiece is of utmost priority. In general, the limiting factors for achieving these goals are:

- Process stability (forced and chatter vibrations lead to poor surface quality and tool breakage/wear due to unstable cutting forces).
- Tool/machine rigidity (elastic deflections of the tool relative to the workpiece due to cutting forces lead to dimensional errors of the finished workpiece).
- Tool and workpiece overheating.

In classical machining operations (e.g. milling, turning, and drilling) these phenomena have been thoroughly researched and, in industry, the research is now methodically being applied to improve productivity and quality. In gear machining, however, this area of research is still in its infancy due to the complex nature of the processes used to machine gears. This chapter presents an overview of the existing machining research in the literature. Section 2.2 talks about some of the research in the field of classical machining operations, and Section 2.3 talks about the existing research in the field of gear machining.

#### **2.2 Classical Machining Literature**

In order to be able to predict the process stability and machined part quality, it is essential to be able to predict the chip geometry and cutting forces in any machining operation. In classical machining operations, the chip geometry can usually be calculated with analytical expressions as a function of the process parameters and tool geometry. Using a mechanistic approach, the cutting forces can be predicted by determining the varying chip thickness and width along the cutting edge and calculating incremental cutting forces with an orthogonal or oblique cutting model. For example, in the simple case of turning, the chip geometry is a function of the axial feedrate, radial depth of cut, and the geometry of the turning tool. For calculation of the cutting forces, the chip is analyzed in two sections: the tool nose radius zone and straight edge zone [3] [4] [5]. The chip thickness varies along the tool nose radius zone and so the cutting force is calculated by discretizing the chip into small segments and integrating the incremental cutting forces.

Although more complicated, similar methods are applied to the calculation of cutting forces in milling [6] [7] [8], multi-point thread turning [9], drilling [10] [11], and broaching [12] [13].

In recent literature, CAD software has been used to calculate the cutter-workpiece engagement in more complicated processes. In milling, for example, cutting forces can be calculated analytically if the axial depth of cut, feedrate, and tool immersion is known, however, for complicated workpieces machined with long CNC programs, CAD software is often needed to determine the depth of cut and tool immersion. To do this, the intersection of the tool and workpiece is calculated and the workpiece is continuously updated. This method is shown in [14] [15] [16] for 3-axis milling, extended to 5-axis milling in [17], and shown for broaching in [18]. In [14] - [18], exact solid modellers (using boundary representation) are used to model the workpieces. Although boundary representation is accurate, it can be slow and unstable (due to excessive computation) with complicated workpieces. Discrete modellers (such as dixel representation) are also used for modelling workpieces ( [19] for example) which offers better computational speed and robustness.

With knowledge of the cutting forces, elastic deflections of the tool can be considered to predict dimensional errors and surface quality of machined surfaces. Budak and Altintas [20] modelled a helical end mill as a cantilever beam with a flexible fixture. Analytical expressions are used for calculating the cutting forces, the elastic deflection of the tool, and the expected surface errors. Experiments showed good agreement in the predicted surface quality and dimensional error. Moreover, using this information, they developed a method of identifying the optimal feedrates and depth of cut which maximizes the material removal rate while maintaining a specified maximum error. This work was extended in [21] which used a finite element model (FEM) to calculate the flexibilities in thin walled workpieces. Workpiece flexibilities are also modelled in turning [22] to predict dimensional errors in the turned workpiece.

Moreover, dynamic deflections of the tool (forced and chatter vibrations) limit the productivity of machining processes as well as cause severe tool wear, tool breakage, and poor surface quality. By characterizing the dynamics at the contact point between the cutter and workpiece with modal transfer functions and considering the regenerative chip thickness mechanism (Figure 2.1), the self-excited vibrations in machining can be predicted [23] [24] [25]. Due to structural modes of the machine being excited by cutting forces, a wavy surface pattern is produced by the cutter. Subsequently, the chip thickness also becomes oscillatory which results in unstable and large oscillatory cutting forces until the tool breaks or jumps out of the cut. Using these theories, stability lobes can be determined in flat-end milling [26] [27], ball-end milling [28], plunge milling [29], 5-axis flank milling [30], turning/boring [31], and broaching

[32]. Stability lobes allow for process planners to choose spindle speeds and cutting depths that maximizes productivity while avoiding chatter vibrations, which ensures high quality of the workpiece, and maximizes tool life.

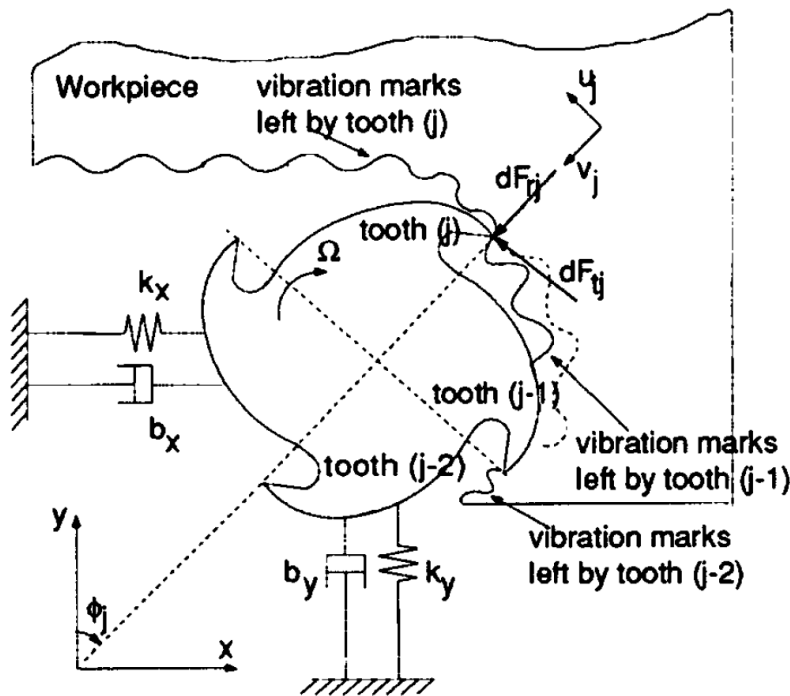


Figure 2.1: 2D dynamic analysis in milling (from [27]).

## 2.3 Gear Machining Literature

Since gear hobbing and gear shaping are the two most prominent methods for manufacturing cylindrical gears, this section will focus on the review of literature for those two processes. However, there is some cutting mechanics research in other processes as well, such as bevel gear cutting [33], generating gear grinding [34], and gear shaving [35].

### 2.3.1 Gear Hobbing

In gear hobbing, there has been extensive research in chip formation and cutting forces. However, there is little research in elastic tool deflection and vibrations during the process. Several studies have been performed in CAD based process simulation for gear hobbing. Klocke et al. [36] developed a software (called SPARTApro) capable of calculating the cutter-workpiece engagement and cutting forces in gear hobbing. Using a unique finite element approach, the workpiece is represented with an array of planes

perpendicular to the axis of the gear. Then, 2D chip geometry is determined on each plane by a penetration calculation between the cutter and workpiece. The chip cross-sections are discretized into volumetric elements and cutting forces are determined. Some experimental validation is presented in the form of spindle torque which showed adequate correlation between the simulated and measured profiles. They also studied the correlation between certain characteristics from the process simulation to the occurrence of surface defects in the finished gear (welded-on chips and smeared areas) [37]. Furthermore, the model was extended to be able to predict profile deviations as a result of certain process errors (tool clamp eccentricity and tool tooth profile errors) [38]. Tapoglou and Antoniadis [39] created a similar model (called HOB3D) which uses a commercial CAD software to calculate the cutter-workpiece engagement and is capable of calculating the cutting forces. The 3D chip geometry is sectioned onto planes which correspond to different revolved positions of the hob. The chip sections are partitioned into rectangles and incremental cutting forces are determined (Figure 2.2). Experimental validation is shown for the cutting forces in three directions which show good correlation. Sabkhi et al. also showed a similar model in [40].

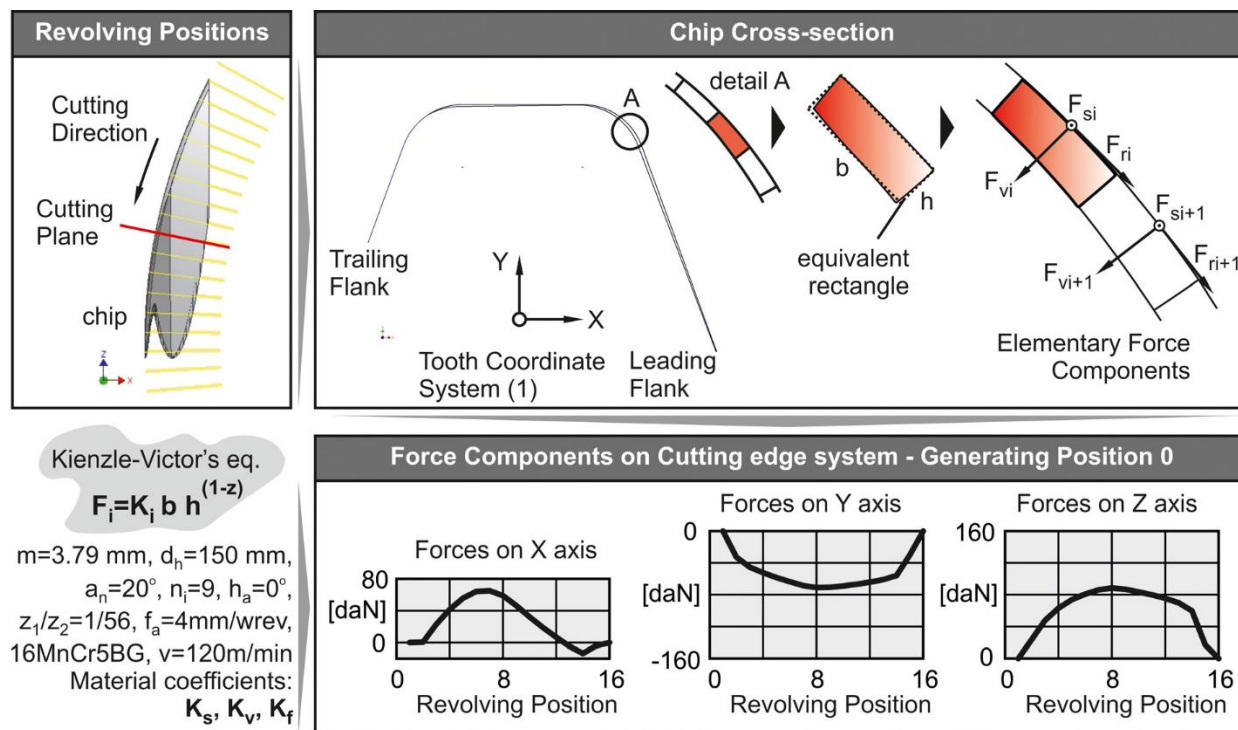


**Figure 2.2:** Cutting force prediction in HOB3D (from [39]).

FEM models of the hobbing process have also been established. Using loading conditions calculated from CAD based cutting simulation, Antoniadis et al. [41] created an FEM model of a hobbing tool which

calculated stresses and strain on the hob tooth. They focused on prediction of tool failure due to fatigue mechanisms and how to design the hobbing process to lower the chances of premature tool failure. Bouzakis et al. [42] created an FEM simulation of hobbing during the generation of a single tooth gap which focused on the prediction of chip flow obstruction and chip collision, while also being able to predict stresses, strain, and temperature. Furthermore, several other FEM based studies have been performed on tool wear mechanisms and the effect of process parameters on the distribution of tool wear on the gear hob [43] [44] [45].

### **2.3.2 Gear Shaping**

In gear shaping, there has been some study in chip formation during cutting. However, there is little published research in the cutting forces, elastic tool deflections, and vibrations. There exists several two-dimensional models which can predict the 2D generated cross-section of the workpiece. By tracing the trochoidal path of the shaper cutter on a plane (considering the tool geometry and process parameters), the generated tooth profile can be mathematically determined. This model is shown in [46] which focused on the effects of asymmetric teeth and tip fillets, in [47] which focused on the effect of protuberance and semi-topping, in [48] which focused on the effect of the gear ratio in internal gear generation, and in [49] which focused on the generation of non-circular gears. Bouzakis and König [50] studied the typical 2D chip cross-sections found in a gear shaping process and analyzed their effects on the chip flow and tool wear. They concluded that based on the width of the tip of the teeth on the gear shaper, there are different cross-sections of chip which will result in better tool life characteristics due to the way the chips flow off the rake face (Figure 2.3). Although this information is interesting, there is only limited insight presented on how to use the research to improve shaper cutter designs or improve process productivity.



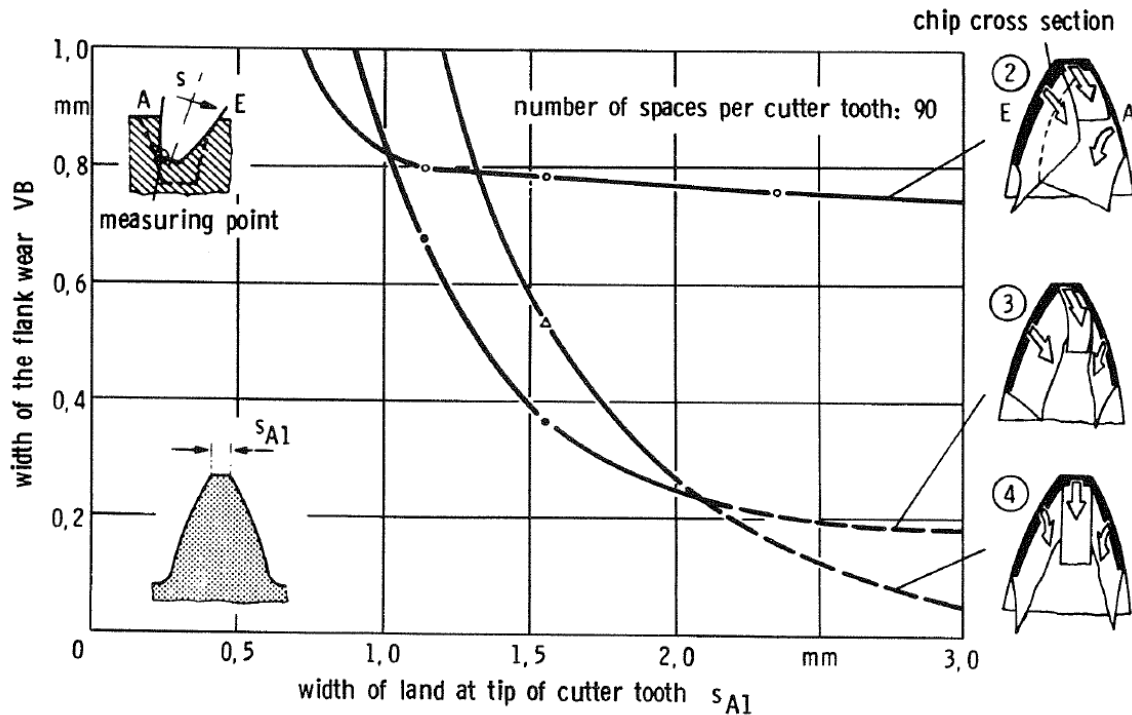


**Figure 2.3:** Influence of tool tip width and chip cross-section on tool wear (from [50]).

Datta et al. created an FEM model of the gear shaping operation [51]. They used ten-node tetrahedral elements to represent the gear cutter and assumed different loading conditions to predict the stress distribution on the gear shaper cutter. The work was extended in [52] which analyzed the stress and deflection of the tool under different cutting process parameters (cutting speed, feedrate, and depth of cut). The analysis, however, used empirical cutting forces, lacked experimental validation, and does not provide any insight on the effect of the tool deflections on workpiece quality.

## 2.4 Conclusions

From the studied literature, it is clear that there is a lack of a complete model for three dimensional chip geometry and cutting forces in gear shaping. Furthermore, there is a lack of study in elastic tool deflection and vibrations during the process which would allow for the accurate prediction of workpiece quality. The research presented in this thesis includes a complete three dimensional model of chip geometry, cutting forces, and a model for tool deflection. To the author's best knowledge, it is the first of its kind in regards to the gear shaping process. The research also serves as a basis for future research in vibration prediction for the gear shaping process.

# Chapter 3

## Kinematics of Gear Shaping

### 3.1 Introduction

In this chapter, the kinematics of the gear shaping process are described in detail. The motion involved in the process is complex as both the cutter and workpiece are moving simultaneously. The kinematics can be considered a superimposition of three different components: the reciprocating motion, rotary feed motion, and radial feed motion. Figure 3.1 shows these components for both internal and external gear generation.

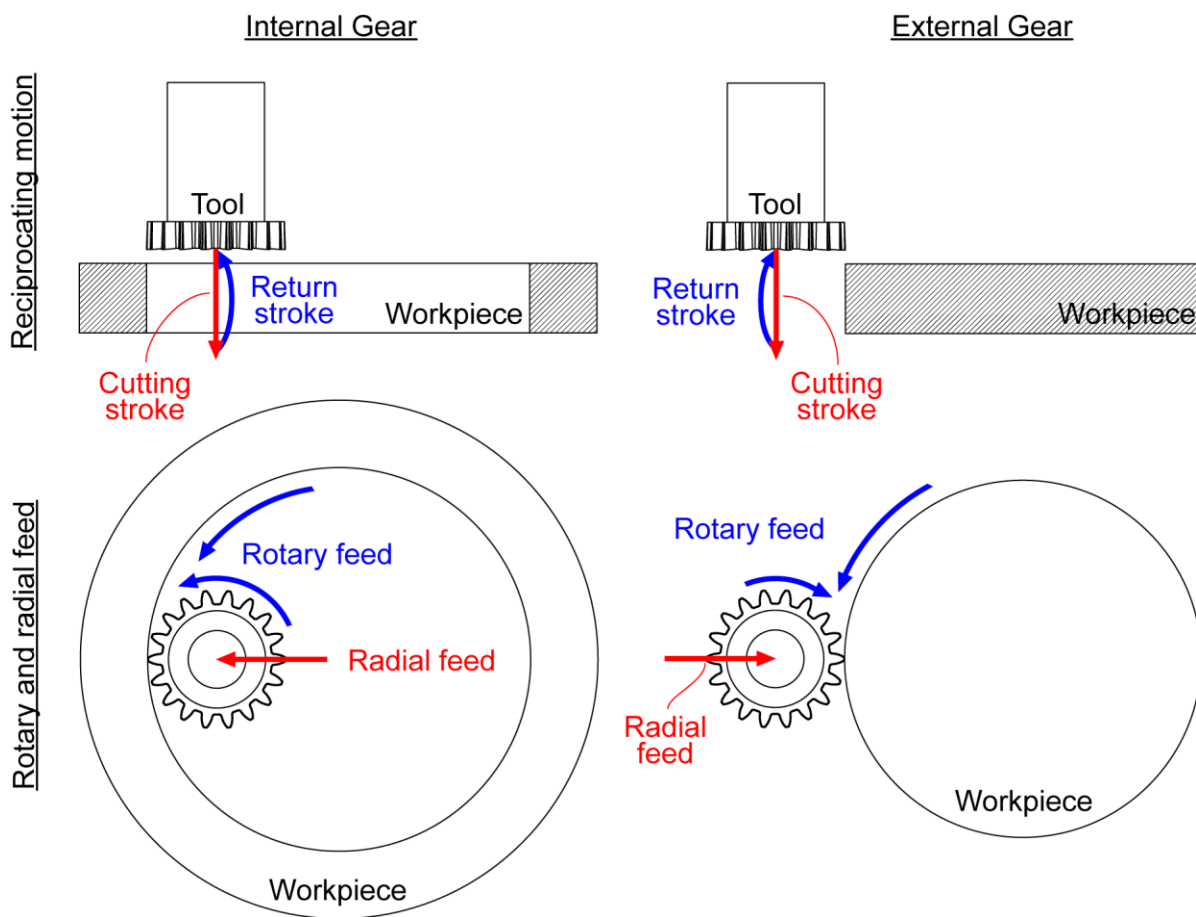


**Figure 3.1:** Kinematic components in gear shaping.

The reciprocating motion moves the cutter up and down which cuts the teeth in the workpiece. During the return stroke, there is back-off motion which prevents the tool cutting edge from rubbing against the workpiece while moving up. Although the back-off motion is important for ensuring good quality of the

finished gear, the motion does not affect the position of the tool during cutting and therefore is not included in the kinematic model. The cutter and workpiece both have rotary feeds which rotate proportionally to their gear ratio. There is radial motion of the tool at the beginning of each cutting pass which slowly feeds the cutter into the workpiece to avoid overloading the tool. In internal gear shaping, the tool radial feed moves away from the center of the workpiece and the rotary feeds are in the same direction. In external gear shaping, the tool radial feed moves towards the center of the workpiece and the rotary feeds are in the opposite direction. Furthermore, for helical gears, there is additional cutter rotation while reciprocating following the helical profile of the gear teeth.

In general, the magnitude of the rotary and radial feeds are proportional to the generated chip thickness while the frequency of the reciprocating motion is proportional to the cutting speed. In the remainder of this chapter, Section 3.2 talks about the basic gear nomenclature necessary for understanding the process, Section 3.3 describes the geometry of the cutter and workpiece, Section 3.4 mathematically describes the kinematics components of gear shaping, and Section 3.5 shows experimental validation of the kinematic model.

## 3.2 Gear Terminology

Before the kinematics of gear shaping is described in detail, basic gear terminology and nomenclature must first be established. There are four possible types of cylindrical gears which can be generated with gear shaping: spur internal, spur external, helical internal, and helical external. Spur gears have straight teeth (parallel to the axis of rotation), while helical gears have teeth which follow a helix profile around the axis of rotation. External gears have teeth on the outside circle of a cylinder, while internal gears have teeth on the inside circle of a ring.

As shown in Figure 3.2, two different planes can be defined for the gear teeth. The transverse plane which is perpendicular to the axis of rotation, and the normal plane which is perpendicular to the helix of the tooth. For spur gears, the normal plane and transverse plane are coincident. In gear design, the gear data parameters are typically given on the normal plane, however it is convenient to construct the gear profile on the transverse plane. The number of teeth on the gear is given by  $N$ , the helix angle of the gear is  $\beta$  ( $\beta = 0$  for spur gears), and the face width of the gear is given by  $b$ .

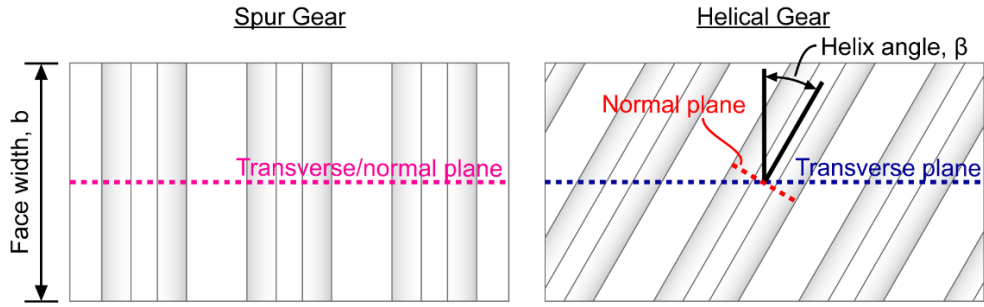


**Figure 3.2:** Transverse plane and normal plane in spur and helical gears.

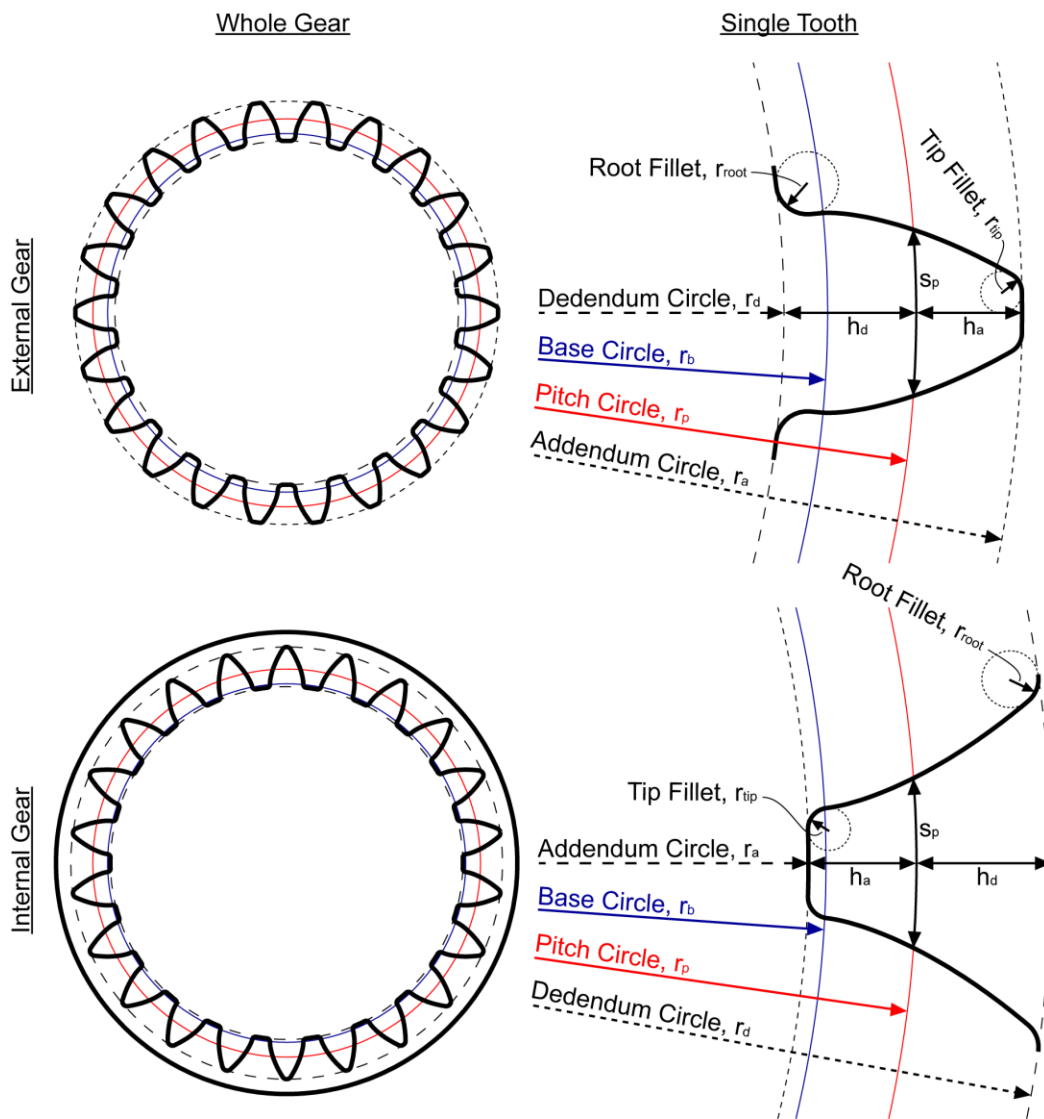


**Figure 3.3:** Basic gear geometry

Figure 3.3 illustrates basic gear geometry and nomenclature for both internal and external gears on the transverse plane. The size of the gear is proportional to its transverse module  $m_t$  which is given in units of length. The transverse module can be calculated from the normal module  $m_n$  as:

$$m_t = \frac{m_n}{\cos \beta} \quad [53] \quad (3.1)$$

The pitch circle radius  $r_p$  and base circle  $r_b$  radius are given by:

$$r_p = \frac{N m_t}{2} \quad [53] \quad (3.2)$$

$$r_b = r_p \cos \psi_t \quad [53] \quad (3.3)$$

Here,  $\psi_t$  is the transverse pressure angle which is defined as the angle tangent to the tooth profile at the pitch radius. The transverse pressure angle can be calculated from the normal pressure angle  $\psi_n$  as:

$$\psi_t = \tan^{-1} \left( \frac{\tan \psi_n}{\cos \beta} \right) \quad [53] \quad (3.4)$$

Each tooth begins at the root (dedendum circle) and ends at the tip (addendum circle) where each side (flank) of the tooth is the involute profile of the base circle. The radius of the addendum  $r_a$  and dedendum circles  $r_d$  are given by:

$$r_a = r_p + \epsilon h_a \quad (3.5)$$

$$r_d = r_p - \epsilon h_d \quad (3.6)$$

$$\epsilon = \begin{cases} +1 & \text{for external gear} \\ -1 & \text{for internal gear} \end{cases} \quad (3.7)$$

In a standard profile,  $h_a = m$  and  $h_d = 1.25 m$  [54], however these are often modified to non-standard values on gear shaper cutters.

The circular tooth thickness at an arbitrary radius  $r$  is given by  $s_r$ :

$$s_r = r \left[ \frac{s_p}{r_p} + 2\epsilon \left( \text{inv } \psi_t - \text{inv} \left( \text{acos} \frac{r_b}{r} \right) \right) \right] \quad (\text{for } r > r_b) \quad [53] \quad (3.8)$$

$$\text{inv } \theta = \tan \theta - \theta \quad [53] \quad (3.9)$$

$$s_p = \frac{\pi m_t}{2} + \epsilon 2x m_t \tan \psi_t \quad [53] \quad (3.10)$$

Here,  $s_p$  is the tooth thickness at the pitch radius and  $x$  is a profile modification factor which affects the thickness of the teeth. In a standard profile,  $x = 0$ , however manufactured gears often have slight profile shifts due to errors in the manufacturing process. In particular with gear shaping, gear shaper cutters are

often oversized or undersized due to the regrinding process which results in profile shifted gears [55]. Figure 3.4 shows how the profile modification factor affects the tooth thicknesses.

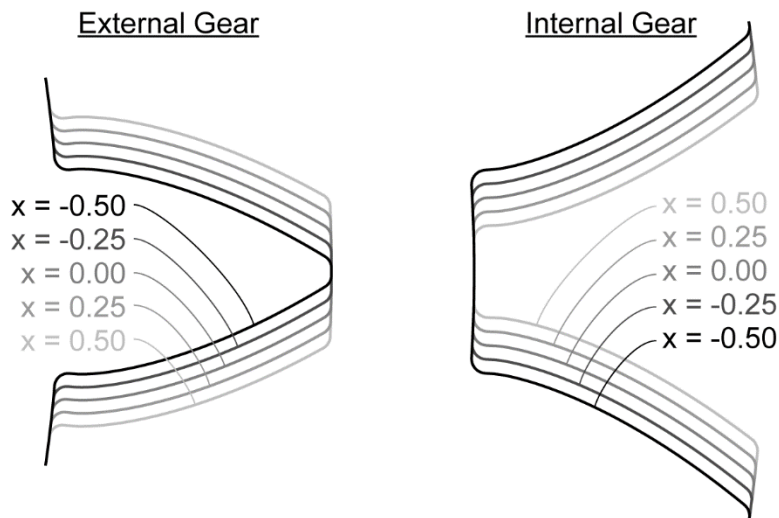


**Figure 3.4:** Gear tooth profile shift.

Finally, there are often fillets connecting the root to the flanks and the tip to the flanks. The tip fillet radius is given by  $r_{tip}$  and the root fillet radius is given by  $r_{root}$ .

### 3.3 Cutter and Workpiece Geometry

Gear shaper cutters take the form of modified cylindrical external gears. The shaper cutter must have the same module, pressure angle, and helix angle of the desired manufactured gear. The teeth are of involute profiles to generate involute profiles in the workpiece, there is increased addendum which creates additional clearance in the root of the produced gear, and there are several relief angles which are cut into the shaper cutter [55]. Figure 3.5 shows the design of a generic shaper cutter. The bottom face of the cutter has a rake angle (denoted by  $\alpha$ ) which forms a conical cutting face in the spur shaper case (shown in Figure 3.6 left) and allows for easier chip flow. The rake angle in a typical shaper cutter is between  $0^\circ$  and  $+10^\circ$ , however can be negative for finishing of hardened gears [2]. Additionally, there is side clearance and outside diameter clearance angles cut into the teeth which prevent rubbing of the cutter teeth onto the workpiece teeth. The side clearance angle is typically  $1.5^\circ - 2^\circ$ , and the outside diameter angle is typically  $2^\circ - 4^\circ$  [55]. In the helical gear shaper case, each tooth has its own rake face (shown in Figure 3.6 right) which has the effect of the rake angle and helix angle. The mathematical modelling of the rake face in each case is described in Section 4.4.1.

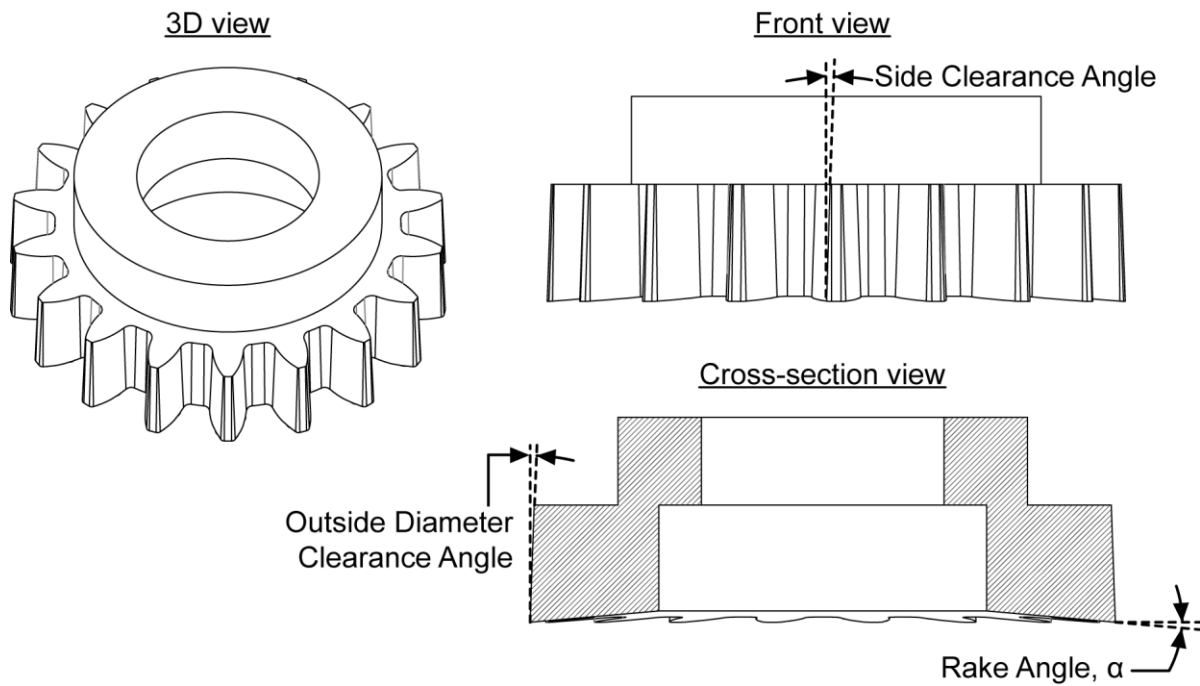


**Figure 3.5:** Gear shaper relief angles.

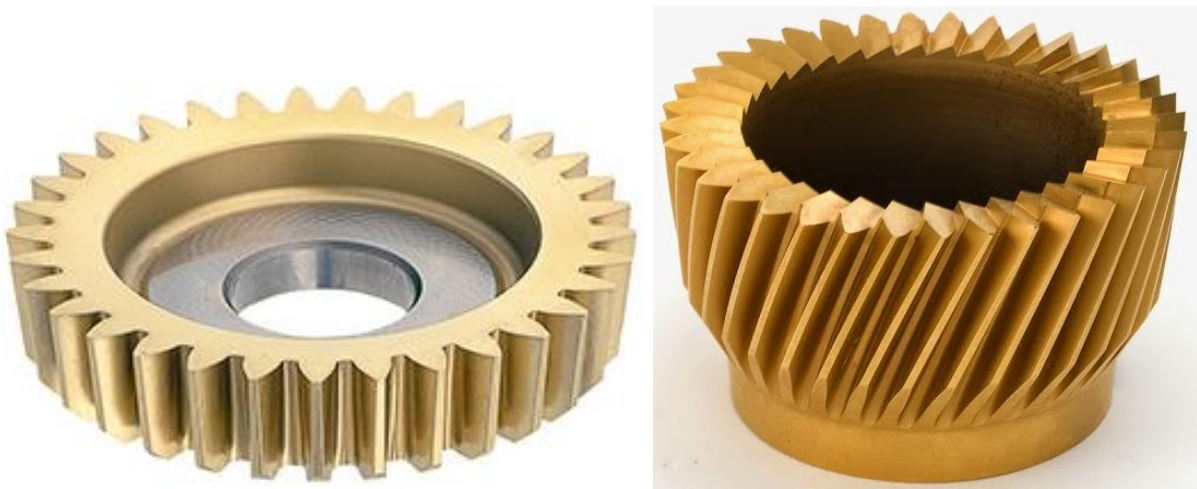


**Figure 3.6:** Comparison of spur gear shaper (from [56]) and helical gear shaper (from [57]).

Although workpiece blank geometry can be complicated for real gearbox parts, for the purpose of investigating the machining process, the geometry can be simplified to a cylinder for external gears and a ring for internal gears. For external gears, the outer diameter of the cylinder is equal to the addendum diameter of the desired gear. For internal gears, the inner diameter of the ring is equal to the addendum

diameter of the desired gear and the outer diameter is arbitrary as long as it is larger than the dedendum diameter.

### 3.4 Kinematics

#### 3.4.1 Coordinate Systems

Several different coordinate systems can be defined for convenience in different parts of the gear shaping analysis. Figure 3.7 illustrates three different coordinate systems:

- Machine coordinate system (MCS) or the world coordinate system is the stationary coordinate system in which the cutter and workpiece can be defined in absolute coordinates. This coordinate system is convenient for performing modal analysis of the machine.
- Workpiece coordinate system (WCS) is the coordinate system in which the observer is rotating with the gear. This coordinate system is convenient for measuring the cutting forces as it is easiest to attach a dynamometer to the workpiece fixture.
- Tool coordinate system (TCS) is the coordinate system in which the observer is rotating and translating with the cutter. This coordinate system is convenient for representing and defining the cutting edge.

The kinematics of gear shaping can be described with four variables: the axial rotation of the cutter  $\phi_c(t)$ , the axial rotation of the gear workpiece  $\phi_g(t)$ , the center-to-center distance between the cutter and workpiece  $r(t)$ , and the vertical position of the tool  $z(t)$ . For generalization of the process, the origin of the MCS can be assumed to be coincident with the origin of the WCS. Therefore, the homogenous transformations of the workpiece and tool relative to the MCS can be defined as:

$$T_{WCS}^{MCS}(t) = \begin{bmatrix} \cos \phi_g(t) & -\sin \phi_g(t) & 0 & 0 \\ \sin \phi_g(t) & \cos \phi_g(t) & 0 & 0 \\ 0 & 0 & 1 & 0 \\ 0 & 0 & 0 & 1 \end{bmatrix} \quad (3.11)$$

$$T_{TCS}^{MCS}(t) = \begin{bmatrix} \cos \phi_c(t) & -\sin \phi_c(t) & 0 & -r(t) \\ \sin \phi_c(t) & \cos \phi_c(t) & 0 & 0 \\ 0 & 0 & 1 & z(t) \\ 0 & 0 & 0 & 1 \end{bmatrix} \quad (3.12)$$

For the cutting simulation, it is convenient to keep the workpiece stationary and represent the tool in the WCS. The transformation between the tool and the workpiece can then be calculated as:



$$T_{TCS}^{WCS}(t) = [T_{WCS}^{MCS}]^{-1} T_{TCS}^{MCS} = \begin{bmatrix} \cos \phi_{cg}(t) & -\sin \phi_{cg}(t) & 0 & -r(t) \cos \phi_g(t) \\ \sin \phi_{cg}(t) & \cos \phi_{cg}(t) & 0 & r(t) \sin \phi_g(t) \\ 0 & 0 & 1 & z(t) \\ 0 & 0 & 0 & 1 \end{bmatrix} \quad (3.13)$$

Here,  $\phi_{cg}(t) = \phi_c(t) - \phi_g(t)$  is the relative angular position between the cutter and gear. Sections 3.4.2 - 3.4.4 below will describe how the four variables ( $z(t), r(t), \phi_c(t), \phi_g(t)$ ) are determined.

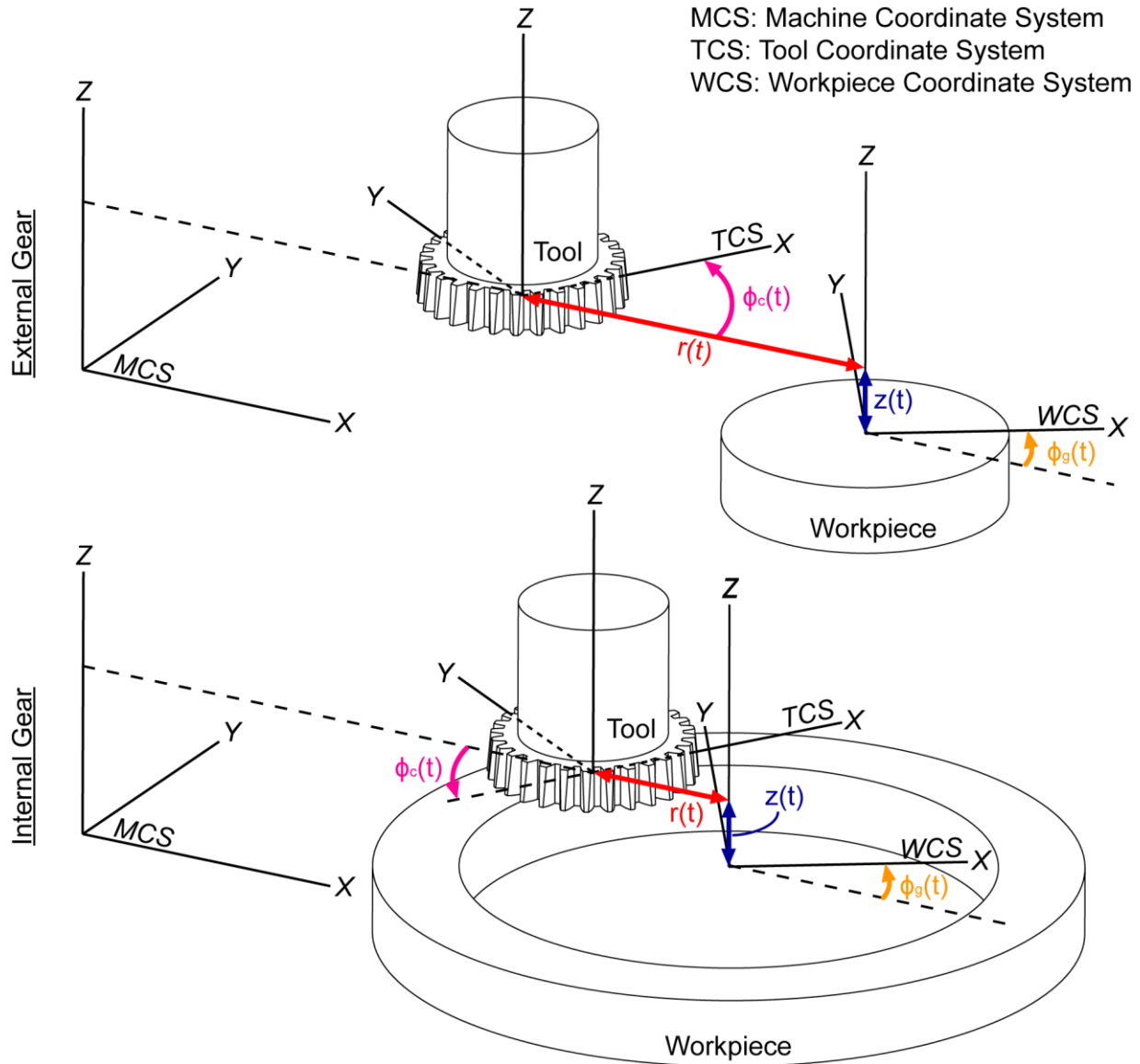


**Figure 3.7:** Coordinate systems in gear shaping.

### 3.4.2 Reciprocating Motion

In modern gear shaping machines, the reciprocating motion is accomplished using a slider crank mechanism as illustrated in Figure 3.8a. The length of the crank rod is CNC controlled which governs the length of the cutting stroke, hence the crank rod length is  $0.5 d_{\text{stroke}}$ . The connecting rod length  $d_{\text{con}}$  is a constant which is a parameter of the machine. The stroke length is a function of the workpiece face width and tool overruns ( $d_{\text{stroke}} = b + d_{\text{top}} + d_{\text{bottom}}$ ) as illustrated in Figure 3.8b. The  $z$  axis datum is defined at the top of the workpiece and is positive above the workpiece. The cutting stroke frequency  $f_{\text{cut}}$  is normally defined in units of DS/min in industry (double strokes per minute where a double stroke is one cutting stroke and one return stroke), therefore the cutting stroke frequency  $\omega_s$  expressed in engineering units is:

$$\omega_s \left[ \frac{\text{rad}}{\text{s}} \right] = f_{\text{cut}} \left[ \frac{\text{DS}}{\text{min}} \right] \cdot \frac{2\pi}{60} \quad (3.14)$$

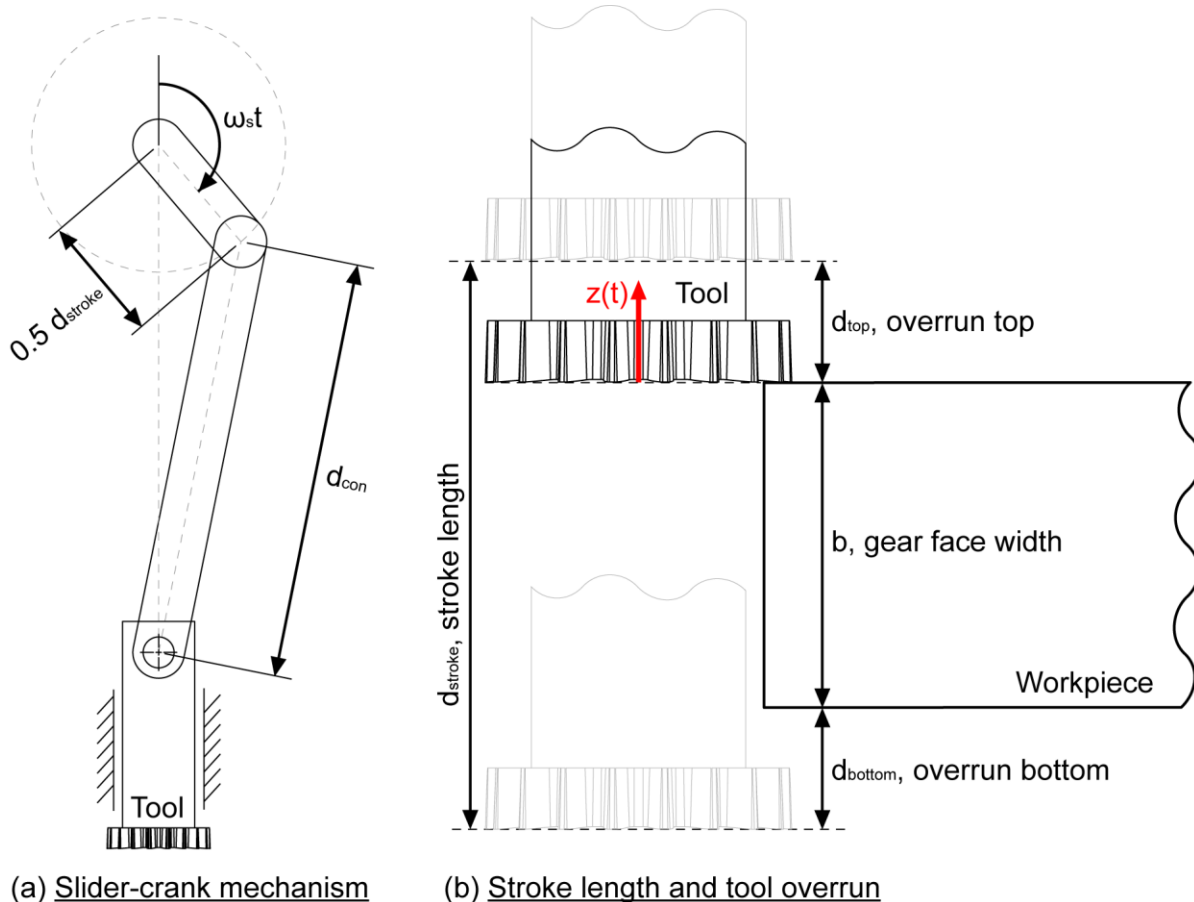


**Figure 3.8:** Reciprocating motion kinematics

Using trigonometric relationships, the reciprocating motion from the slider-crank mechanism can be expressed as:

$$z(t) = d_{top} - 0.5d_{stroke}(1 - \cos(\omega_s t)) + \sqrt{d_{con}^2 - (0.5d_{stroke} \sin(\omega_s t))^2} - d_{con} \quad (3.15)$$

However, this can be simplified to a pure sinusoidal equation without the effect of the slider-crank mechanism:

$$z(t) = d_{top} - 0.5d_{stroke}(1 - \cos(\omega_s t)) \quad (3.16)$$

Figure 3.9 shows a comparison of the two above equations for a single stroke with  $d_{top} = 1$ ,  $b = 10$ ,  $d_{bottom} = 1$ ,  $d_{con} = 500$ , and a stroke frequency of 400 DS/min. The maximum difference between the two profiles is about 0.03 mm, therefore the pure-sinusoidal equation is a very close approximation of the full slider-crank equation and in most cases can be used as a substitute.

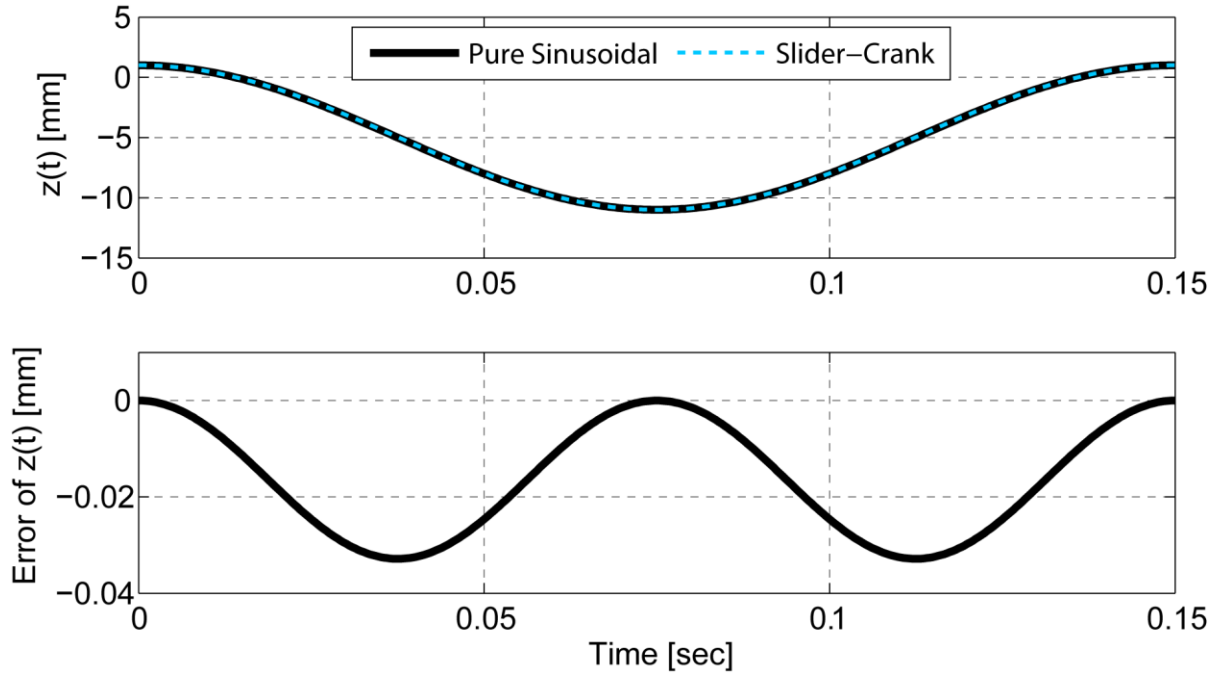


**Figure 3.9:** Slider-crank vs pure sinusoidal motion.

### 3.4.3 Rotary Feed Motion

The rotary feeds of the workpiece can be expressed as a function of a single process parameter  $f_{rotary}$  which is given in units of mm/DS (millimeters per double stroke). The rotational velocity of the workpiece ( $\omega_g$ ) can be solved as:

$$\omega_g \left[ \frac{\text{rad}}{\text{s}} \right] = f_{\text{rotary}} \left[ \frac{\text{mm}}{\text{DS}} \right] \cdot \frac{f_{\text{cut}} \left[ \frac{\text{DS}}{\text{min}} \right]}{60 r_{p_g}} \quad (3.17)$$

Here,  $r_{p_g}$  is the pitch radius of the gear (workpiece). Therefore, the rotational position of the workpiece ( $\phi_c$ ) is simply:

$$\phi_g(t) = \omega_g t \quad (3.18)$$

The rotational position of the tool ( $\phi_c$ ) is a function of the workpiece rotation and the vertical position of the tool. The tool must rotate as the workpiece rotates to emulate the rolling of the gears. For helical gears, the tool must also rotate while reciprocating following the profile of the helical teeth. The rotation of the cutter can be expressed as:

$$\phi_c(t) = \underbrace{-\frac{\epsilon \omega_g}{R} t}_{\text{rolling of gears}} + \underbrace{\frac{z(t) \tan \beta}{r_{p_c}}}_{\text{helical component}} \quad (3.19)$$

$$R = N_c / N_g \quad (3.20)$$

Here,  $R$  is the gear ratio between the cutter and workpiece, and  $r_{p_c}$  is the pitch radius of the cutter.

### 3.4.4 Radial Feed Motion

A gear shaping process consists of one or more cutting passes (usually 1 or 2 roughing passes and 1 finishing pass). Each pass removes some radial depth of cut which can be defined using the center-to-center radial distances  $r_{\text{start}}$  and  $r_{\text{end}}$ . For internal gears,  $r_{\text{start}} < r_{\text{end}}$ , and for external gears,  $r_{\text{start}} > r_{\text{end}}$ . Table 3.1 shows how these radial distances are determined for the  $i$ th cutting pass in  $n$  number of passes.

**Table 3.1:** Cutting pass radial distances

	<u>Cutting Pass</u>		
	<b>First</b> $i = 1$	<b>Intermediate</b> $1 < i < n$	<b>Last</b> $i = n, n > 1$
$r_{\text{start}_i}$	$r_{\text{scrape}}$	$r_{\text{end}_{i-1}}$	$r_{\text{end}_{i-1}}$
$r_{\text{end}_i}$	$\begin{cases} r_{\text{start}_i} - \epsilon d_{\text{cut}_i} & \text{for } n > 1 \\ r_{gc} & \text{for } n = 1 \end{cases}$	$r_{\text{start}_i} - \epsilon d_{\text{cut}_i}$	$r_{gc}$

Here,  $d_{\text{cut}}$  is the depth of cut specified for the pass,  $r_{\text{scrape}} = r_{a_g} + \epsilon r_{a_c}$  is the scraping distance (the radial distance at which the addendum of the cutter just touches the addendum of the workpiece), and  $r_{gc} = r_{p_g} +$

$\epsilon r_{pc}$  is the final nominal center-to-center distance (in practice,  $r_{gc}$  is often manually overridden to correct for tooth thickness errors in the finished gear).

There are a couple different radial infeed strategies which exist. The most common method is Radial with Rotary (RwR) in which the cutter is radially fed into the workpiece whilst simultaneously rotating. Typically, the infeed motion is defined by radial feed at start of infeed ( $f_{\text{radial, start}}$ ) and radial feed at end of infeed ( $f_{\text{radial, end}}$ ) given in units of mm/DS. These can be translated into respective radial velocities with the formulas:

$$v_{r, \text{start}} \left[ \frac{\text{mm}}{\text{s}} \right] = -\epsilon f_{\text{radial, start}} \left[ \frac{\text{mm}}{\text{DS}} \right] \cdot \frac{f_{\text{cut}} \left[ \frac{\text{DS}}{\text{min}} \right]}{60} \quad (3.21)$$

$$v_{r, \text{end}} \left[ \frac{\text{mm}}{\text{s}} \right] = -\epsilon f_{\text{radial, end}} \left[ \frac{\text{mm}}{\text{DS}} \right] \cdot \frac{f_{\text{cut}} \left[ \frac{\text{DS}}{\text{min}} \right]}{60} \quad (3.22)$$

Usually,  $|v_{r, \text{end}}| < |v_{r, \text{start}}|$  to prevent overloading of the tool since the chip area will increase as the cutter approaches the final center-to-center distance. After the infeed is complete, the workpiece is rotated an additional  $360^\circ$  to complete the cutting pass. Although the infeed can be defined using the four parameters ( $r_{\text{start}}$ ,  $r_{\text{end}}$ ,  $f_{\text{radial, start}}$ , and  $f_{\text{radial, end}}$ ), different gear shaping machines will use different velocity and acceleration profiles during the infeed. For example, sophisticated machines may use jerk limited trajectory planning where the rate of change in acceleration is limited [58]. In the simplest case, a constant step acceleration could be used where the radial kinematics can be described with the below equations. The position, velocity, and acceleration profiles are illustrated in Figure 3.10.

$$t_{\text{infeed}} = 2 \left| \frac{r_{\text{end}} - r_{\text{start}}}{v_{r, \text{end}} + v_{r, \text{start}}} \right| \quad (3.23)$$

$$t_{\text{pass}} = t_{\text{infeed}} + \frac{2\pi}{\omega_g} \quad (3.24)$$

$$a_{\text{infeed}} = \frac{v_{r, \text{end}} - v_{r, \text{start}}}{t_{\text{infeed}}} \quad (3.25)$$

$$r(t) = \begin{cases} r_{\text{start}} + v_{r, \text{start}}t + \frac{1}{2}a_{\text{infeed}}t^2 & \text{for } 0 \leq t < t_{\text{infeed}} \\ r_{\text{end}} & \text{for } t_{\text{infeed}} \leq t \leq t_{\text{pass}} \end{cases} \quad (3.26)$$

$$\frac{d(r(t))}{dt} = \begin{cases} v_{r, \text{start}} + a_{\text{infeed}}t & \text{for } 0 \leq t < t_{\text{infeed}} \\ 0 & \text{for } t_{\text{infeed}} \leq t \leq t_{\text{pass}} \end{cases} \quad (3.27)$$

$$\frac{d^2(r(t))}{dt^2} = \begin{cases} a_{\text{infeed}} & \text{for } 0 \leq t < t_{\text{infeed}} \\ 0 & \text{for } t_{\text{infeed}} < t \leq t_{\text{pass}} \end{cases} \quad (3.28)$$

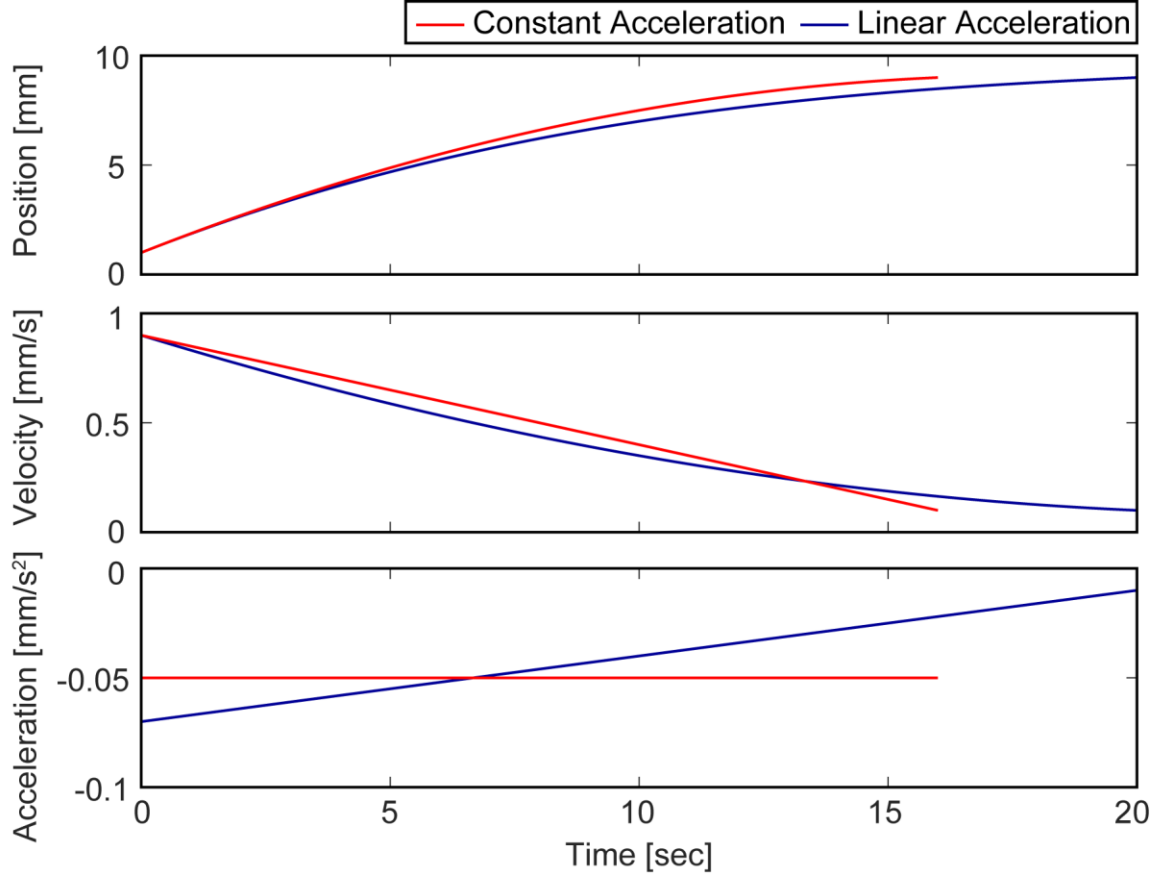


**Figure 3.10:** Comparison of constant acceleration and linear acceleration infeed profiles.

Here,  $t_{\text{infeed}}$  is the time required for the infeed,  $t_{\text{pass}}$  is the total time required for the cutting pass,  $a_{\text{infeed}}$  is the radial acceleration during the infeed, and  $t$  is the amount of time passed since the beginning of the cutting pass.

In a more complicated case, linear acceleration may also be used during infeed where the acceleration of the drive begins at  $a_{\text{infeed, start}}$  and ends at  $a_{\text{infeed, end}}$ . In this case, the kinematics of the radial feed is described by the below equations:

$$r(t) = \begin{cases} r_{\text{start}} + v_{r, \text{start}} t + \frac{1}{2} a_{\text{infeed, start}} t^2 + \frac{a_{\text{infeed, end}} - a_{\text{infeed, start}}}{6 t_{\text{infeed}}} t^3 & \text{for } 0 \leq t < t_{\text{infeed}} \\ r_{\text{end}} & \text{for } t_{\text{infeed}} \leq t \leq t_{\text{pass}} \end{cases} \quad (3.29)$$

$$\frac{d(r(t))}{dt} = \begin{cases} v_{r,start} + a_{infeed,start}t + \frac{a_{infeed,end} - a_{infeed,start}}{2 t_{infeed}} t^2 & \text{for } 0 \leq t < t_{infeed} \\ 0 & \text{for } t_{infeed} \leq t \leq t_{pass} \end{cases} \quad (3.30)$$

$$\frac{d^2(r(t))}{dt^2} = \begin{cases} a_{infeed,start} + \frac{a_{infeed,end} - a_{infeed,start}}{t_{infeed}} t & \text{for } 0 \leq t < t_{infeed} \\ 0 & \text{for } t_{infeed} < t \leq t_{pass} \end{cases} \quad (3.31)$$

Here, the value of the accelerations would be determined by the machine's proprietary algorithms. For example, if the machine has a pre-determined  $a_{infeed,end}$ , then the  $t_{infeed}$  can be calculated by solving a quadratic equation, and then the  $a_{infeed,start}$  can be determined:

$$t_{infeed} = \frac{(2v_{r,end} + v_{r,start}) \pm \sqrt{(2v_{r,end} + v_{r,start})^2 - 6 a_{infeed,end} (r_{end} - r_{start})}}{a_{infeed,end}} \quad (3.32)$$

$$a_{infeed,start} = \frac{2(v_{r,end} - v_{r,start})}{t_{infeed}} - a_{infeed,end} \quad (3.33)$$

Above, logic may be used to determine the signage of the plus-minus in the quadratic formula. If only one of the answers is positive, than the positive answer is correct. If both answers are positive, than the smaller answer can be chosen. The linear acceleration profile is compared against the constant acceleration profile in Figure 3.10 for the same  $r_{start}$ ,  $r_{end}$ ,  $f_{radial,start}$ ,  $f_{radial,end}$ , and a pre-set  $a_{infeed,end}$  of  $-0.01$ . Depending on the value of  $a_{infeed,end}$ , the linear acceleration profile may be shorter or longer than the constant acceleration profile.

### 3.5 Experimental Validation

In order to validate the kinematic model, servo position commands are captured from the Siemens 840D CNC servo controller in a Liebherr LSE500 gear shaping machine tool (pictured in Figure 3.11). The Liebherr LSE500 machine is a CNC based machine that is capable of producing cylindrical gears of all types up to a diameter of 500 mm. Earlier versions of gear shaping machines were completely mechanical and thus had limitations. For example, gearing was used to link the motion between the cutter and workpiece rotation drives, thus only certain gear ratios could be used. Moreover, mechanical guides were used to generate the helical component of the tool rotation, thus only certain helix angles could be generated. In the Liebherr machine, each drive is numerically controlled so there are no such limitations and the setup time is significantly reduced.



**Figure 3.11:** Liebherr LSE500 Machine (from [59]).

The axis layout for the Liebherr machine is shown in Figure 3.12. The axis which controls the center-to-center distance of the cutter and workpiece  $r(t)$  is labelled X1, the tool rotation  $\phi_c(t)$  is C1, the workpiece rotation  $\phi_g(t)$  is C2, the crank rotation drive for the reciprocating motion is Z3, and there is additionally a ZL3 axis (not pictured) which uses linear encoders to measure the vertical position of the tool  $z(t)$ . There are several other axes (for example the process automation axes) which are not important for the experimental validation of the kinematic model.

Commanded position data from the four important axes (X1, C1, C2, and ZL3) are captured from the machine during a shaping cutting pass. Table 3.1 shows the gear data and process data for the cutting pass. The machine has its own proprietary optimization algorithms which can slightly alter the nominal process parameters to achieve better quality gears. For example, there is temperature compensation which automatically adjusts the center-to-center distance to take into account thermal deformations of the machine. It is difficult to reverse engineer the machine's proprietary compensation algorithms, so the parameters are manually adjusted to improve the alignment of the measured and simulated profiles (shown in the bold values in Table 3.2).



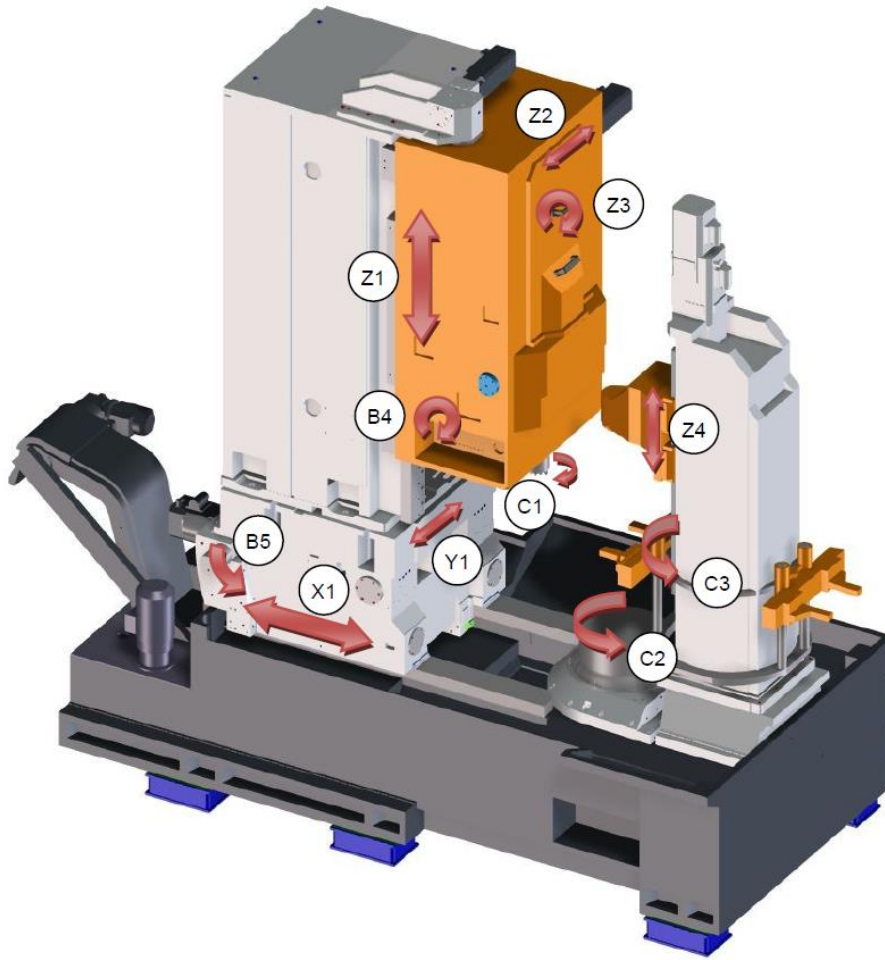


**Figure 3.12:** Liebherr LSE500 Axes Labels (from [60]).

**Table 3.2:** Cutting pass parameters and gear data for kinematic experimental validation.

Gear Data		Cutting Pass Parameters	
$\epsilon$	1 (external gear)	$f_{cut}$ [DS/min]	300 ( <b>300.11</b> )
$m_n$ [mm]	2.1167	$f_{rotary}$ [mm/DS]	0.8 ( <b>0.75</b> )
$\psi_n$ [deg]	20	$f_{radial, start}$ [mm/DS]	0.1
$\beta$ [deg]	-20 (helix angle)	$f_{radial, end}$ [mm/DS]	0.025
$N_c$	36	$r_{start}$ [mm]	103.03
$N_g$	52	$r_{end}$ [mm]	98.243
$b$	50	$d_{top}$ [mm]	5
		$d_{bottom}$ [mm]	5

Linear acceleration profiles are used in the simulation where the  $a_{\text{infeed, end}} = 0.0075$  is determined manually from the captured position profile. Figure 3.13 shows the position of the X1 axis during the infeed from the captured servo data and simulated profiles, along with their velocity and acceleration determined by numerical differentiation. It can be seen that the profiles based on linear acceleration closely emulate the movement of the gear shaping machine. Comparisons for position of all four of the axes can be seen in Figure 3.14 during the whole process and during a zoomed in portion at the beginning of the cutting pass. The only post processing applied to the captured profiles is shifting to account for the initial position of the axes. As seen, all four axes in the simulated profiles match closely to the captured commanded position data.

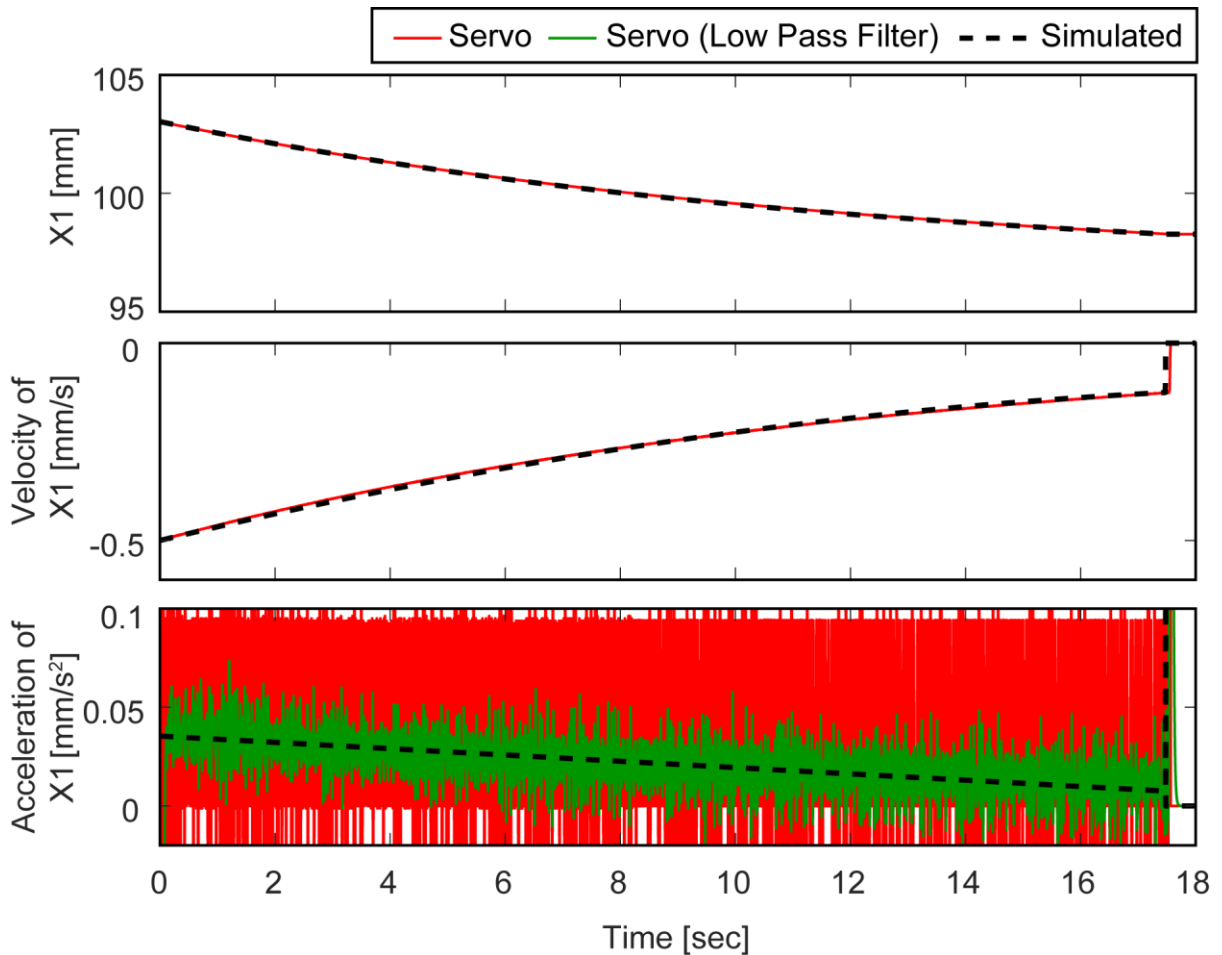


**Figure 3.13:** Position, velocity, and acceleration profiles of X1 axis during infeed.

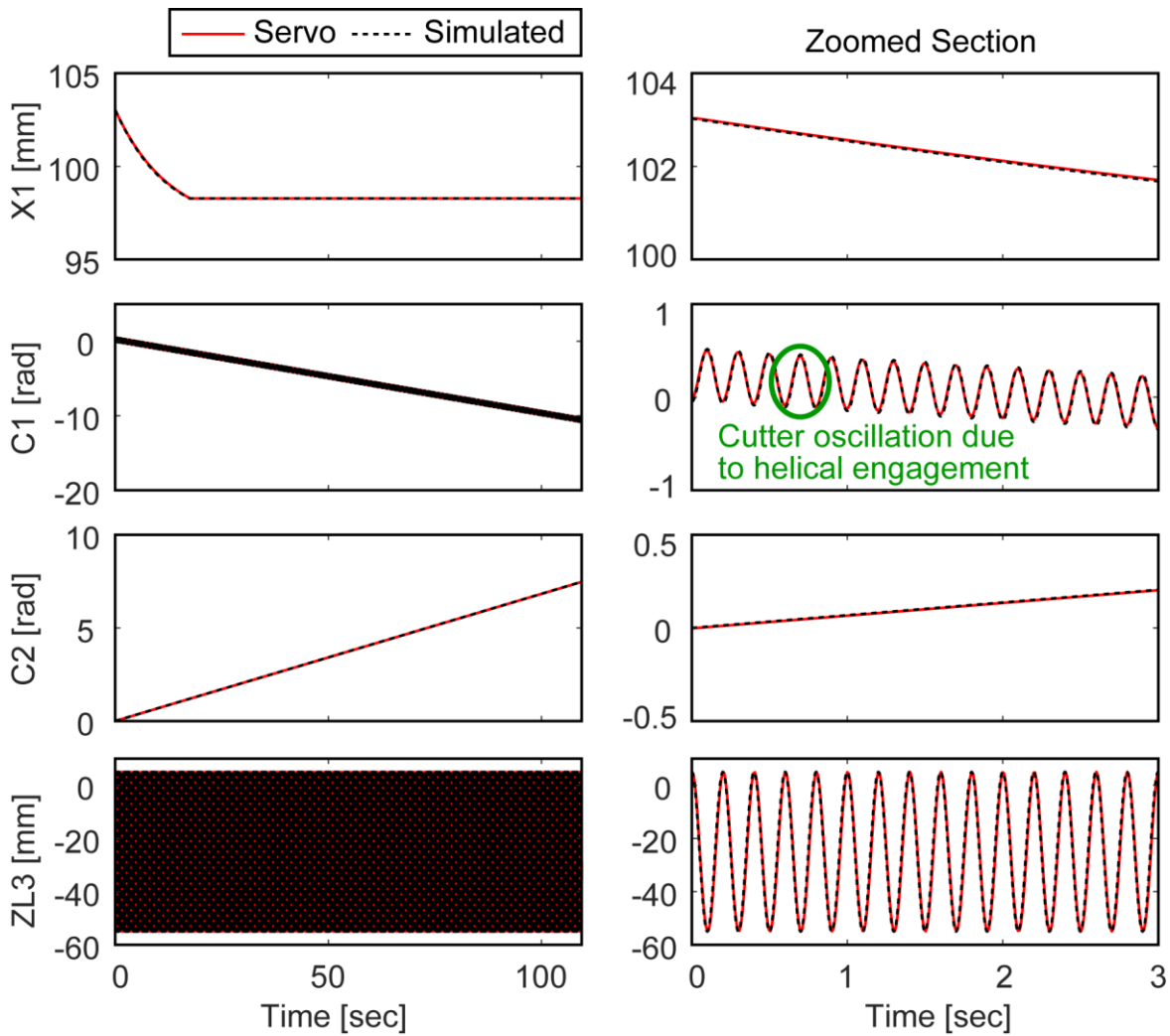


**Figure 3.14:** Comparison of simulated and captured X1, C1, C2, and ZL3 profiles.

### 3.6 Conclusions

The kinematics of the gear shaping process include three different components (reciprocating motion, rotary feed motion, and radial feed motion). The reciprocating motion moves the cutter up and down which generates the majority of the cutting action. The rotary feed motion of the cutter and workpiece emulate the rolling of two gears, and in addition the tool rotates while reciprocating following the helical profile of the workpiece. The radial motion slowly feeds the cutter into the workpiece, usually in one to three cutting passes, until the final depth of cut is reached. The kinematic model has been experimentally verified using measured data from the CNC controller of a Liebherr gear shaping machine.

## Chapter 4

### Cutting Force Prediction

#### 4.1 Introduction

In this chapter, the cutting force prediction model is described in detail including experimental validation. To predict the cutting forces, the cutter-workpiece engagement is first calculated using a discrete solid modeller, called ModuleWorks, which uses the multi-dexel representation. The tool cutting edge is discretized into nodes where each node represents a generalized oblique cutting force model with varying principle cutting directions, local inclination angle, and local normal rake angle. At each time step, two dimensional chip geometry is calculated and the force contribution from each node is summated to achieve the total force vector.

#### 4.2 Cutting Force Models

##### 4.2.1 Orthogonal

The orthogonal cutting model [61] is the most basic cutting force model. As illustrated in Figure 4.1, the cutting edge is perpendicular to the cutting velocity  $V_c$ . There are two force components which are generated in this model: the tangential force  $F_t$ , and feed force  $F_f$ . The tangential force is parallel and opposite in direction to the cutting velocity  $V_c$ . The feed force is perpendicular to the cutting edge and cutting velocity and is directed outward from the workpiece surface. Each of the cutting forces are linear with respect to the undeformed chip width  $b$ , undeformed chip thickness  $h$ , and the cutting coefficients ( $K_{tc}, K_{te}, K_{fc}, K_{fe}$ ):

$$F_t = K_{tc}bh + K_{te}b = K_{tc}a + K_{te}b \quad (4.1)$$

$$F_f = K_{fc}bh + K_{fe}b = K_{fc}a + K_{fe}b \quad (4.2)$$

The cutting components  $K_{tc}bh$  and  $K_{fc}bh$  are due to the shearing of the material and are thus proportional to the undeformed chip area ( $a = bh$ ), while the edge components  $K_{te}h$  and  $K_{fe}h$  are due to the rubbing of the edge against the workpiece and are thus proportional to the undeformed chip width  $b$ . Additional parameters in the model include the tool rake angle  $\alpha_r$  which is defined as the angle between the rake face and the feed direction, and the shear angle  $\phi_c$  which is defined as the angle between the shearing plane of the material and the cutting velocity. The cutting coefficients are affected by many factors (for example,

workpiece material, tool coating, tool wear, lubrication, rake angle, cutting speed, chip thickness) and are typically determined with experimental orthogonal cutting tests.

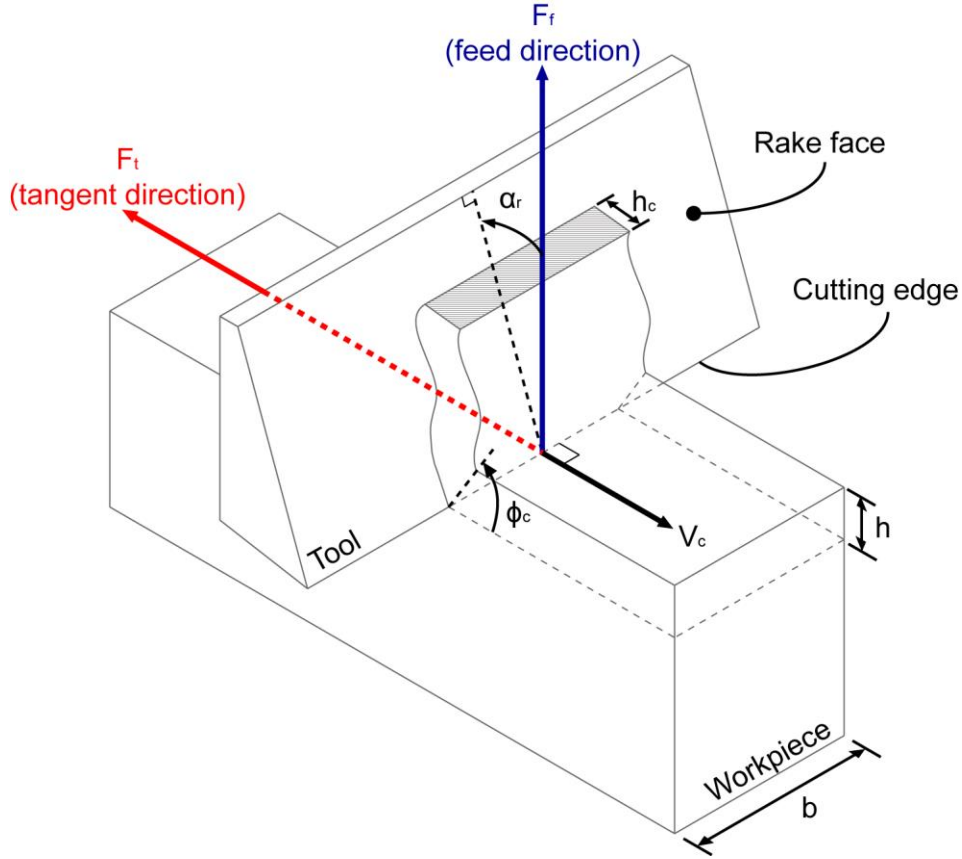


**Figure 4.1:** Orthogonal cutting model.

#### 4.2.2 Oblique

The oblique cutting force model [61] is an extension of the orthogonal cutting model where the cutting edge is not perpendicular to the cutting velocity as shown in Figure 4.2. In addition to the tangential and feed force as seen in the orthogonal model, there is a radial force  $F_r$  which is perpendicular to the tangential and feed force. Similar to the orthogonal model, the radial force is proportional to the undeformed chip area, chip thickness, and cutting coefficients ( $K_{rc}$ ,  $K_{re}$ ):

$$F_r = K_{rc}bh + K_{re}b = K_{rc}a + K_{re}b \quad (4.3)$$

The angle between the cutting edge and the radial direction is defined as the inclination angle  $i$ . Similar to the orthogonal model, the tool normal rake angle  $\alpha_n$  is defined as the angle between the feed direction and

the rake face measured on the plane orthogonal to the cutting edge (called the normal plane). In addition, there is a chip flow angle  $\eta$  which is defined as the angle at which the chip flows on the rake face measured from the vector on the rake face normal to the cutting edge. The chip flow angle is normally assumed to be equal to the inclination angle ( $\eta = i$ ) [62].

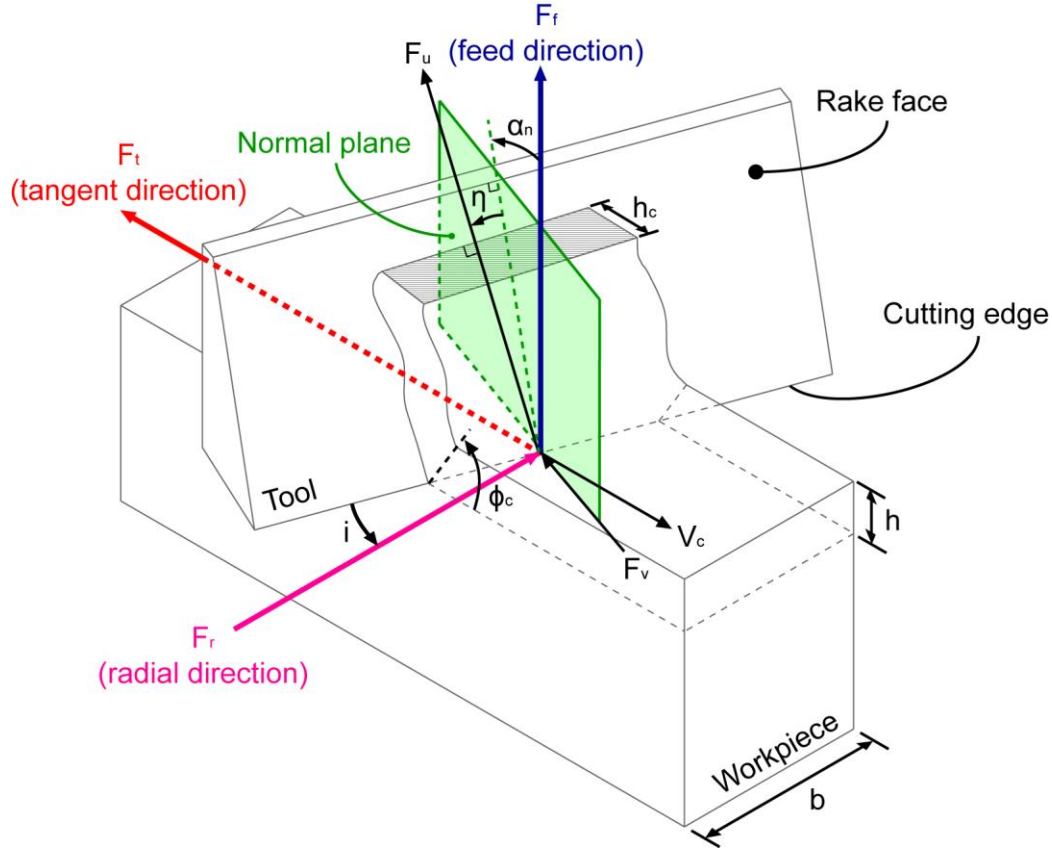


**Figure 4.2:** Oblique cutting model.

### 4.2.3 Orthogonal to Oblique

A more comprehensive cutting model is the orthogonal to oblique model [61]. This model allows cutting coefficients to be estimated by orthogonal cutting experiments, however is still applicable to tools with oblique angles. The shear angle ( $\phi_c$ ), average friction angle ( $\beta_d$ ), and shearing stress ( $\tau_s$ ) are determined from orthogonal cutting experiments. The shear angle can be calculated with the below equation where  $r_c$  is the chip ratio and  $h_c$  is the deformed chip thickness.

$$\phi_c = \tan^{-1} \frac{r_c \cos \alpha_r}{1 - r_c \sin \alpha_r}, \quad r_c = \frac{h}{h_c} \quad (4.4)$$

The friction angle, which is a representation of the coefficient of friction on the rake face, can be calculated as:

$$\beta_a = \alpha_n + \tan^{-1} \frac{K_{fc}}{K_{tc}} \quad (4.5)$$

Finally, the shearing stress can be calculated with the below formula where  $F_s$  is the shearing force and  $A_s$  is the chip cross-section area on the shearing plane:

$$\tau_s = \frac{F_s}{A_s} = \frac{F_{tc} \cos \phi_c - F_{fc} \sin \phi_c}{bh / \sin \phi_c} = \sin \phi_c (K_{tc} \cos \phi_c - K_{fc} \sin \phi_c) \quad (4.6)$$

To obtain the oblique cutting coefficients, the orthogonal to oblique transformation is applied. The shearing cutting coefficients ( $K_{tc}, K_{fc}, K_{rc}$ ) are determined with the below equations. The tangential and feed edge coefficients ( $K_{te}, K_{fe}$ ) are assumed to be equal to the edge coefficients identified in the orthogonal cutting tests, and the radial edge coefficient  $K_{re}$  is typically approximated as zero.

$$K_{tc} = \frac{\tau_s}{\sin \phi_n} \frac{\cos(\beta_n - \alpha_n) + \tan i \tan \eta \sin \beta_n}{\sqrt{\cos^2(\phi_n + \beta_n - \alpha_n) + \tan^2 \eta \sin^2 \beta_n}} \quad (4.7)$$

$$K_{fc} = \frac{\tau_s}{\sin \phi_n \cos i} \frac{\sin(\beta_n - \alpha_n)}{\sqrt{\cos^2(\phi_n + \beta_n - \alpha_n) + \tan^2 \eta \sin^2 \beta_n}} \quad (4.8)$$

$$K_{rc} = \frac{\tau_s}{\sin \phi_n} \frac{\cos(\beta_n - \alpha_n) \tan i + \tan \eta \sin \beta_n}{\sqrt{\cos^2(\phi_n + \beta_n - \alpha_n) + \tan^2 \eta \sin^2 \beta_n}} \quad (4.9)$$

Here, the normal shear angle  $\phi_n$  is assumed to be equal to the identified orthogonal shear angle  $\phi_c$ , and the normal friction angle  $\beta_n$  is assumed to be equal to the identified orthogonal friction angle  $\beta_a$ . It is noteworthy that the shear angle, friction angle, and shear stress are dependent on the rake angle of the tool. In the orthogonal to oblique transformation, the normal rake angle  $\alpha_n$  (i.e. projection of the oblique tool's rake angle onto the normal plane) is also assumed to coincide with the rake angle in the pure orthogonal cutting conditions.

#### 4.2.4 Exponential Chip Thickness

The above models have assumed linear relationships with respect to the undeformed chip area. However, it has been shown that the cutting forces can exhibit nonlinear behaviours with respect to the chip thickness [61]. Therefore, the cutting forces are often expressed as nonlinear functions of the undeformed chip thickness:

$$F_t = (K_t h^{-p})a, \quad F_f = (K_f h^{-q})a, \quad F_r = (K_r h^{-r})a \quad (4.10)$$

Here, the exponents  $(p, q, r)$  are additional coefficients determined from experiments. Furthermore, cutting forces can also be nonlinear with respect to the cutting speed, therefore the above equations can also be extended to include the effect of the cutting speed.

#### 4.2.5 Kienzle

The nonlinear Kienzle cutting force model [63] is another widely used model in the literature. In this model, there is a friction force  $F_u$  and a normal force  $F_v$ , as seen in Figure 4.2. The normal force is normal to the rake face while the friction force is coincident with the rake face and is parallel to the vector which defines the chip flow angle  $\eta$ . Similar to the exponential chip model, each force component is nonlinear with respect to the chip thickness  $h$ :

$$F_u = (K_u h^{-u})a, \quad F_v = (K_v h^{-v})a \quad (4.11)$$

Here,  $K_u$ ,  $K_v$ ,  $u$ , and  $v$  are cutting coefficients which are determined experimentally. The coefficients in the Kienzle model can be transformed into the oblique cutting coefficients with the following transformation [64]:

$$K_{tc} = K_u h^{-u} (\sin i \sin \eta + \cos i \sin \alpha_n \cos \eta) + K_v h^{-v} (\cos i \cos \alpha_n) \quad (4.12)$$

$$K_{fc} = K_u h^{-u} (\cos \alpha_n \cos \eta) - K_v h^{-v} \sin \alpha_n \quad (4.13)$$

$$K_{rc} = K_u h^{-u} (-\cos i \sin \eta + \sin i \sin \alpha_n \cos \eta) + K_v h^{-v} \sin i \cos \alpha_n \quad (4.14)$$

#### 4.2.6 Generalized Model

In each of the above defined cutting force models, the forces can be generalized into the oblique cutting model with the three principle directions (tangential, feed, and radial) where the cutting coefficients may be constants or functions of other process parameters such as the chip thickness, cutting speed, inclination angle, tool rake angle, etc.

$$F_t = K_{tc}(h, V_c, \dots)a + K_{te}(h, V_c, \dots)b \quad (4.15)$$

$$F_f = K_{fc}(h, V_c, \dots)a + K_{fe}(h, V_c, \dots)b \quad (4.16)$$

$$F_r = K_{rc}(h, V_c, \dots)a + K_{re}(h, V_c, \dots)b \quad (4.17)$$



## 4.3 Cutter-Workpiece Engagement

As evident in the cutting force models, knowledge of the chip geometry is a pre-requisite for calculating the cutting force. Specifically, the undeformed chip area ( $a$ ), thickness ( $h$ ) and width ( $b$ ) must be known. To obtain this information in simulation, the cutter-workpiece engagement (interference) must be calculated and the workpiece geometry must be continuously updated while material is being removed. In the gear shaping operation, it is very difficult to do this analytically as the kinematics are complex, and the cutter and workpiece geometries are complicated. Therefore, a solid modeller is used to compute the cutter-workpiece engagement. There are two different types of solid modellers available: exact modellers, and discrete modellers. Exact modellers (such as boundary representation) represent the solids with exact equations and, in general, offer better accuracy. Discrete modellers (such as multi-dexel representation) represent the solids approximately while offering better speed and robustness. In this analysis, a discrete solid modeller, called ModuleWorks [65], is used. The ModuleWorks engine is a highly optimized solid modeller specifically developed for material removal simulation which uses the multi-dexel representation to model the workpiece.

### 4.3.1 Multi-Dexel Representation

The multi-dexel representation is a method of modelling surfaces and volumes with arrays of parallel line segments (called 'nails') [66]. The nails have points on them which represent where material begin and end. Figure 4.3 shows the dexel representation of a circle. It can be seen that if only a single array of nails is used, curves/surfaces which are near parallel the direction of the nails are not represented well. Therefore, multiple orthogonal sets of nails are used. The two-direction dexel representation of the circle has an improved distribution of points on the curve versus the single-direction representation. In three dimensions, three orthogonal sets of nails are used to represent volumes.

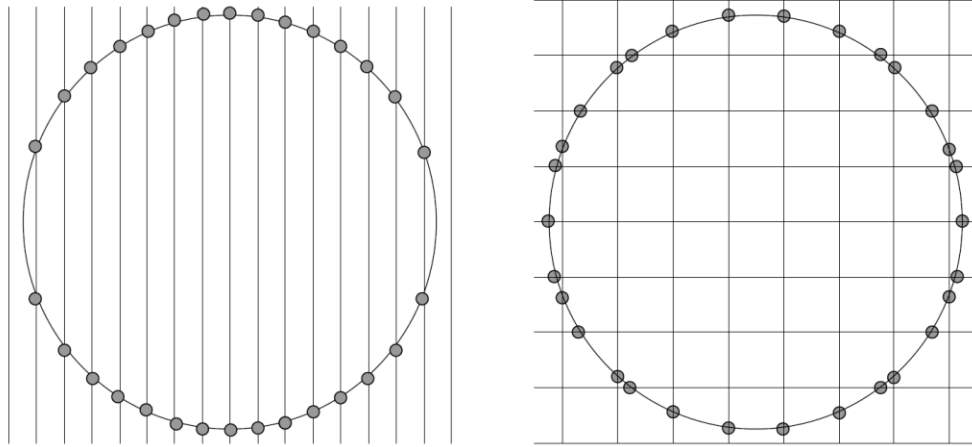


**Figure 4.3:** Single direction and two direction dixel representation of a circle (from [66]).

### 4.3.2 Material Removal Simulation

In the gear shaping simulation, the cutter-workpiece engagement and cutting force is calculated at discrete time steps. Within the ModuleWorks engine, the cutter is represented by a single transverse plane at the bottom of the cutter as seen in Figure 4.4. Using a thin plane at the bottom of the cutter as a representation of the tool allows for the cutter clearance angles to be omitted from the CAD model which decreases simulation time.

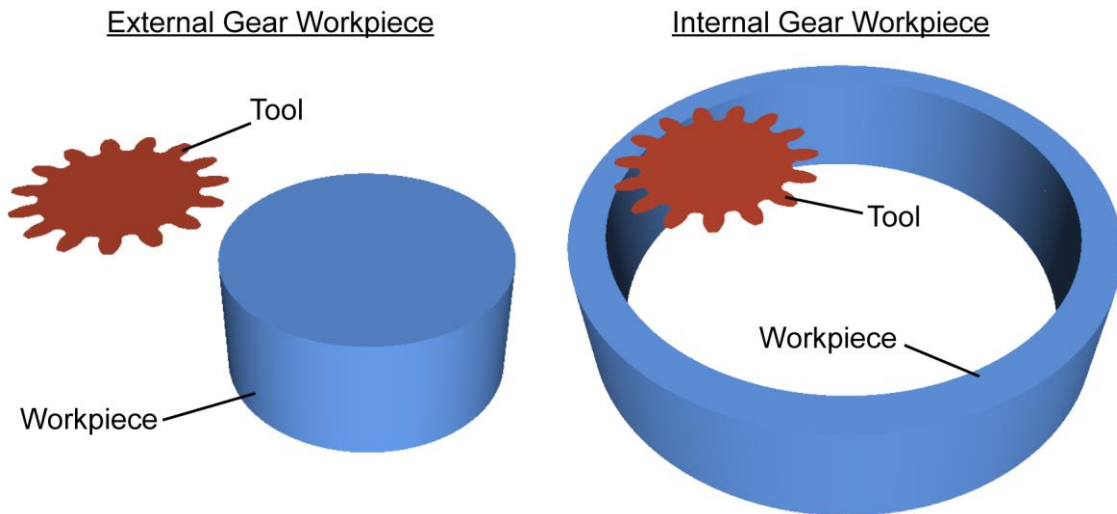


**Figure 4.4:** Tool and workpiece representation in ModuleWorks engine.

To perform the cutter-workpiece engagement calculation with the ModuleWorks engine, the workpiece must be kept stationary and the tool is swept from a starting position to an end position. Therefore, the position of the cutter at the beginning and end of each time step is calculated in the Workpiece Coordinate System using the transformation defined in Equation (3.13). Then, a cutting operation is performed in the engine to obtain the removed material in dixel representation as depicted in Figure 4.5. The nails in the removed material are then analyzed to determine the two-dimensional chip geometry and cutting force which is explained further in Section 4.5.

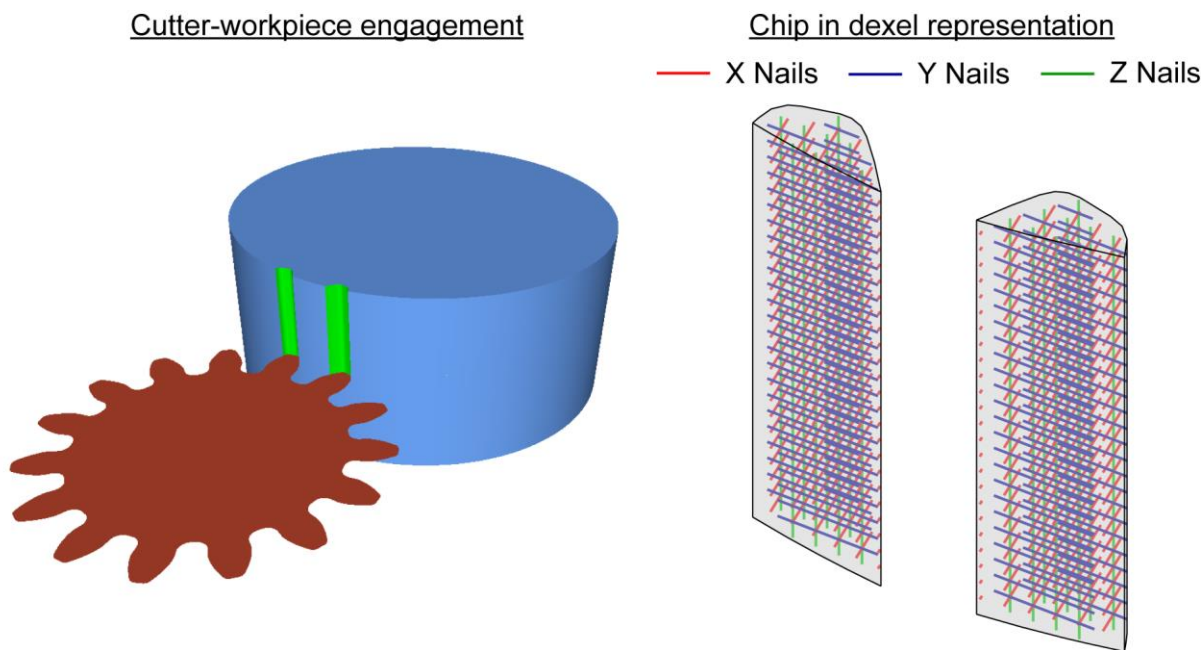


**Figure 4.5:** Cutter-workpiece engagement.

#### 4.4 Tool Edge Discretization

To perform the cutting force prediction, the tool edge is discretized into points called nodes where each node contributes a three dimensional force component per the generalized oblique cutting force model. The geometry of the cutting edge is different for the spur and helical gear shaper cases. However, in both cases the tool edge is first discretized by generating points on the transverse plane of the cutter based on the gear data. Then, the nodes on the transverse plane are modified based on the model of the rake face to obtain the nodes on the cutting edge. Afterwards, the cutting directions (tangential, feed, radial), local inclination angle, and local normal rake angle are determined for each node.

## 4.4.1 Rake Face Model

### 4.4.1.1 Spur Gear Shaper

In spur gear shaping, the rake face is modelled as a downward facing cone where the angle between the gear transverse plane and the rake face is the cutter global rake angle  $\alpha$  as shown in Figure 4.6.

#### Spur gear shaper

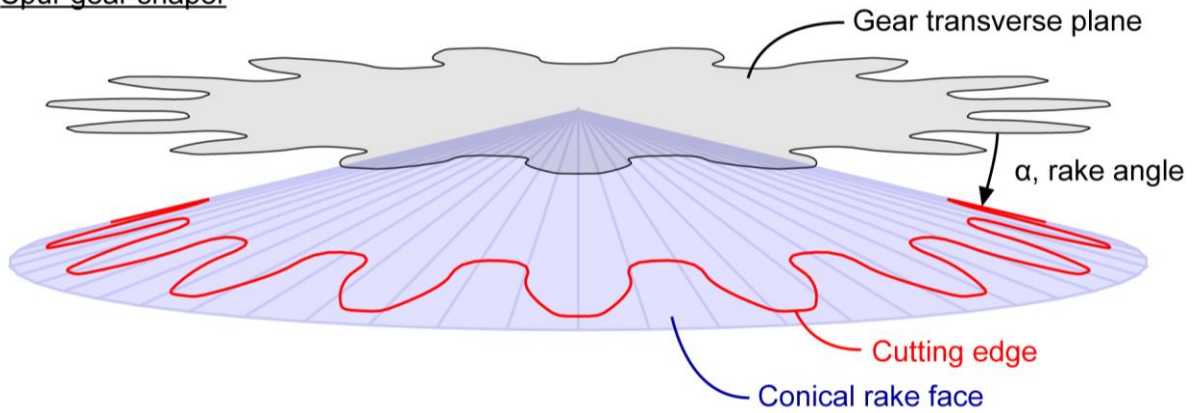


**Figure 4.6:** Rake face model in spur gear shaping.

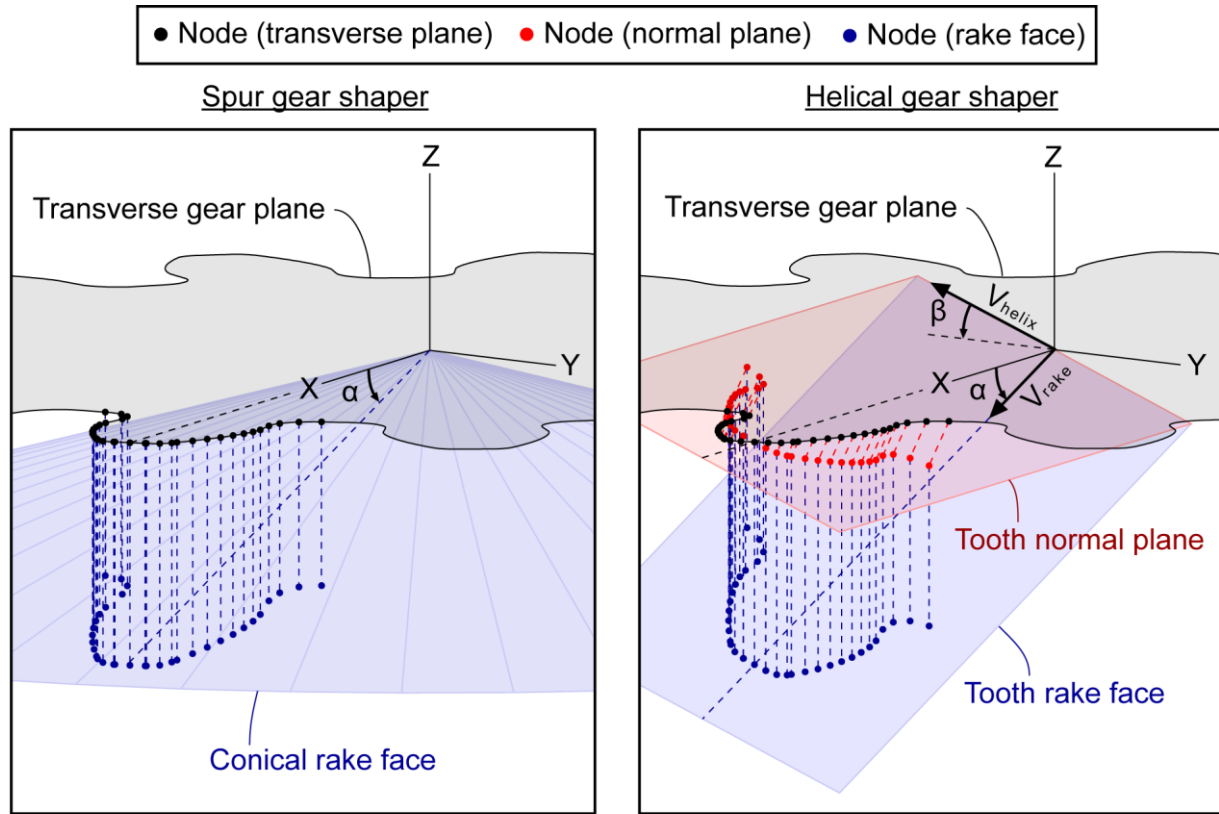


**Figure 4.7:** Projection of transverse nodes onto rake face.

The equation of the cone is simply:

$$z = -\sqrt{x^2 + y^2} \tan \alpha \quad (4.18)$$

Starting from the generated transverse gear profile, the cutting edge can be obtained by the vertical projection of each point onto the conical rake face (shown in Figure 4.7 left). Denoting the location of a node on the transverse profile (in the tool coordinate system) as  $p_t = [x_t \ y_t \ 0]^T$ , the corresponding point on the rake face is:

$$p_r = [x_r \ y_r \ z_r]^T = \left[ x_t \ y_t \ -\sqrt{x_t^2 + y_t^2} \tan \alpha \right]^T \quad (4.19)$$

#### 4.4.1.2 Helical Gear Shaper

In the helical gear shaper case, each tooth has its own rake face which includes the effects of the helix angle and global rake angle of the cutter as seen in Figure 4.8.

### Helical gear shaper

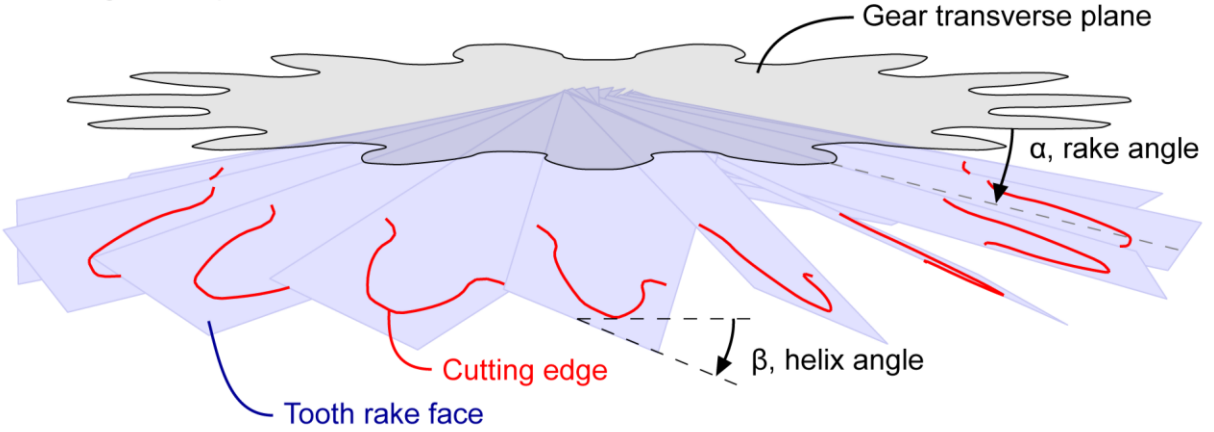


**Figure 4.8:** Rake face model in helical gear shaping.

The transverse nodes are first orthogonally projected onto the normal plane of the tooth to obtain the normal nodes and then vertically projected onto the rake face to obtain the rake face nodes as seen in the right side of Figure 4.7.

The equation of the normal plane for a tooth is given by:

$$\hat{n}_{\text{normal}} \cdot (p_n - p_{\text{normal}}) = 0 \quad (4.20)$$

Here,  $p_n$  is any point on the plane,  $\hat{n}_{\text{normal}}$  and  $p_{\text{normal}}$  define the plane geometry where  $\hat{n}_{\text{normal}}$  is the vector normal to the normal plane, and  $p_{\text{normal}}$  is a point coincident with the plane. In this case,  $p_{\text{normal}} = [0 \ 0 \ 0]^T$  and  $\hat{n}_{\text{normal}}$  is determined as:

$$\begin{aligned} \hat{n}_{\text{normal}} &= R_{\text{tooth}} \hat{n}_{\text{normal},0} = R_{\text{tooth}} (\hat{V}_{\text{helix}} \times \hat{X}) \\ &= \begin{bmatrix} \cos \gamma & -\sin \gamma & 0 \\ \sin \gamma & \cos \gamma & 0 \\ 0 & 0 & 1 \end{bmatrix} \left( \begin{bmatrix} 0 \\ -\cos \beta \\ \sin \beta \end{bmatrix} \times \begin{bmatrix} 1 \\ 0 \\ 0 \end{bmatrix} \right) \\ &= \begin{bmatrix} -\sin \beta \sin \gamma \\ \sin \beta \cos \gamma \\ \cos \beta \end{bmatrix} \end{aligned} \quad (4.21)$$

Here,  $\beta$  is the helix angle of the cutter.  $R_{\text{tooth}}$  is the yaw rotation matrix for the particular tooth; hence,  $\gamma$  defines the angle of the tooth on the transverse plane measured from the  $x$  axis to the tip of the tooth as illustrated in Figure 4.9.  $\hat{n}_{\text{normal},0}$  is the normal vector of the normal plane for a tooth where  $\gamma = 0$ . This is

determined by the cross product of the  $x$  axis and  $\hat{V}_{\text{helix}} = [0 \quad -\cos \beta \quad \sin \beta]^T$ , which are both vectors that are coincident with the normal plane (illustrated in Figure 4.7 right).

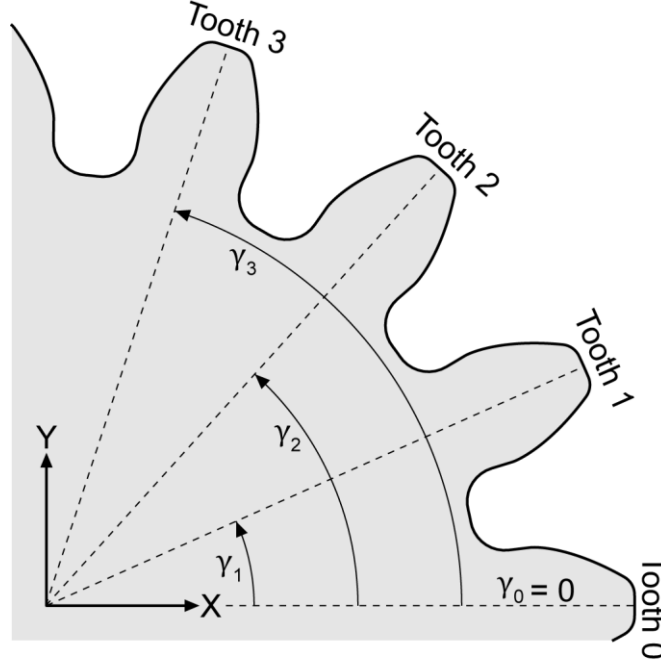


**Figure 4.9:** Illustration of tooth angle ( $\gamma$ ).

To perform the orthogonal projection of the transverse nodes onto the normal plane of the tooth, the following projection is used:

$$p_n = [x_n \quad y_n \quad z_n]^T = p_t - [(p_t - p_{\text{normal}}) \cdot \hat{n}_{\text{normal}}] \hat{n}_{\text{normal}} \quad (4.22)$$

The equation of the rake plane of the tooth which also has the effect of the cutter's global rake angle ( $\alpha$ ) is, given by:

$$\hat{n}_{\text{rake}} \cdot (p_r - p_{\text{rake}}) = 0 \quad (4.23)$$

$p_{\text{rake}} = [0 \quad 0 \quad 0]^T$  is a point coincident with the plane, and  $\hat{n}_{\text{rake}}$  is the vector normal to the plane which is determined by:

$$\begin{aligned}
\hat{n}_{\text{rake}} &= R_{\text{tooth}} \hat{n}_{\text{rake},0} = R_{\text{tooth}} (\hat{V}_{\text{helix}} \times \hat{V}_{\text{rake}}) \\
&= \begin{bmatrix} \cos \gamma & -\sin \gamma & 0 \\ \sin \gamma & \cos \gamma & 0 \\ 0 & 0 & 1 \end{bmatrix} \left( \begin{bmatrix} 0 \\ -\cos \beta \\ \sin \beta \end{bmatrix} \times \begin{bmatrix} \cos \alpha \\ 0 \\ -\sin \alpha \end{bmatrix} \right) \\
&= \begin{bmatrix} \cos \beta \cos \gamma \sin \alpha - \cos \alpha \sin \beta \sin \gamma \\ \cos \alpha \cos \gamma \sin \beta + \cos \beta \sin \alpha \sin \gamma \\ \cos \alpha \cos \beta \end{bmatrix} \\
&= \begin{bmatrix} n_{\text{rake},x} \\ n_{\text{rake},y} \\ n_{\text{rake},z} \end{bmatrix}
\end{aligned} \tag{4.24}$$

Similarly,  $\hat{n}_{\text{rake},0}$  is the normal vector of the rake plane for a tooth with  $\gamma = 0$  which is determined by the cross product of two vectors coincident with the plane ( $\hat{V}_{\text{helix}} = [0 \quad -\cos \beta \quad \sin \beta]^T$  and  $\hat{V}_{\text{rake}} = [\cos \alpha \quad 0 \quad -\sin \alpha]^T$ , shown in Figure 4.7 right).

Using the equation of the plane, the vertical projection of the normal nodes onto the rake plane can be performed to obtain the rake face nodes:

$$p_r = [x_r \quad y_r \quad z_r]^T = \left[ x_n \quad y_n \quad -\frac{n_{\text{rake},x} x_n + n_{\text{rake},y} y_n}{n_{\text{rake},z}} \right]^T \tag{4.25}$$

#### 4.4.2 Cutting Direction Calculation

In the generalized cutting force model, the tangential, feed, and radial direction must be determined which is a function of the cutting edge geometry and the cutting velocity relative to the workpiece. The cutting velocity  $\bar{V}_c$  of the tool is a combination of the three different kinematic components:

$$\bar{V}_c(t) = \underbrace{\bar{V}_{\text{rad}}(t)}_{\text{radial feed}} + \underbrace{\bar{V}_{\text{rot}}(t)}_{\text{rotary feed}} + \underbrace{\bar{V}_{\text{rec}}(t)}_{\text{reciprocating}} \tag{4.26}$$

##### 4.4.2.1 Spur Gear Shaping

In spur gear shaping, it can be seen that the magnitude of the radial feed and rotary feed are 2-3 orders of magnitude smaller than the reciprocating motion. For a typical cutting pass (e.g.  $f_{\text{cut}} = 400$ ,  $f_{\text{rotary}} = 0.2$  feed,  $f_{\text{radial, start}} = f_{\text{radial, end}} = 0.1$ , and  $d_{\text{stroke}} = 30$ ), the average cutting speed due to reciprocating motion is 400 mm/s, the average tangential velocity due to the rotary feed of the cutter is 1.3 mm/s, and the velocity due to the infeed motion is 0.67 mm/s. Therefore, the radial and rotary feed can be ignored and the cutting velocity can be approximated as:



$$\bar{V}_c(t) \cong \bar{V}_{rec}(t) = \left[ 0 \quad 0 \quad \frac{dz(t)}{dt} \right]^T \quad (4.27)$$

$$\frac{dz(t)}{dt} = \frac{d(d_{top} - 0.5d_{stroke}(1 - \cos(\omega_s t)))}{dt} = -0.5\omega_s d_{stroke} \sin(\omega_s t) \quad (4.28)$$

Since cutting only occurs during the down stroke, the unit vector of the cutting velocity ( $\hat{V}_c$ ) is constant for every node location (shown in Figure 4.10):

$$\hat{V}_c = [0 \quad 0 \quad -1]^T \text{ (spur case)} \quad (4.29)$$

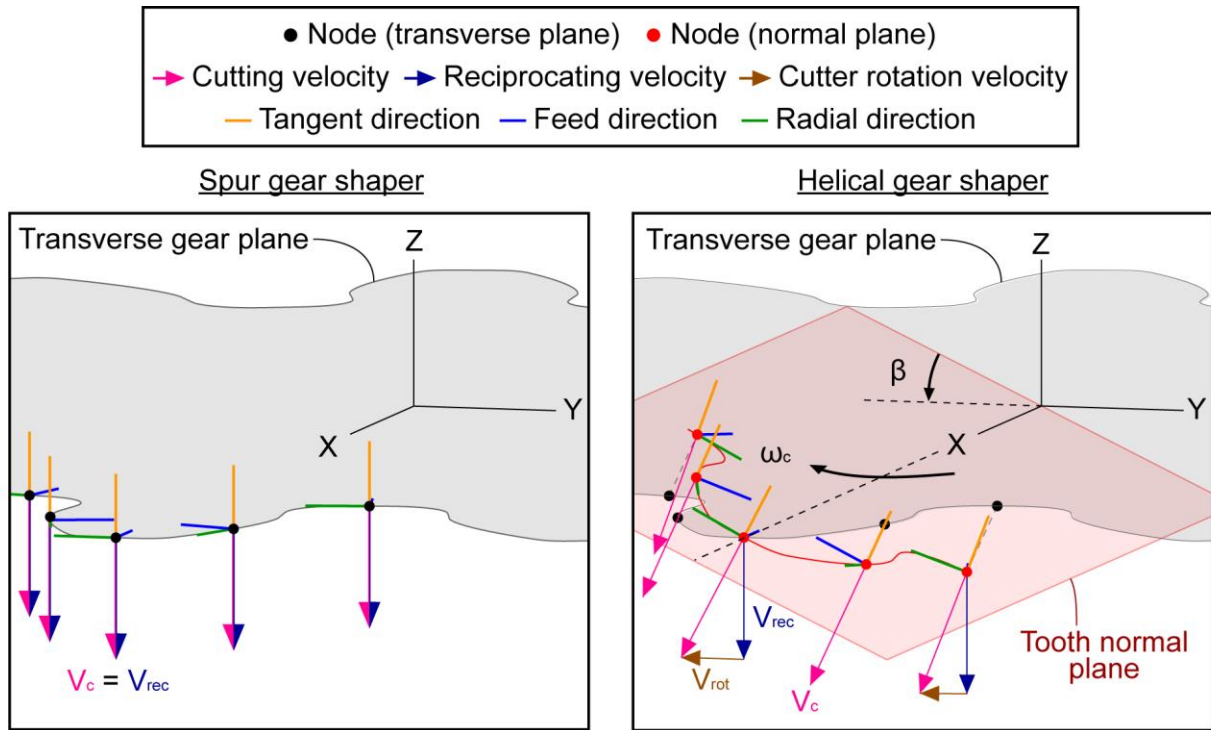


**Figure 4.10:** Cutting velocity and directions in spur and helical shaping.

#### 4.4.2.2 Helical Gear Shaping

In helical gear shaping, there is additional tool rotation due to the helical engagement of the tool and workpiece. In this case, the magnitude of the helical component is significant. The rotation of the cutter relative to the gear workpiece is:

$$\phi_{cg}(t) = \phi_c(t) - \phi_g(t) = - \underbrace{\frac{\epsilon \omega_g}{R} t}_{\text{rotary feed of cutter}} + \underbrace{\frac{z(t) \tan \beta}{r_{pc}}}_{\text{helical component}} - \underbrace{\omega_g t}_{\text{rotary feed of gear}} \cong \frac{z(t) \tan \beta}{r_{pc}} \quad (4.30)$$

The angular velocity of the cutter relative to the gear is then:

$$\omega_{cg}(t) = \frac{d\phi_{cg}(t)}{dt} \cong \frac{\frac{dz(t)}{dt} \tan \beta}{r_{pc}} \quad (4.31)$$

For rake node location  $p_r = [x_r \ y_r \ z_r]^T$ , the tangential velocity due to the rotation of the tool is:

$$\bar{V}_{\text{rot}}(t) = \underbrace{\sqrt{x_r^2 + y_r^2}}_{\text{radial distance to node location}} \underbrace{\frac{\frac{dz(t)}{dt} \tan \beta}{r_{pc}}}_{\text{angular velocity}} \underbrace{\frac{[-y_r \ x_r \ 0]^T}{\sqrt{x_r^2 + y_r^2}}}_{\text{tangential unit vector}} = \frac{\frac{dz(t)}{dt} \tan \beta}{r_{pc}} [-y_r \ x_r \ 0]^T \quad (4.32)$$

Then, the total cutting velocity is:

$$\begin{aligned} \bar{V}_c &\cong \bar{V}_{\text{rot}}(t) + \bar{V}_{\text{rec}}(t) = \frac{\frac{dz(t)}{dt} \tan \beta}{r_{pc}} [-y_r \ x_r \ 0]^T + \left[ 0 \ 0 \ \frac{dz(t)}{dt} \right]^T \\ &= \frac{dz(t)}{dt} \left[ \frac{-y_r \tan \beta}{r_{pc}} \ \frac{x_r \tan \beta}{r_{pc}} \ 1 \right]^T \end{aligned} \quad (4.33)$$

Therefore, the unit vector of the cutting velocity will be constant for each node (in the tool coordinate system) regardless of the value of  $dz(t)/dz$ . Since cutting always occurs in the negative  $z$  direction, the unit vector of the cutting velocity is:

$$\hat{V}_c = \frac{\begin{bmatrix} \frac{y_r \tan \beta}{r_{pc}} & \frac{-x_r \tan \beta}{r_{pc}} & -1 \end{bmatrix}}{\sqrt{\left(\frac{y_r \tan \beta}{r_{pc}}\right)^2 + \left(\frac{-x_r \tan \beta}{r_{pc}}\right)^2 + 1}} \quad (\text{helical case}) \quad (4.34)$$

It is noteworthy that the tangential velocity due to tool rotation is different for each node location. Nodes that are farther away from the axis of rotation will have larger tangential velocity than nodes which are closer (seen in Figure 4.10) and therefore, each node also has a different cutting velocity vector.

#### 4.4.2.3 Tangential, Feed, and Radial Direction Calculation

In both the helical and spur cases, the cutting directions for each node are calculated with the same procedure given the knowledge of the cutting velocity and rake node location. The location of the current

node is denoted by  $p_{0,r}$ , the location of the next node is denoted by  $p_{1,r}$ , and the location of the previous node is denoted by  $p_{-1,r}$  as shown in Figure 4.11.

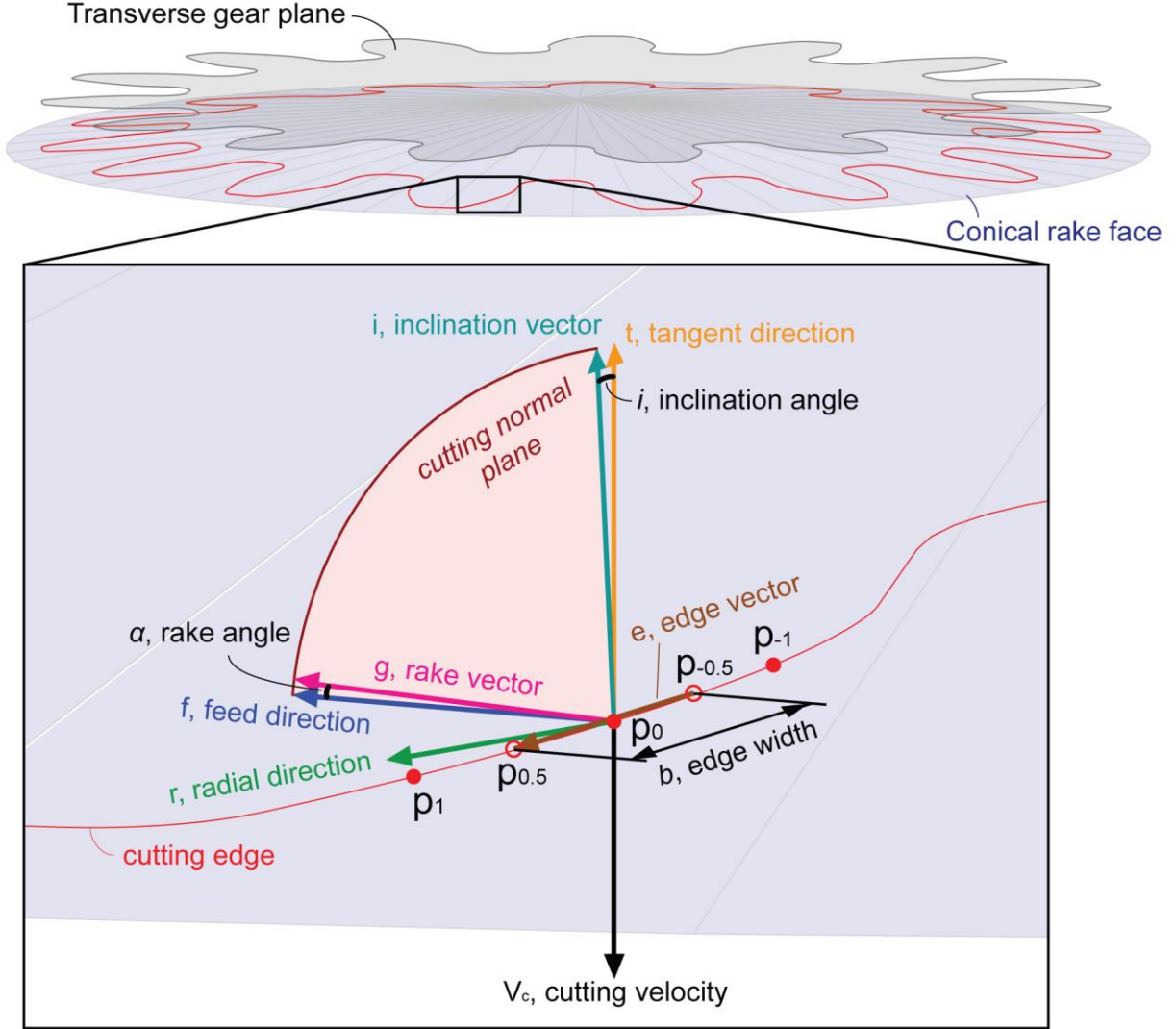


**Figure 4.11:** Cutting direction calculation.

$p_{0.5,r}$  and  $p_{-0.5,r}$  are midpoint nodes which are calculated as follows:

$$\begin{aligned}
 p_{0.5,r} &= \frac{(p_{1,r} + p_{0,r})}{2} \\
 p_{-0.5,r} &= \frac{(p_{0,r} + p_{-1,r})}{2}
 \end{aligned}
 \tag{4.35}$$

The tangent direction  $\hat{t}$  is defined opposite to the cutting velocity unit vector:

$$\hat{t} = -\hat{V}_c \quad (4.36)$$

An edge vector  $\bar{e}$  and unit edge vector  $\hat{e}$  is defined which adjoins the two midpoints:

$$\bar{e} = p_{0.5} - p_{-0.5}, \quad \hat{e} = \frac{\bar{e}}{\|\bar{e}\|} \quad (4.37)$$

With the assumption that the node locations are ordered in a clockwise manner around the axis of rotation, the feed direction  $\hat{f}$  is orthogonal to the edge vector and tangent direction:

$$\hat{f} = \hat{e} \times \hat{t} \quad (4.38)$$

Next, an inclination vector  $\hat{i}$  is defined as orthogonal to the feed vector and edge vector:

$$\hat{i} = \hat{f} \times \hat{e} \quad (4.39)$$

Accordingly, the inclination angle  $i$  can be calculated as the angle between the inclination vector and tangent direction

$$i = \text{acos}(\hat{i} \cdot \hat{t}) \quad (4.40)$$

The radial direction  $\hat{r}$  is calculated as orthogonal to the tangential and feed directions, however care must be taken to flip the radial direction if necessary:

$$\hat{r} = \hat{t} \times \hat{f}, \quad \text{if } \hat{r} \cdot \hat{i} < 0 \Rightarrow \hat{r} = -\hat{r} \quad (4.41)$$

The edge width  $b$  is calculated as the length of the edge vector projected onto the radial direction:

$$b = \|\bar{e}\| \cos i \quad (4.42)$$

Finally, the normal rake angle  $\alpha_n$  is defined as the angle between the feed direction and rake face on the cutting normal plane where the cutting normal plane is the plane normal to the cutting edge. A rake vector  $\hat{g}$  is defined which is the vector that intersects the cutting normal plane and rake face. The normal rake angle is then calculated as the angle between the rake vector and feed direction, with care being taken for the negative rake angle case:

$$\alpha_n = \text{acos}(\hat{g} \cdot \hat{f}), \quad \text{if } \hat{g} \cdot \hat{i} < 0 \Rightarrow \alpha_n = -\alpha_n \quad (4.43)$$

The rake vector is calculated differently for the spur and helical shaping cases. For the spur shaping case, since the rake face is a cone, the rake vector must be approximated locally (i.e. the rake face is a curved surface). To do the approximation, a ghost point  $p_g$  is determined which lies on the rake face and cutting

normal plane, then the rake vector is calculated by adjoining the ghost point and node location as illustrated in Figure 4.12.

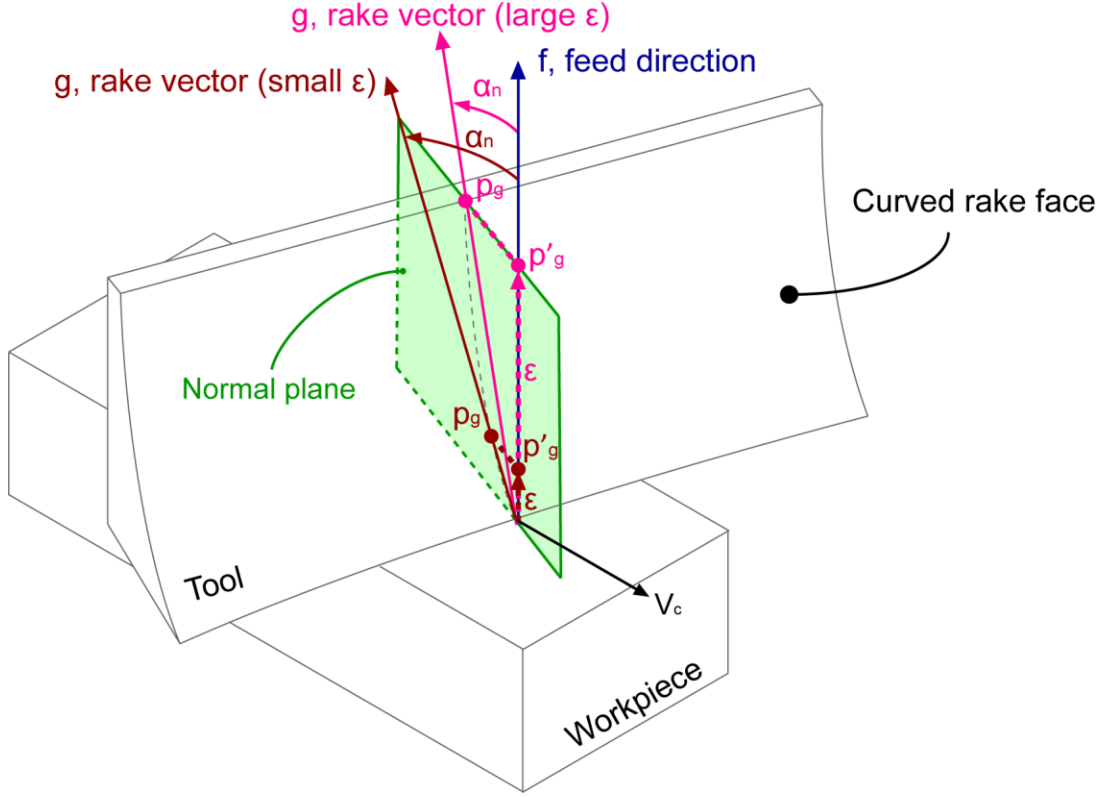


**Figure 4.12:** Local approximation of normal rake angle for curved rake face.

The ghost point is calculated by first perturbing the node location a small amount ( $\epsilon$ ) in the feed direction:

$$p'_g = p_{0,r} + \epsilon \hat{f} \quad (4.44)$$

Then, the z coordinate is adjusted to be on the rake face:

$$p'_{gz} = -\tan \alpha \sqrt{p'_{gx}{}^2 + p'_{gy}{}^2} \quad (4.45)$$

Finally, the point is orthogonally projected onto the cutting normal plane to obtain the ghost point:

$$p_g = p'_g - ((p'_g - p_{0,r}) \cdot \hat{e}) \hat{e} \quad (4.46)$$

$$\bar{g} = p_g - p_{0,r}, \quad \hat{g} = \frac{\bar{g}}{\|\bar{g}\|} \text{ (spur case)} \quad (4.47)$$

Based on the value of  $\varepsilon$ , different values for the normal rake angle will be obtained as seen in Figure 4.12. In this case, a small  $\varepsilon$  (0.000001) is used to obtain the approximation of the normal rake angle close to the cutting edge.

For the helical shaping case, the rake face is a plane so the rake vector can be calculated analytically:

$$\hat{g} = \underbrace{\hat{n}_{\text{rake}}}_{\text{normal vector of rake face}} \times \underbrace{\hat{e}}_{\text{normal vector of cutting normal plane}} \quad (\text{helical case}) \quad (4.48)$$

Figure 4.13 show how the local rake angle and inclination angles vary along the cutting edge in a spur and helical gear shaper case. In general, there is high rake angle and low inclination angle at the tip and root of the teeth while there is low rake angle and high inclination angle on the flanks of the teeth.

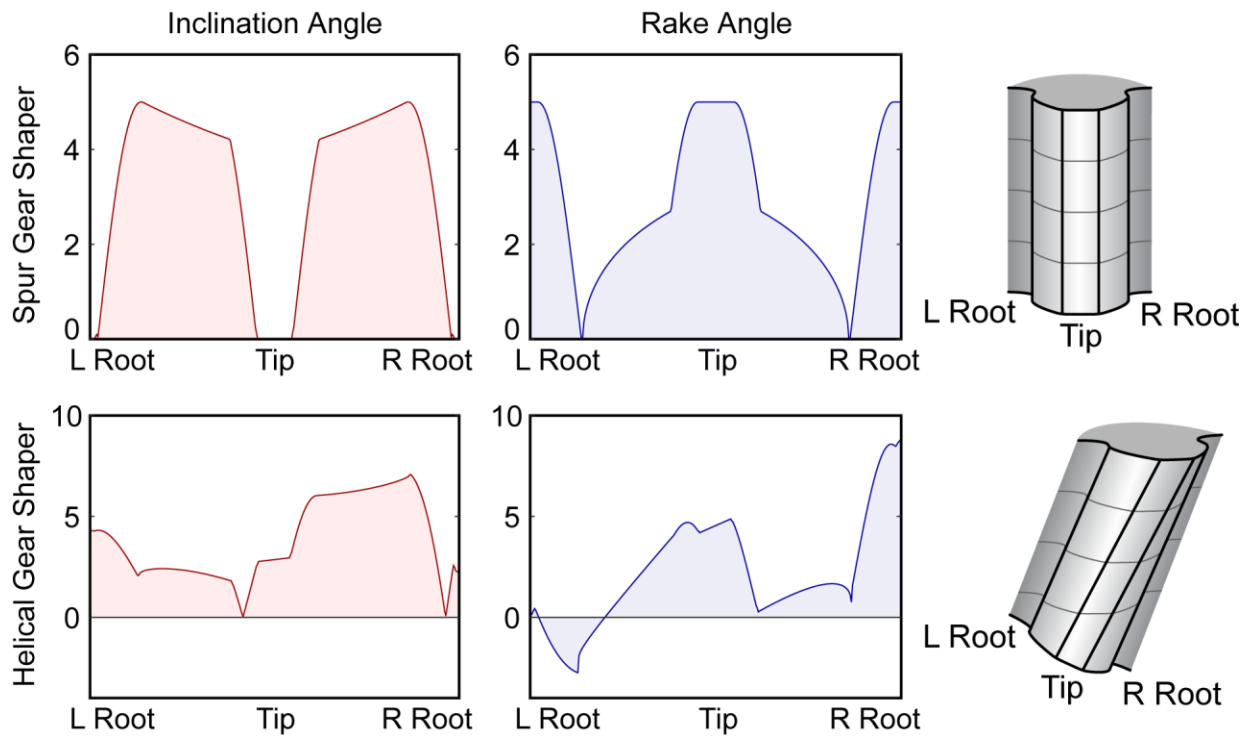


**Figure 4.13:** Distribution of inclination and rake angles on single gear tooth with cutter rake angle of  $5^\circ$  and helical angle of  $25^\circ$  in helical gear shaper case.

## 4.5 Force Calculation

Since the cutting force model is a function of the chip thickness and width, the chip geometry must be analyzed on a two-dimensional plane. The chip cross-section is constructed on the plane normal to the Z-

axis at the dixel height closest to the midpoint of the tool movement during the time step. As seen in Figure 4.14 which shows a typical chip generated during a helical shaping case, the chip cross-section can change drastically throughout the movement of the tool during a time step, therefore analyzing the chip at the middle of the tool movement gives the best representation of the average chip cross-section.

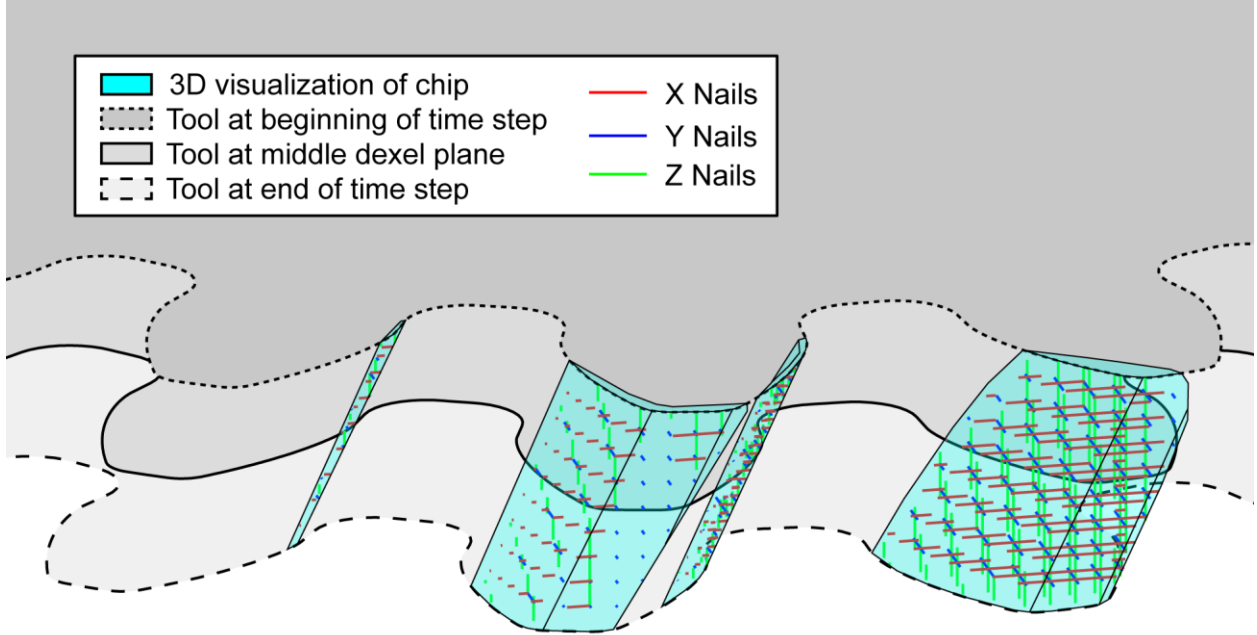


**Figure 4.14:** Typical chip geometry in helical gear shaping case.

To reconstruct the chip cross-section from the dixel format, a point cloud is generated on the construction plane which includes the end points of each X and Y nail on the plane, the intersection of the Z nails on the plane, and the engaged nodes along the tool edge (Figure 4.15a). The engaged nodes include any nodes on the tool which are within a certain distance to any of the X and Y nail endpoints or Z nail intersections. The distance threshold is chosen to be the dixel precision ( $d_{\text{dixel}}$ ) which is the distance between two adjacent nails. Here, the transverse node locations are used since the tool is represented with a transverse plane in the CWE calculation. However, since the node geometry is defined in the TCS (see previous section) and the CWE is in the WCS, the node locations are transformed into the WCS:

$$\begin{array}{c} \begin{bmatrix} p_t^{WCS} \\ 1 \end{bmatrix} \\ \text{transverse node} \\ \text{location in WCS} \end{array} = \begin{array}{c} \underline{T_{TCS}^{WCS}} \\ \text{transform} \\ \text{between tool} \\ \text{and workpiece} \end{array} \begin{array}{c} \begin{bmatrix} p_t^{TCS} \\ 1 \end{bmatrix} \\ \text{transverse node} \\ \text{location in TCS} \end{array} \quad (4.49)$$

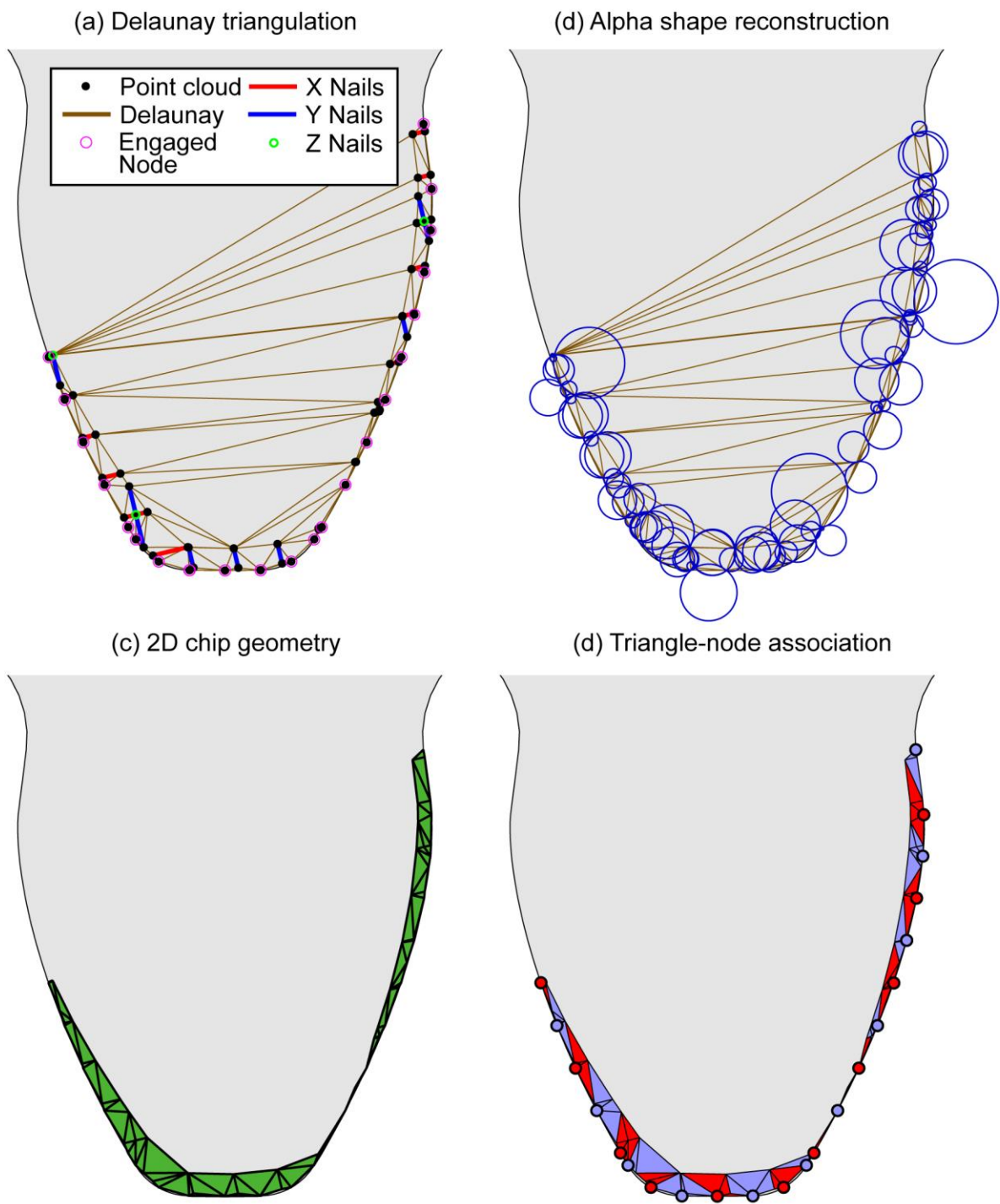


**Figure 4.15:** Reconstruction of two-dimensional chip cross-section.



From the point cloud on the plane, the chip geometry is reconstructed using the alpha shape method [67]. Alpha shapes is a method for determining the shape of a set of points on a plane. To determine the alpha shape of the point cloud, the Delaunay triangulation (DT) is first calculated. The DT is defined as the non-overlapping triangulation of the set of points in which the circumscribed circle of each triangle does not contain any other point [68]. This results in the triangulation with the fewest number of thin triangles. There are many algorithms for calculating the DT which offer varying levels of speed and robustness. In this case, the Bowyer-Watson algorithm [69] is implemented due to its simplicity and robustness. In this algorithm, each point is incrementally inserted into a “super” triangle which encompasses the bounds of the point cloud. During each insertion, each triangle within the existing triangulation whose circumscribed circle contains the inserted point is removed from the triangulation. Then, each vertex from the removed triangles is re-triangulated with the inserted point to obtain a valid DT. After all the points are inserted, the triangles which contain the vertices of the “super” triangle are removed. The location  $(x_c, y_c)$  and radius  $(r_c)$  of the circumscribed circle of a triangle given the coordinates of the three vertices on a plane can be calculated as [70]:

$$\begin{aligned}
 x_c &= \frac{(x_0^2 + y_0^2)(y_2 - y_1) + (x_1^2 + y_1^2)(y_0 - y_2) + (x_2^2 + y_2^2)(y_1 - y_0)}{2(x_0(y_2 - y_1) + x_1(y_0 - y_2) + x_2(y_1 - y_0))} \\
 y_c &= \frac{(x_0^2 + y_0^2)(x_1 - x_2) + (x_1^2 + y_1^2)(x_2 - x_0) + (x_2^2 + y_2^2)(x_0 - x_1)}{2(x_0(y_2 - y_1) + x_1(y_0 - y_2) + x_2(y_1 - y_0))} \\
 r_c &= \sqrt{(x_c - x_0)^2 + (y_c - y_0)^2}
 \end{aligned} \tag{4.50}$$

Once the DT of the point cloud is obtained, the alpha shape is determined by removing any triangles whose circumscribed circle’s radius is larger than the alpha distance  $d_\alpha$ . In this case, the alpha threshold is chosen to be  $d_\alpha = \sqrt{2}d_{\text{dixel}}$ . Figure 4.15b shows the circumscribed circles of the triangles that are part of the alpha shape for that particular case. The triangles in the alpha shape form the geometry of the chip cross-section (Figure 4.15c).

Each triangle in the alpha shape is associated to the tool node that is closest to the centroid of that triangle as shown in Figure 4.15d.

In the cutting force model, the undeformed chip characteristics (area, thickness, width) are defined on the plane normal to the tangential direction. In the helical gear shaping case, the tangential direction is not coincident with the Z axis, however the alpha shape is constructed on the plane normal to the Z axis.

Therefore, the triangles of the alpha shape must be orthogonally projected onto the plane normal to the tangent direction as depicted in the left side of Figure 4.16 before calculating the undeformed chip area.

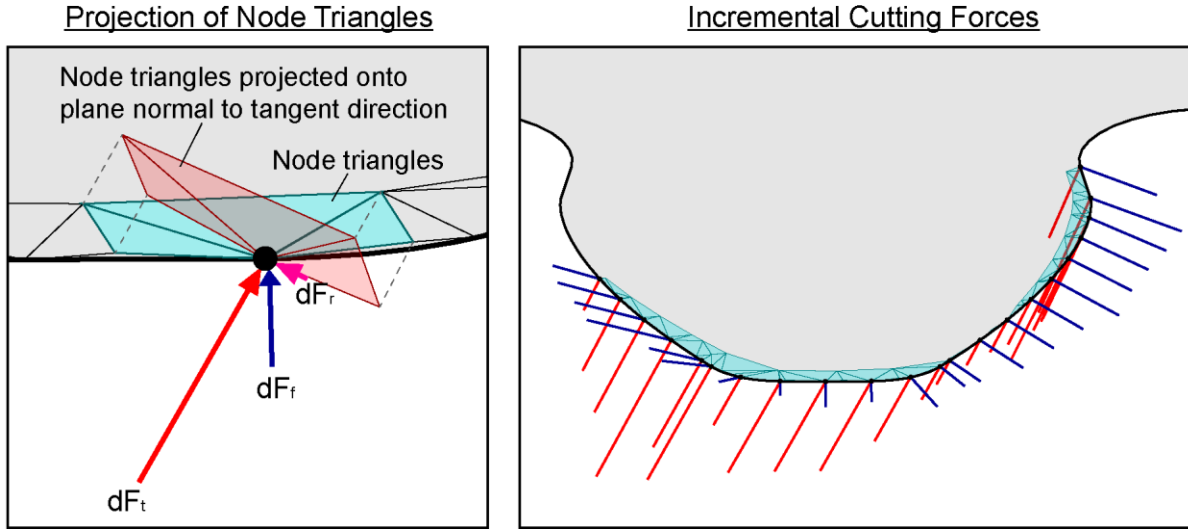


**Figure 4.16:** Projection of triangles onto plane normal to tangential direction.

The summation of the area of each triangle associated to a node comprise the undeformed chip area which is used to calculate the incremental tangential, feed, and radial forces. The area of a triangle ( $\Delta$ ) in three dimensions given the coordinates of the three vertices can be calculated using Heron's formula [71]:

$$\begin{aligned}
 \Delta &= \sqrt{s(s - l_{01})(s - l_{02})(s - l_{12})} \\
 l_{01} &= \sqrt{(x_0 - x_1)^2 + (y_0 - y_1)^2 + (z_0 - z_1)^2} \\
 l_{02} &= \sqrt{(x_0 - x_2)^2 + (y_0 - y_2)^2 + (z_0 - z_2)^2} \\
 l_{12} &= \sqrt{(x_1 - x_2)^2 + (y_1 - y_2)^2 + (z_1 - z_2)^2} \\
 s &= (l_{01} + l_{02} + l_{12})/2
 \end{aligned} \tag{4.51}$$

The incremental tangential, feed, and radial forces ( $dF_t$ ,  $dF_f$ ,  $dF_r$ ) for each node are then calculated (Figure 4.16 right) with the below formula which coincides with the generalized oblique cutting model. The chip thickness, which may be a parameter in the cutting coefficient, is estimated by dividing the chip area with the chip width ( $h = a/b$ ).

$$dF_{t,f,r} = K_{(t,f,r)c}(h, |\bar{V}_c|, \dots) \left( \underbrace{\sum_{\substack{\text{associated} \\ \text{triangles} \\ a, \text{ chip area}}} \Delta} \right) + K_{(t,f,r)e}(h, |\bar{V}_c|, \dots) b \quad (4.52)$$

Finally, the total cutting force for a time step is determined by integrating the incremental cutting forces from each node:

$$\bar{F}^{WCS} = \sum_{\substack{\text{engaged} \\ \text{nodes}}} (dF_t \hat{t}^{WCS} + dF_f \hat{f}^{WCS} + dF_r \hat{r}^{WCS}) \quad (4.53)$$

In the previous section, the tangential, feed, and radial directions were defined in the TCS, therefore they must be rotated into the WCS:

$$\underbrace{\hat{t}^{WCS}}_{\substack{\text{tangential} \\ \text{vector in WCS}}} = \underbrace{R_{TCS}^{WCS}}_{\substack{\text{rotation matrix} \\ \text{between tool} \\ \text{and workpiece}}} \underbrace{\hat{t}^{TCS}}_{\substack{\text{tangential} \\ \text{vector in TCS}}} \quad (4.54)$$

$$\hat{f}^{WCS} = R_{TCS}^{WCS} \hat{f}^{TCS}, \quad \hat{r}^{WCS} = R_{TCS}^{WCS} \hat{r}^{TCS}$$

## 4.6 Experimental Validation

Experimental validation of the cutting force prediction algorithm has been carried out by defining several different case studies designed to validate the model for different types of gears, processes, and materials. Cutting force measurements have been recorded during the generation of internal spur gears, external spur gears, and external helical gears. In each case, two different processes were tested (a single pass process, and a two-pass process with a roughing and finishing pass). The gear data and process parameters for the internal gear case study can be found in Table 4.1 and the workpiece/tool can be seen in Figure 4.17. In this case, two different workpiece materials were tested (AISI 1141 and 5130 steels) and the tool material is PM-HSS with Balinit® Alcrona Pro coating. Similarly, the process parameters for the external spur and external helical cases can be found in Table 4.2 and Table 4.3, and the workpiece/tools can be seen in Figure 4.18 and Figure 4.19. In both the external spur and external helical cases, the workpiece material is AISI 8620 steel. The tool material for the external spur case is PM-HSS with Balinit® Alcrona Pro coating, and the tool material for the external helical case is S390 steel with Balinit® Alcrona Pro coating. All of the tools used in the experiments have a rake angle of 5 degrees.

**Table 4.1:** Cutting pass parameters and gear data for internal spur case study.

Gear Data		Cutting Pass Parameters		
$\epsilon$	-1 (internal gear)	One-pass	Two-pass	
$m_n$ [mm]	1.5875	$f_{cut}$ [DS/min]	350	450
$\psi_n$ [deg]	25	$f_{rotary}$ [mm/DS]	0.5	0.5
$\beta$ [deg]	0	$f_{radial, start}$ [mm/DS]	0.01	0.01
$N_c$	50	$f_{radial, end}$ [mm/DS]	0.01	0.0041
$N_g$	121	$r_{start}$ [mm]	52.75	56.609
$b$	34.85	$r_{end}$ [mm]	56.89	56.89
$r_{ac}$	41.26	$d_{top}$ [mm]	2.54	2.54
$r_{ag}$	94.2	$d_{bottom}$ [mm]	2.54	2.54
$x_c$	0.0*			

\*tool profile modification coefficient was unfortunately not measured during this trial and assumed zero in simulation

**Table 4.2:** Cutting pass parameters and gear data for external spur case study.

Gear Data		Cutting Pass Parameters		
$\epsilon$	1 (external gear)	One-pass	Two-pass	
$m_n$ [mm]	5.08	$f_{cut}$ [DS/min]	400	400
$\psi_n$ [deg]	22.5	$f_{rotary}$ [mm/DS]	0.5	1
$\beta$ [deg]	0	$f_{radial, start}$ [mm/DS]	0.1	0.025
$N_c$	28	$f_{radial, end}$ [mm/DS]	0.025	0.025
$N_g$	22	$r_{start}$ [mm]	137.111	128.561
$b$	25.4	$r_{end}$ [mm]	128.361	128.361
$r_{ac}$ [mm]	77.2	$d_{top}$ [mm]	2.54	2.54
$r_{ag}$ [mm]	60.875	$d_{bottom}$ [mm]	2.54	2.54
$x_c$	0.17			

**Table 4.3:** Cutting pass parameters and gear data for external helical case study.

Gear Data		Cutting Pass Parameters		
$\epsilon$	1 (external gear)	One-pass	Two-pass	
$m_n$ [mm]	2.1167	$f_{cut}$ [DS/min]	300	300
$\psi_n$ [deg]	20	$f_{rotary}$ [mm/DS]	0.8	0.5
$\beta$ [deg]	-20	$f_{radial, start}$ [mm/DS]	0.1	0.1
$N_c$	36	$f_{radial, end}$ [mm/DS]	0.025	0.025
$N_g$	52	$r_{start}$ [mm]	103.03	98.343
$b$	50	$r_{end}$ [mm]	98.243	98.243
$r_{ac}$ [mm]	43.065	$d_{top}$ [mm]	5	5
$r_{ag}$ [mm]	60.875	$d_{bottom}$ [mm]	5	5
$x_c$	-0.06			

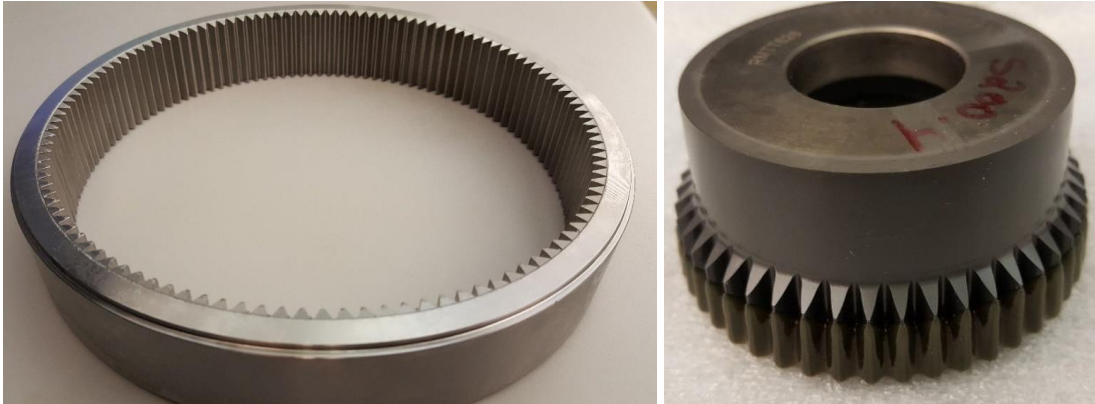


**Figure 4.17:** Finished workpiece (left) and tool (right) for internal spur gear case study.



**Figure 4.18:** Finished workpiece (left) and tool (right) for external spur gear case study.

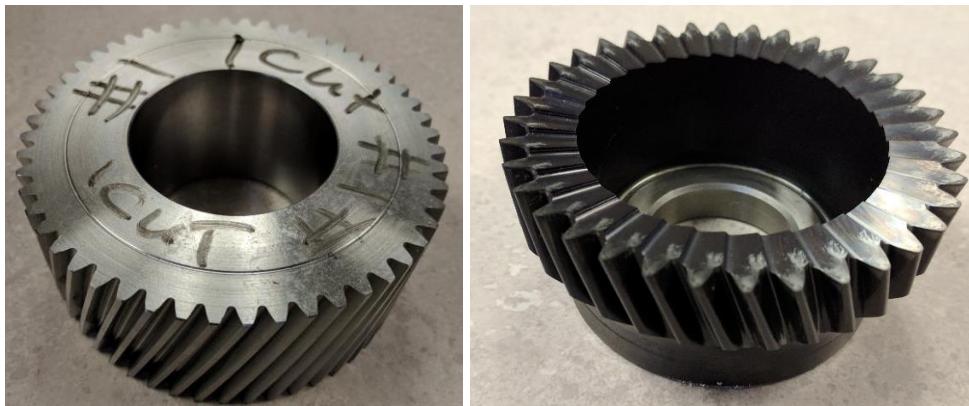


**Figure 4.19:** Finished workpiece (left) and tool (right) for external helical gear case study.

#### 4.6.1 Experimental Setup

To measure the cutting forces, a Kistler 9255A 3-axis dynamometer is mounted on the Liebherr LSE500 gear worktable. Hence, the measured cutting forces are in the workpiece coordinate system. A custom fixture was designed and built for the internal gear workpiece (seen in Figure 4.20) complete with a centering fixture and chip evacuation port. For the external gears, a collet fixture was used as seen in Figure 4.21. During the cutting, oil lubricant is used very heavily, so the dynamometer is wrapped in plastic to avoid contamination. Before each experiment, the dynamometer cable is wrapped around the worktable several times and put under tension such that the cable unwraps itself neatly during the process and does not get caught in any moving parts.

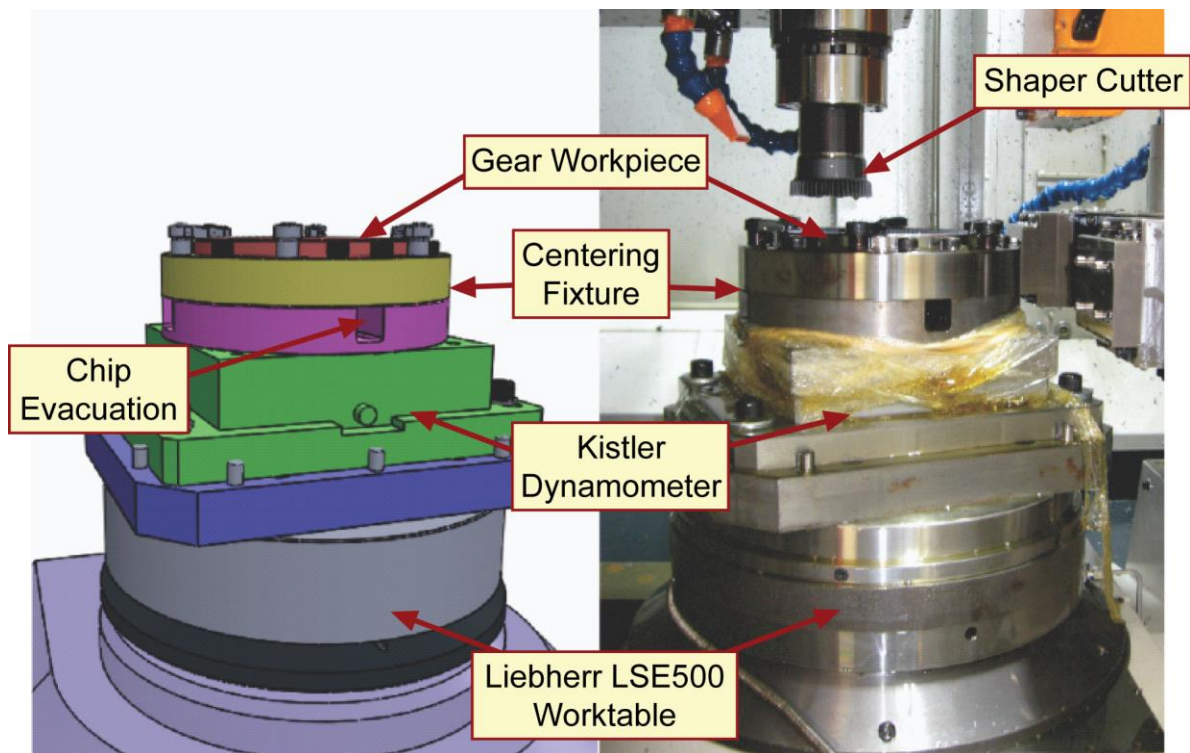


**Figure 4.20:** Experimental setup for spur internal gear case.

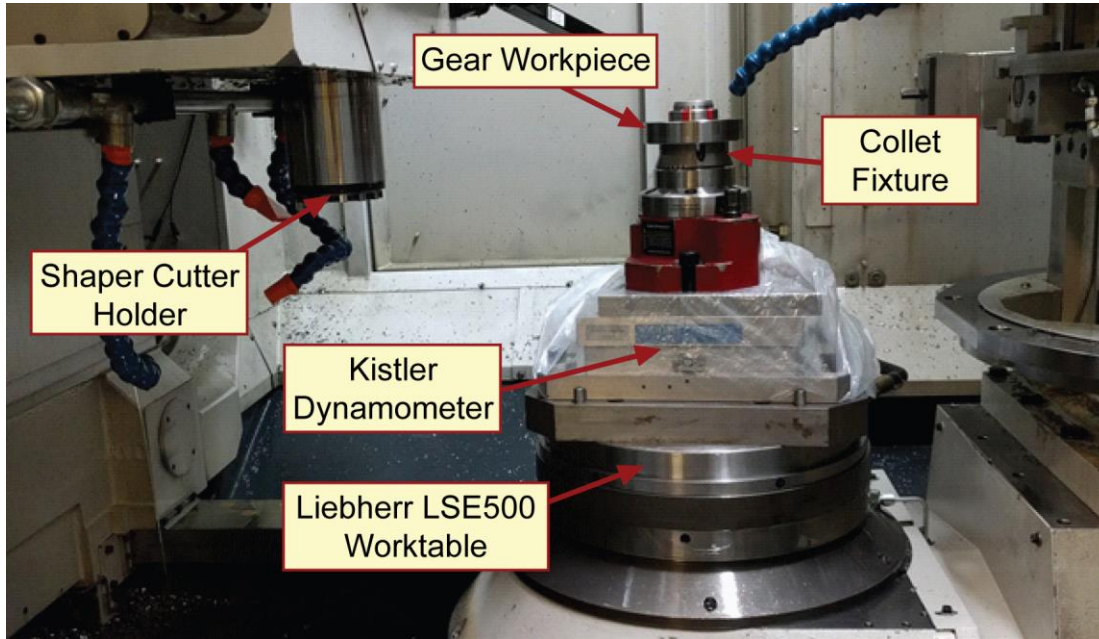


**Figure 4.21:** Experimental setup for external gear cases.

#### 4.6.2 Cutting Coefficient Determination

To calibrate the cutting force coefficients used in the simulation, in-process force measurements are used from the case studies. Two different procedures have been developed to identify coefficients for an orthogonal to oblique model and an orthogonal exponential chip thickness model. It is expected that if the tool has a large rake angle and thus a large variation of inclination along the cutting edge, than the orthogonal to oblique model would perform better than the exponential chip thickness model. However, for the performed experiments, it was found that the exponential chip thickness model performed better (particularly during finishing passes) since the chip thickness varies considerably during the gear shaping process.

##### 4.6.2.1 Orthogonal to Oblique Model

The orthogonal to oblique model consists of six parameters: the shear stress ( $\tau$ ), shear angle ( $\phi$ ), friction angle ( $\beta$ ), and edge coefficients ( $K_{te}$ ,  $K_{fe}$ ,  $K_{re}$ ). During simulation, the oblique cutting coefficients ( $K_{tc}$ ,  $K_{fc}$ ,  $K_{rc}$ ) are determined using the orthogonal to oblique transformations (equations (4.7) - (4.9)) which are a function of the shear stress, shear angle, friction angle, local rake angle, and local inclination angle. To predict the shear stress, shear angle, and friction angle from experimental data, a cubic search space is first

defined as depicted in Figure 4.22. From the cubic search space, many candidate points are chosen and the orthogonal to oblique transformation is used to determine the cutting coefficients based on the average local inclination and rake angle of the cutter. Then, based on experimentally measured forces and simulated chip characteristics, a least squares problem is formulated for each candidate point that solves for the edge coefficients using linear regression. Afterwards, the error for each candidate point is evaluated and the candidate set of coefficients with the least error is chosen.

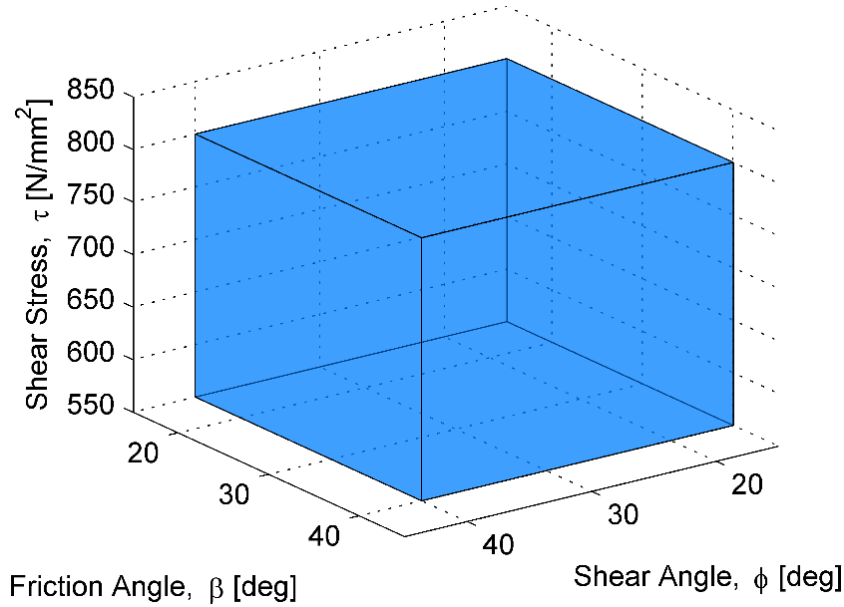


**Figure 4.22:** Cubic search for shear stress, friction angle, shear angle.

The least squares problem is formulated as follows where one data point is taken from each stroke during a process:

$$\underbrace{\begin{bmatrix} F_x \\ F_y \\ F_z \\ \vdots \\ F_x \\ F_y \\ F_z \end{bmatrix}}_{\text{measured forces}} = \underbrace{\begin{bmatrix} \sum_{\text{engaged nodes}} a\hat{t} & \sum_{\text{engaged nodes}} a\hat{f} & \sum_{\text{engaged nodes}} a\hat{r} & \sum_{\text{engaged nodes}} b\hat{t} & \sum_{\text{engaged nodes}} b\hat{f} & \sum_{\text{engaged nodes}} b\hat{r} \\ \vdots \\ \sum_{\text{engaged nodes}} a\hat{t} & \sum_{\text{engaged nodes}} a\hat{f} & \sum_{\text{engaged nodes}} a\hat{r} & \sum_{\text{engaged nodes}} b\hat{t} & \sum_{\text{engaged nodes}} b\hat{f} & \sum_{\text{engaged nodes}} b\hat{r} \end{bmatrix}}_{\text{regressors (from simulation)}} \underbrace{\begin{bmatrix} K_{tc} \\ K_{fc} \\ K_{rc} \\ K_{te} \\ K_{fe} \\ K_{re} \end{bmatrix}}_{\text{cutting coefficients}} \quad (4.55)$$

Above,  $s$  is the stroke number,  $S$  is the total number of strokes in the process,  $\hat{t}$ ,  $\hat{f}$ ,  $\hat{r}$  are the tangential, feed, and radial unit vectors for each engaged tool node,  $a$  is the chip area determined by the alpha shape



reconstruction for each engaged node, and  $b$  is the chip width for each engaged node. This can be simplified to the following form:

$$Y = [\phi_c \quad \phi_e] \begin{bmatrix} \theta_c \\ \theta_e \end{bmatrix} \quad (4.56)$$

Here,  $Y$  is the vector of measured forces with size  $3S \times 1$ ,  $\phi_c$  is the matrix of regressors pertaining to the cutting coefficients with size  $3S \times 3$ ,  $\phi_e$  is the matrix of regressors pertaining to the edge coefficients with size  $3S \times 3$ ,  $\theta_c = [K_{tc} \quad K_{fc} \quad K_{rc}]^T$  is the vector of cutting coefficients, and  $\theta_e = [K_{te} \quad K_{fe} \quad K_{re}]^T$  is the vector of edge coefficients. As mentioned, the cutting coefficients are determined using the orthogonal to oblique transformation from the candidate point within the cubic search space of shear stress, shear angle, and friction angle. Subsequently, the edge coefficients are determined using linear regression:

$$\theta_e = \text{pinv}\{\phi_e\} (Y - \phi_c \theta_c) \quad (4.57)$$

Here, since the influence of the radial edge coefficient is typically assumed to be negligible ( $K_{re} \cong 0$ ), the 3<sup>rd</sup> column of  $\phi_e$  is set to zero. The model prediction error for each candidate set of coefficients is evaluated using the RMS error of normalized forces:

$$\text{Error} = \sqrt{\frac{1}{3S} \left( \sum_{s=1}^S (e_x^2 + e_y^2 + e_z^2) \right)} \quad (4.58)$$

$$e_x = \frac{F_{x, \text{measured}} - F_{x, \text{simulated}}}{F_{x, \text{max}}}, \quad e_y = \frac{F_{y, \text{meas}} - F_{y, \text{sim}}}{F_{y, \text{max}}}, \quad e_z = \frac{F_{z, \text{meas}} - F_{z, \text{sim}}}{F_{z, \text{max}}} \quad (4.59)$$

The identified best set of coefficients for each material is given in Table 4.4. The AISI 1141 and 5130 steel cutting coefficients were determined from the internal spur gear one-pass process, and the AISI 8620 steel coefficients were determined from the external spur gear one-pass process. Contour plots that show how the error changes based on the shear angle and friction angle for the identified shear stress can be seen in Figure 4.23, Figure 4.24, and Figure 4.25.

**Table 4.4:** Identified orthogonal to oblique coefficients.

Material	$\tau$ [N/mm <sup>2</sup> ]	$\phi$ [deg]	$\beta$ [deg]	$K_{te}$ [N/mm]	$K_{fe}$ [N/mm]
AISI 1141 Steel	805.6	26.4	28.6	10.5	15.2
AISI 5130 Steel	764.1	27.7	36.7	18.9	10.2
AISI 8620 Steel	633.3	25.9	38.0	31.4	1.26

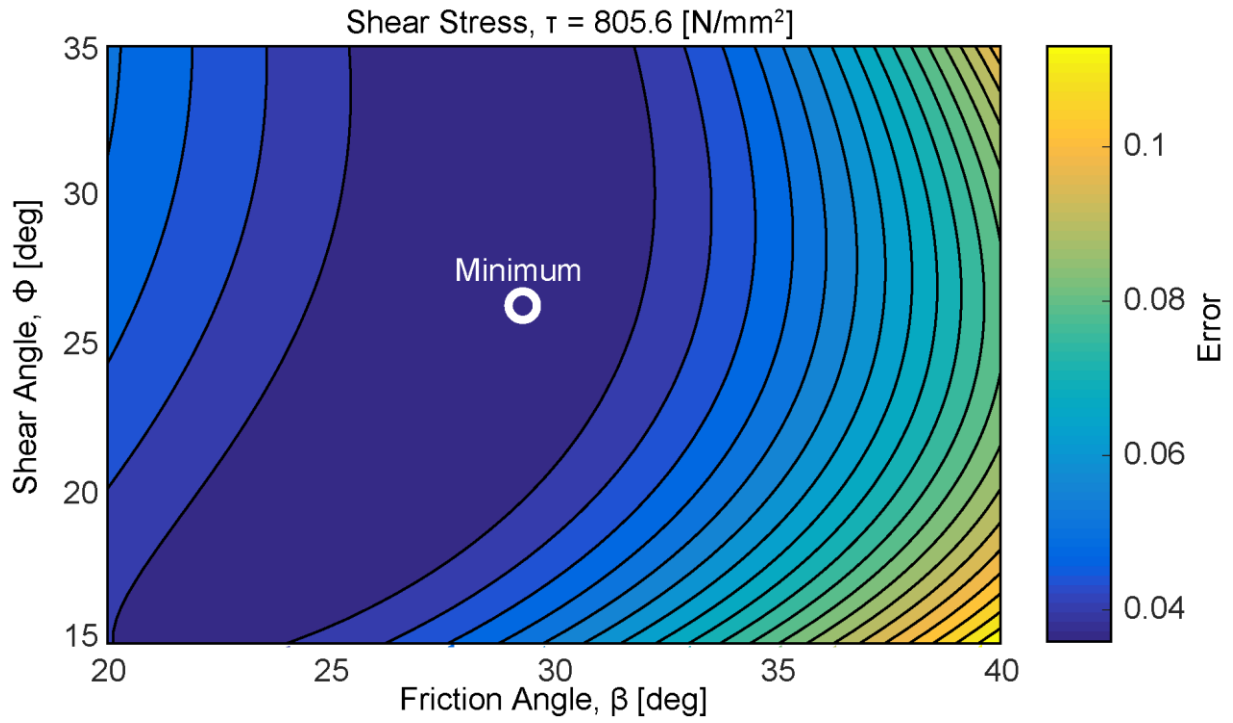


**Figure 4.23:** Error contour plot for AISI 1141 steel at  $\tau = 805.6$  [N/mm<sup>2</sup>].

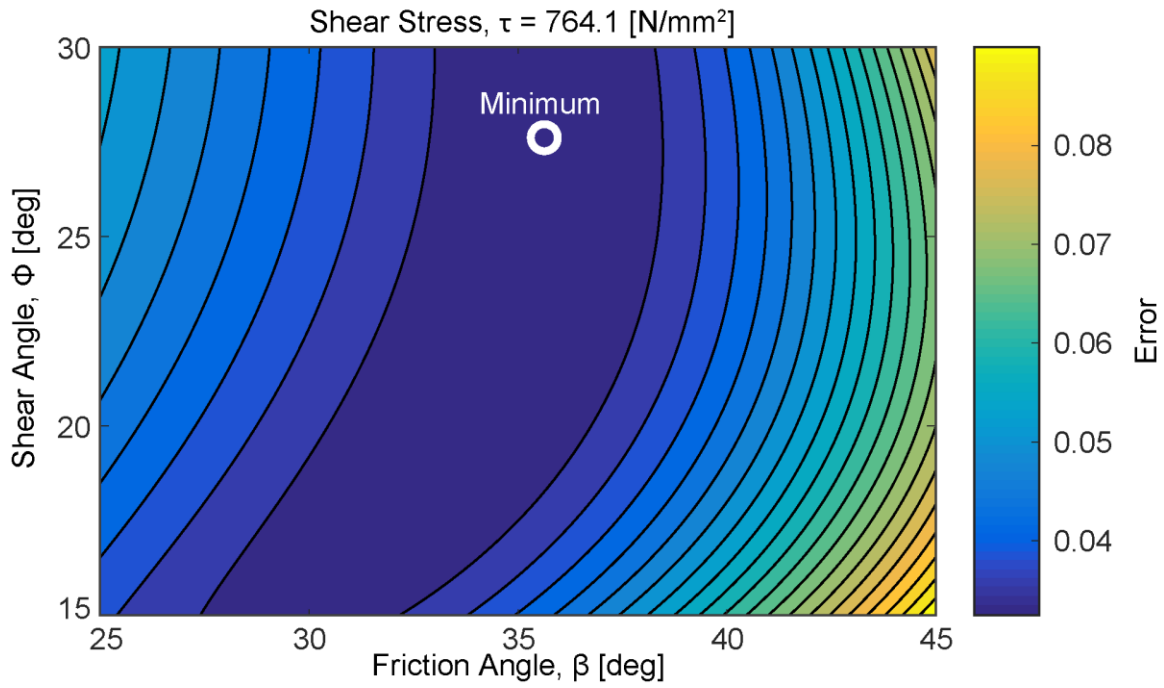


**Figure 4.24:** Error contour plot for AISI 5130 steel at  $\tau = 764.1$  [N/mm<sup>2</sup>].

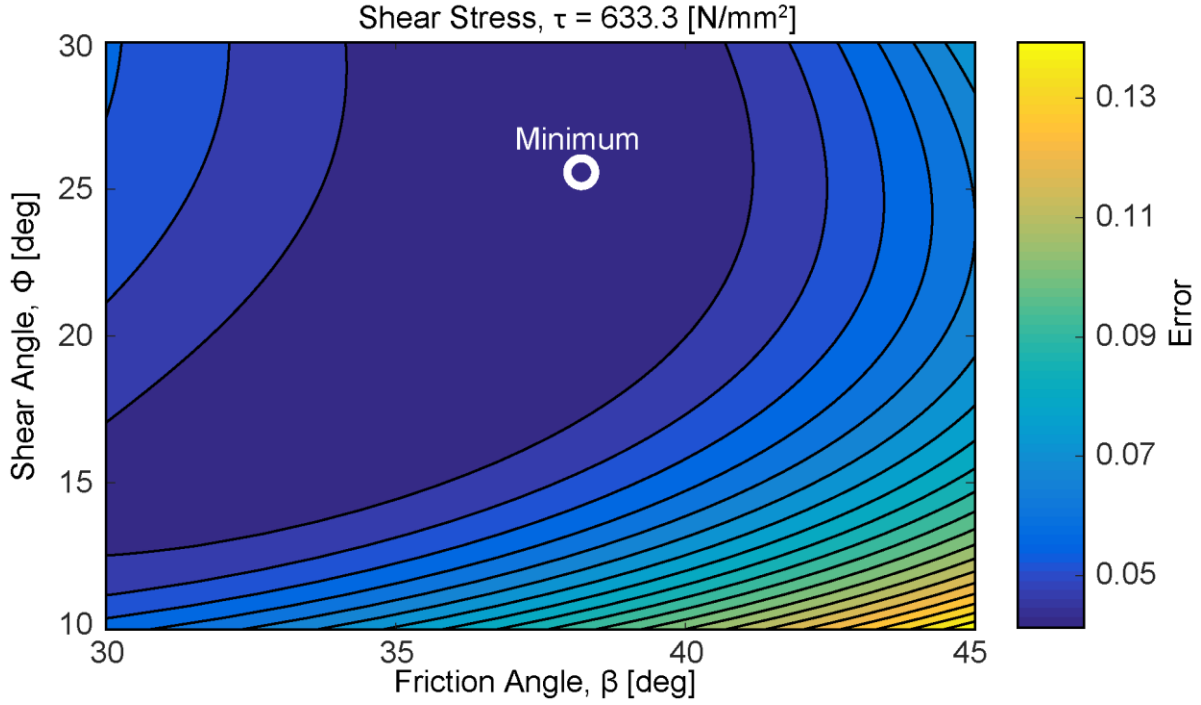


**Figure 4.25:** Error contour plot for AISI 8620 steel at  $\tau = 633.3$  [N/mm<sup>2</sup>].

#### 4.6.2.2 Orthogonal Exponential Chip Thickness Model

An orthogonal exponential chip thickness model is also fit based on in-process force measurements. In spur gear shaping, the measured cutting force can be separated into tangential and feed components. Given that the cutting velocity is solely in the  $z$  direction, the measured force in the  $z$  direction can be attributed to the tangential force, and the resultant force on the  $xy$  plane can be attributed to the feed component. The radial component would also contribute to force on the  $xy$  plane, but here it is assumed to be negligible ( $K_{rc} = 0$ ) since the inclination angle of the tools are  $5^\circ$  or less. Additionally, all edge components are assumed to be zero ( $K_{te} = K_{fe} = K_{re} = 0$ ). Accordingly, based on the effective simulated chip area, the tangential and feed coefficients can be determined for each data point:

$$K_{tc} = \frac{|F_{z, \text{measured}}|}{\underbrace{\sum_{\text{engaged nodes}} a\hat{t} \cdot \hat{Z}}_{\text{effective tangential chip area on } z \text{ axis}}}, K_{fc} = \frac{\sqrt{F_{x, \text{measured}}^2 + F_{y, \text{measured}}^2}}{\sqrt{\left(\underbrace{\sum_{\text{engaged nodes}} a\hat{f} \cdot \hat{X}}_{\text{effective feed chip area on } xy \text{ plane}}\right)^2 + \left(\sum_{\text{engaged nodes}} a\hat{f} \cdot \hat{Y}\right)^2}} \quad (4.60)$$

Similar to the orthogonal to oblique model, one measured data point is taken from each cutting stroke during the gear shaping process. Then, by comparing each measured  $K_{tc}$  and  $K_{fc}$  to the average simulated chip thickness for the data point, an exponential function can be fit to the data as seen in Figure 4.26, Figure 4.27, and Figure 4.28. Since chip mechanics typically only act exponentially with small chip thicknesses, a linear portion is defined where if the chip thickness is larger than the threshold, then the cutting coefficient is constant. Table 4.5 shows the identified coefficients for the three materials used in the experiments. The internal spur gear one-pass process was used for the AISI 1141 and 5130 steels, while the external spur gear two-pass process was used for the AISI 8620 steel as it was found that the one-pass process did not have enough data points with small chip thickness.

**Table 4.5:** Identified orthogonal exponential chip thickness coefficients.

<b>Material</b>	<b><math>K_{tc}</math> [N/mm<sup>2</sup>]</b>		<b><math>K_{fc}</math> [N/mm<sup>2</sup>]</b>	
AISI 1141 Steel	$35.15 h^{-0.9613}$	$h < 0.01$	$11.57 h^{-1.059}$	$h < 0.01$
	2941	$h \geq 0.01$	1518	$h \geq 0.01$
AISI 5130 Steel	$6.859 h^{-1.346}$	$h < 0.01$	$4.067 h^{-1.341}$	$h < 0.01$
	3375	$h \geq 0.01$	1956	$h \geq 0.01$
AISI 8620 Steel	$37.25 h^{-1.045}$	$h < 0.015$	$14.41 h^{-1.14}$	$h < 0.015$
	3000	$h \geq 0.015$	1730	$h \geq 0.015$

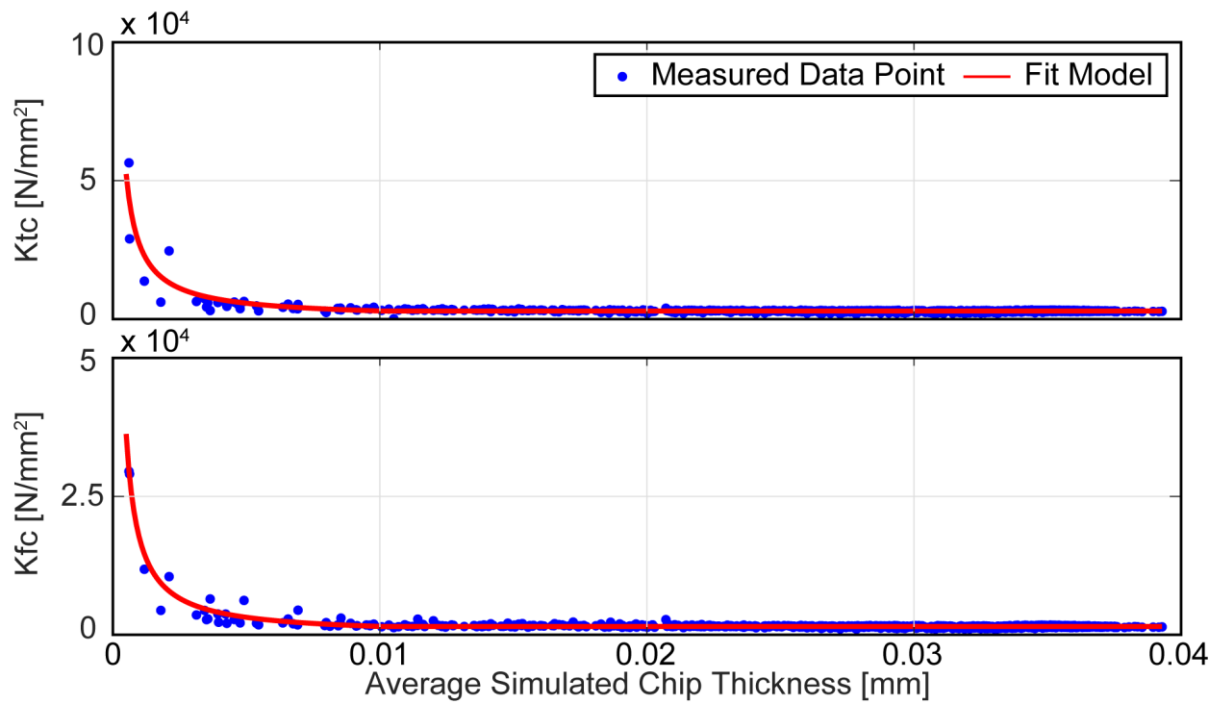


**Figure 4.26:** Exponential chip model for AISI 1141 steel.

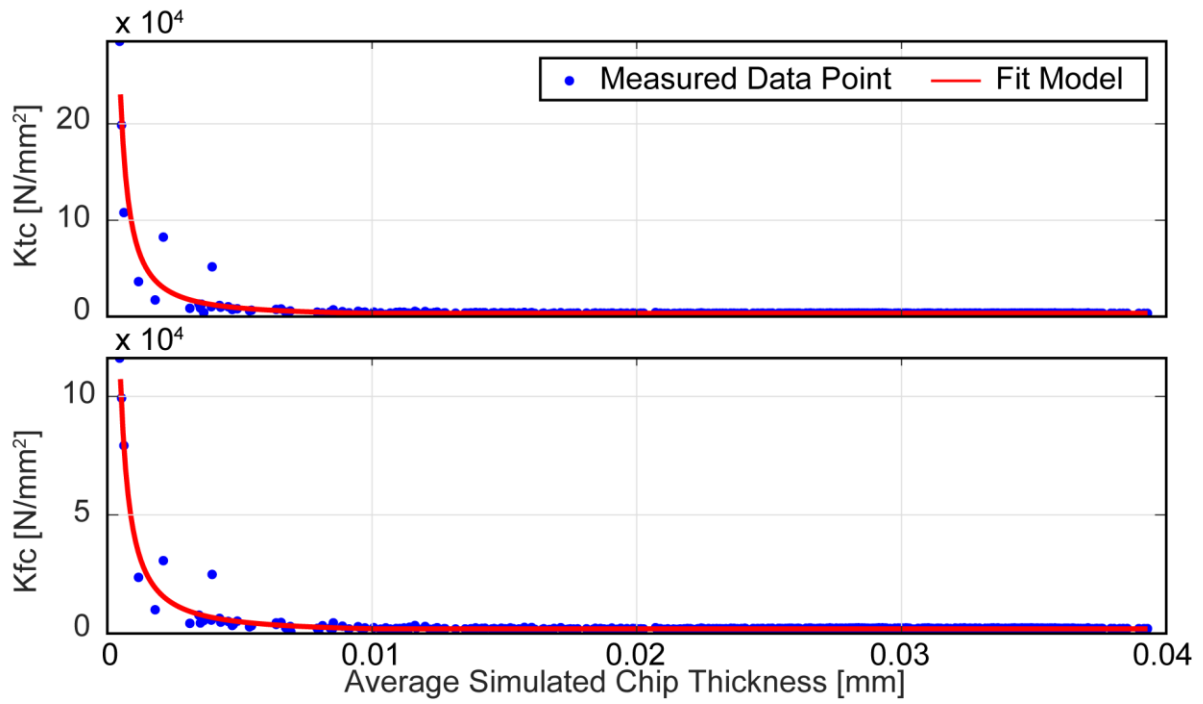


**Figure 4.27:** Exponential chip model for AISI 5130 steel.

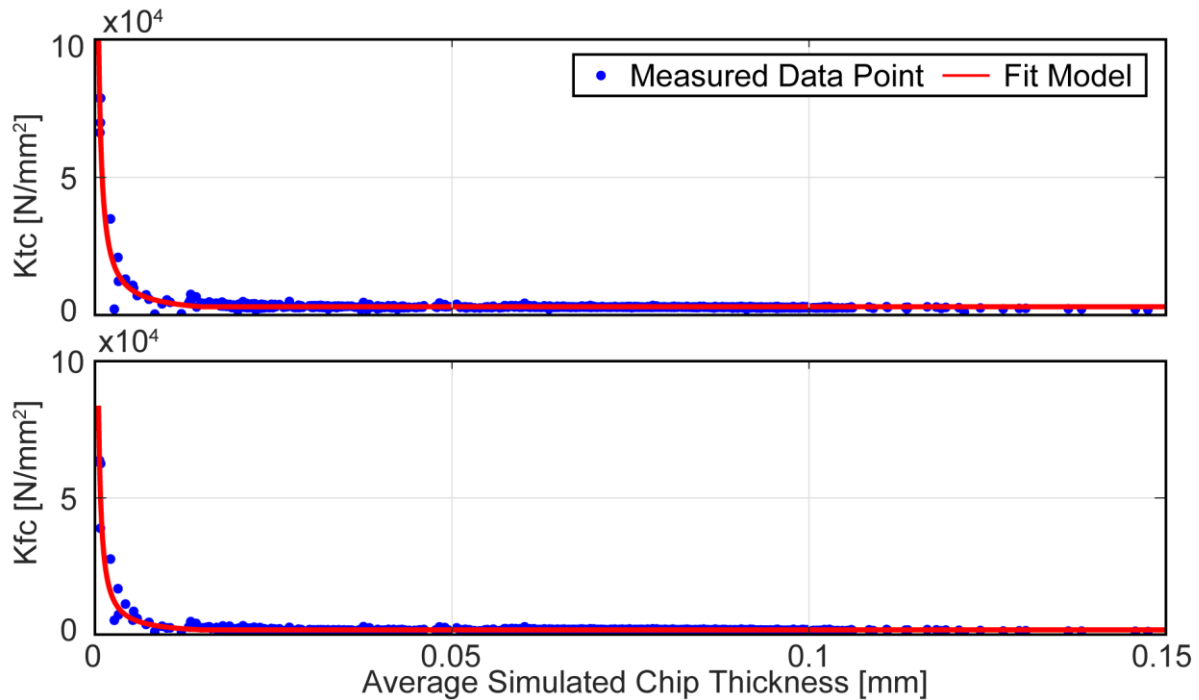


**Figure 4.28:** Exponential chip model for AISI 8620 steel.

### 4.6.3 Results

The following sections show comparisons of simulated and measured cutting forces in each of the case studies. In each case, the identified orthogonal exponential chip thickness model was used. Although both models give accurate force predictions, the exponential chip thickness model produced more accurate predictions particularly in finishing passes as the chip thicknesses are thin.

#### 4.6.3.1 Internal Spur Gear, One-Pass, AISI 1141 Steel

Figure 4.29 shows a comparison of the simulated and measured cutting forces the internal gear, one-pass process with AISI 1141 steel workpiece. Several trends can be seen in the forces profiles. During the radial infeed of the tool, the cutting forces slowly increase until the peak force is seen at the end of the infeed where there is a combination of the radial feed and rotary feed which results in the maximum chip area. After the infeed is complete, the forces remain relatively steady as each of the teeth are cut into the workpiece. Of course, the magnitude in the  $x$  and  $y$  directions are changing sinusoidally as the dynamometer is rotating with the gear. Throughout the entire cutting pass, a slight wavy pattern can be observed as seen in the zoomed in profiles in Figure 4.30. This is due to the repetitive teeth engagement

pattern of the gear shaping process. Each time a new tooth on the tool starts its engagement in the workpiece, a maximum chip area will soon occur after which results in a peak cutting force. After the steady-state cutting phase, the completion of the gear occurs which is when the tool comes back around to the area of the workpiece where the infeed first began. During this stage, the cutting forces slowly decrease until they become zero and the workpiece is complete.

The accuracy of the simulated cutting forces are evaluated by calculating the RMS error of the forces taking one data point from each stroke. Each data point is determined by calculating the average simulated and measured force over the cutting stroke. Table 4.6 shows the RMS error along with percentage error calculated based on the maximum force in each direction. The simulated and measured cutting forces show very good correlation throughout the entire process with an error less than 5%.

**Table 4.6:** RMS error for internal spur gear, one-pass, AISI 1141 steel process.

	$E_x$ [N]	$E_y$ [N]	$E_z$ [N]
Single Pass	45.7 (3.6%)	56.7 (4.6%)	135 (3.4%)

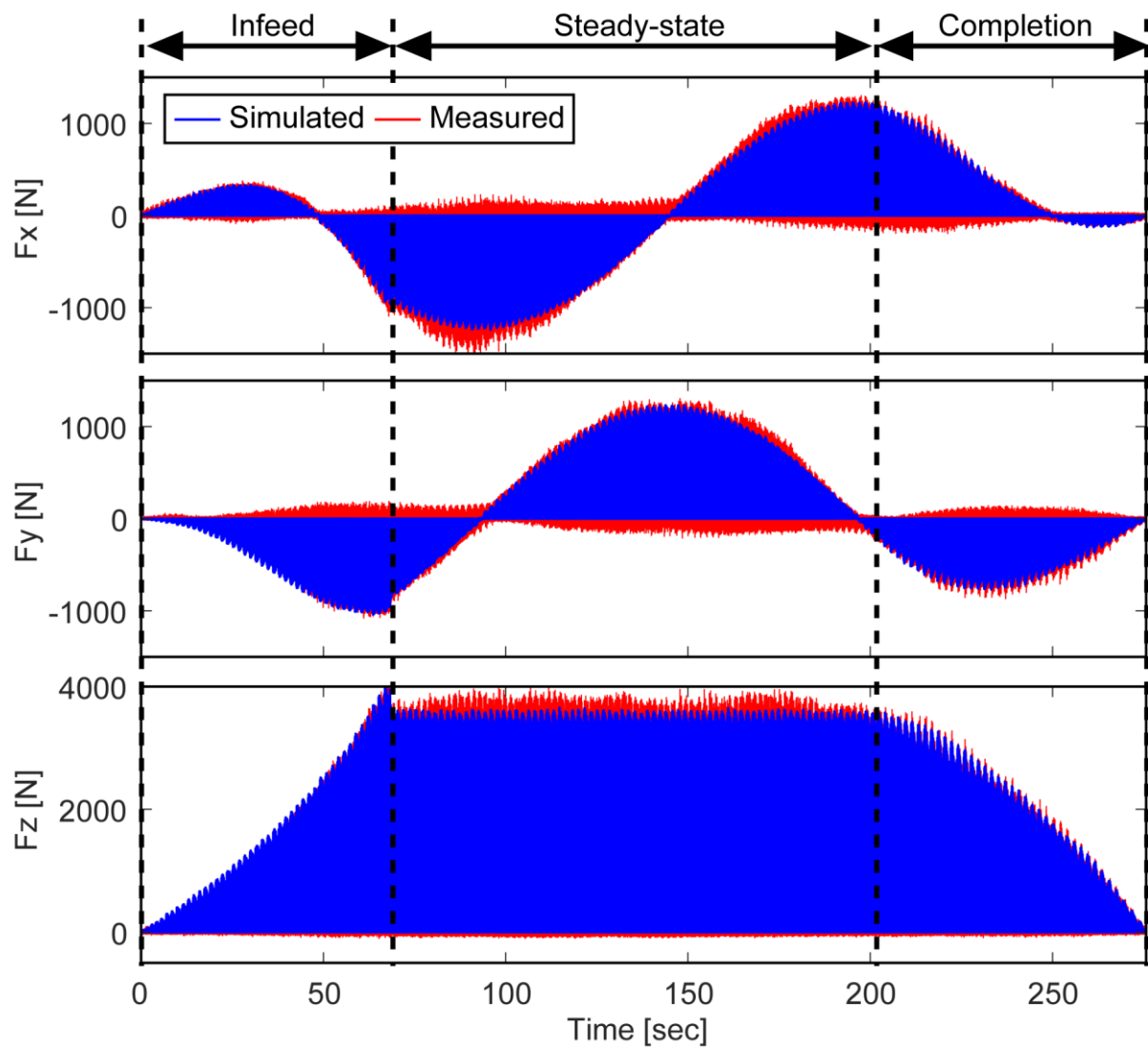


**Figure 4.29:** Comparison of simulated and measured cutting forces for internal spur gear, one-pass, AISI 1141 steel process.



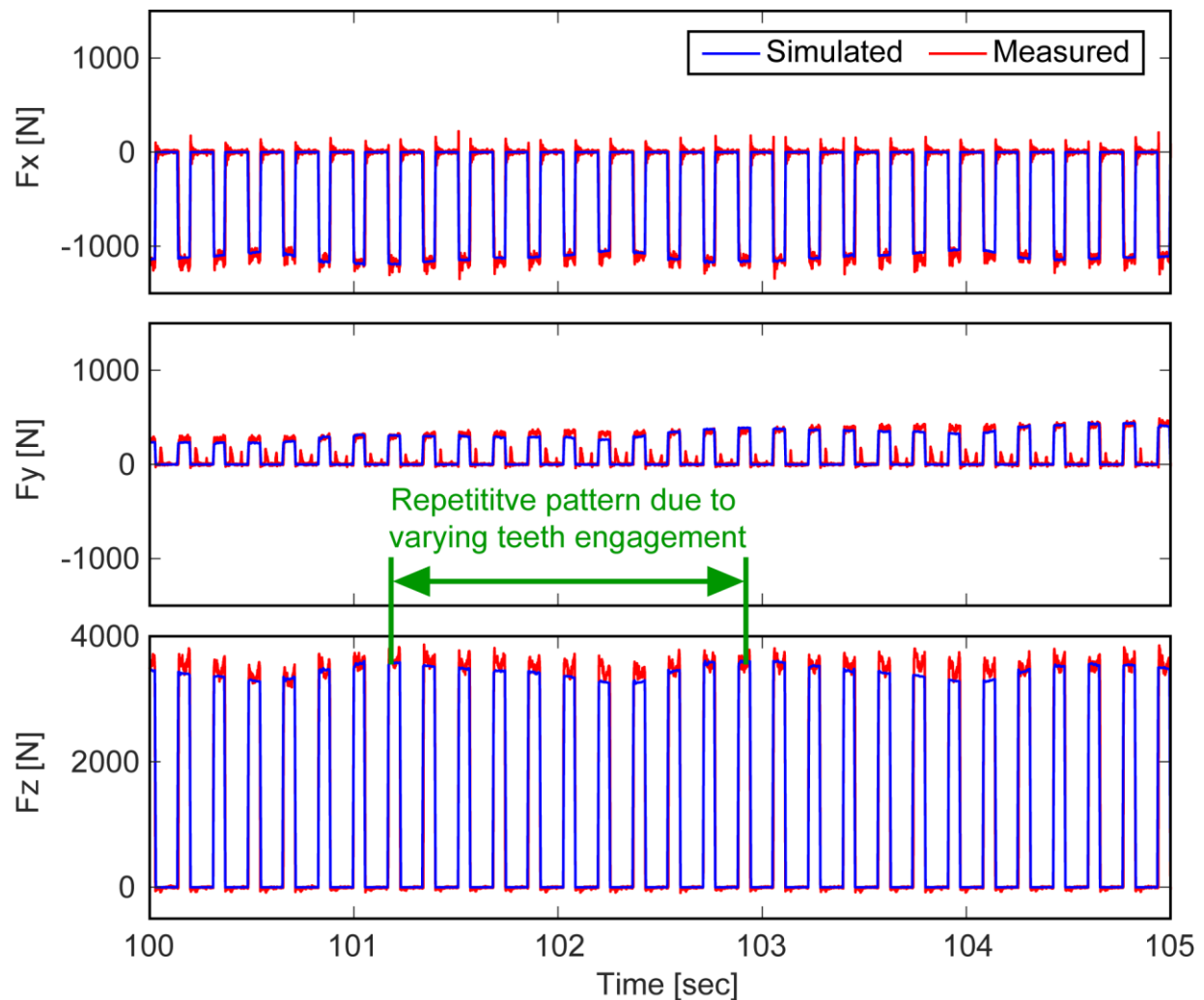


**Figure 4.30:** Comparison of simulated and measured cutting forces for internal spur gear, one-pass, AISI 1141 steel process, zoomed in.

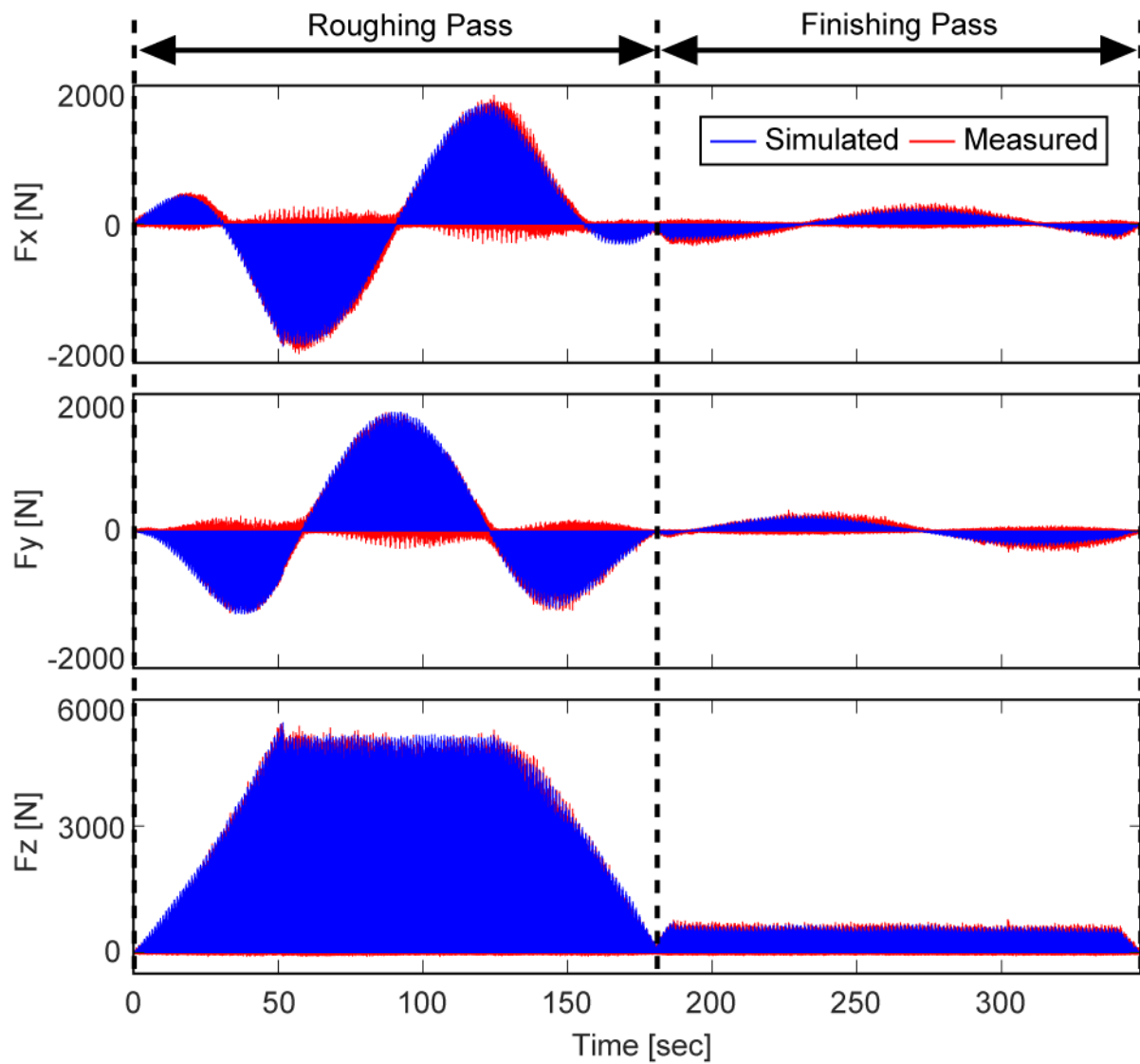
#### 4.6.3.2 Internal Spur Gear, Two-Pass, AISI 1141 Steel

Figure 4.31 shows the simulated and measured cutting forces profiles for the internal spur gear, two-pass, AISI 1141 steel process. Very similar trends can be seen as with the single pass process, however, there are two cycles of the infeed, steady-state, and completion phases. It can be seen in the zoomed profiles (Figure 4.32), that the wavy repetitive pattern in the finishing pass becomes out of phase contributing to error in the predicted force profiles. This is likely due to unknown kinematics in the transition between the two-passes. The kinematic model assumes instantaneous change between the rotary/radial feedrate of adjacent cutting passes, however this is not likely the case on the gear shaping machine. Nevertheless, the magnitudes of

the forces match well. In later experiments (external spur and external helical gear cases), commanded trajectories are captured from the CNC during the experiments and used directly in simulation which results in closer agreement for the second pass. Table 4.7 below shows the RMS error and percentage for the roughing and finishing passes.

**Table 4.7:** RMS error for internal spur gear, two-pass, AISI 1141 steel process.

	$E_x$ [N]	$E_y$ [N]	$E_z$ [N]
Roughing Pass	64.4 (3.7%)	96.2 (5.5%)	204 (3.8%)
Finishing Pass	22.1 (10.5%)	24.3 (11.3%)	74.5 (11.3%)



**Figure 4.31:** Comparison of simulated and measured cutting forces for internal spur gear, two-pass, AISI 1141 steel process.

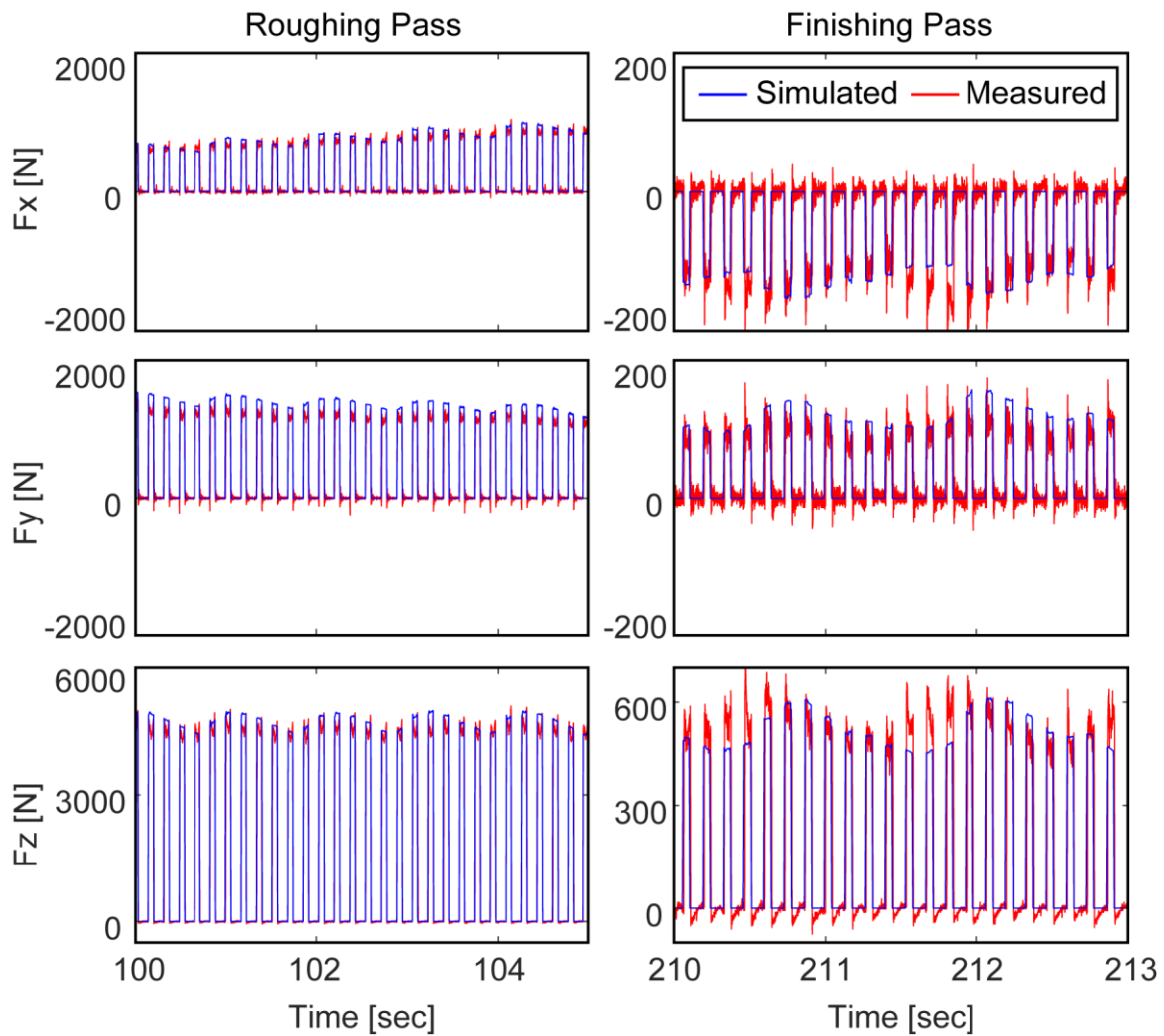


**Figure 4.32:** Comparison of simulated and measured cutting forces for internal spur gear, two-pass, AISI 1141 steel process, zoomed in.

#### 4.6.3.3 Internal Spur Gear, One-Pass, AISI 5130 Steel

Figure 4.33 and Figure 4.34 shows the simulated and measured cutting forces for the internal spur, one-pass process with the AISI 5130 steel workpiece. Table 4.8 shows the RMS error of the predicted forces. Very similar trends can be seen to the equivalent process with AISI 1141 steel workpiece.

**Table 4.8:** RMS error for internal spur gear, one-pass, AISI 5130 steel process.

	$E_x$ [N]	$E_y$ [N]	$E_z$ [N]
Single Pass	61.1 (3.7%)	68.5 (4.2%)	188 (4.0%)

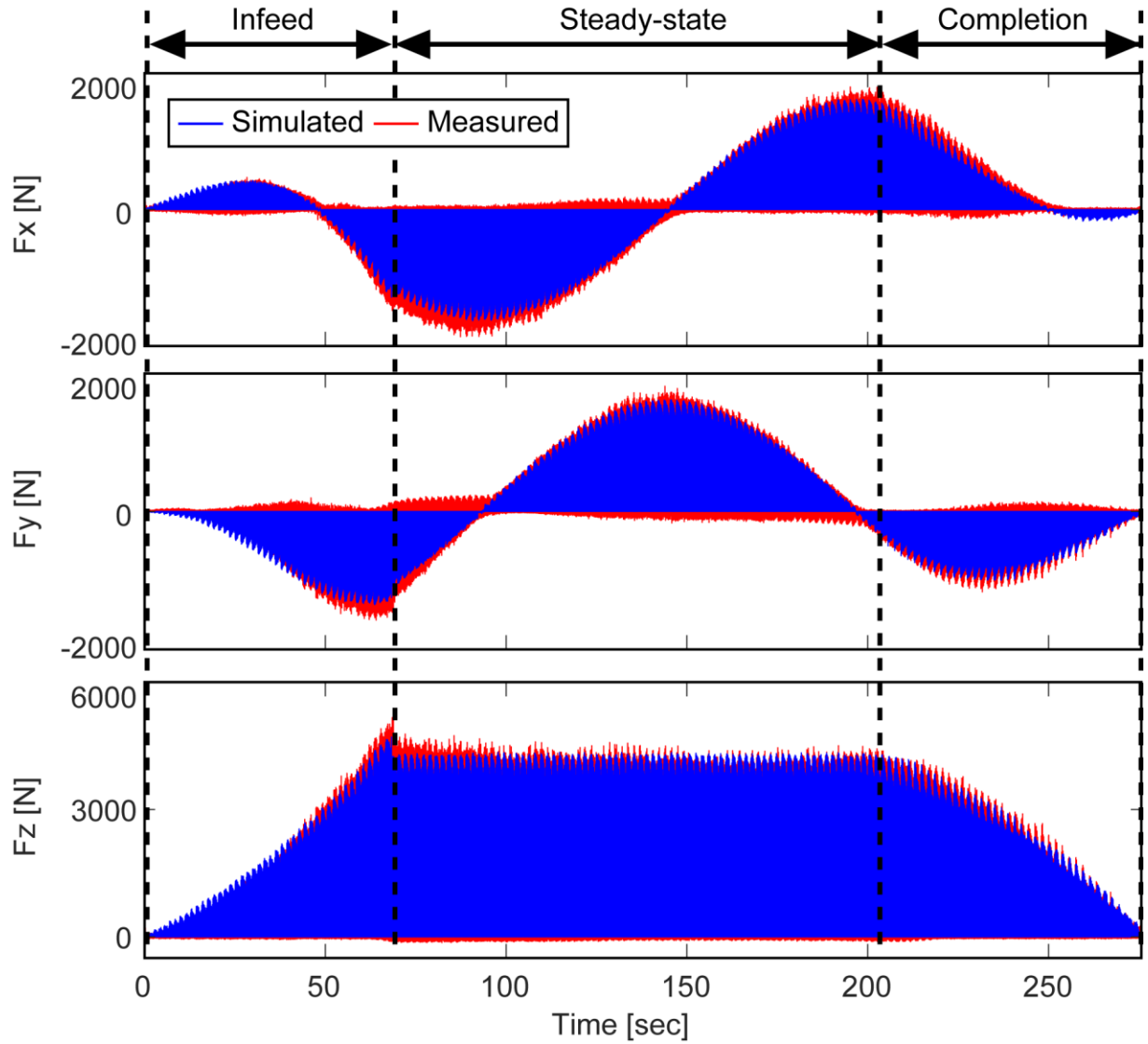


**Figure 4.33:** Comparison of simulated and measured cutting forces for internal spur gear, one-pass, AISI 5130 steel process.

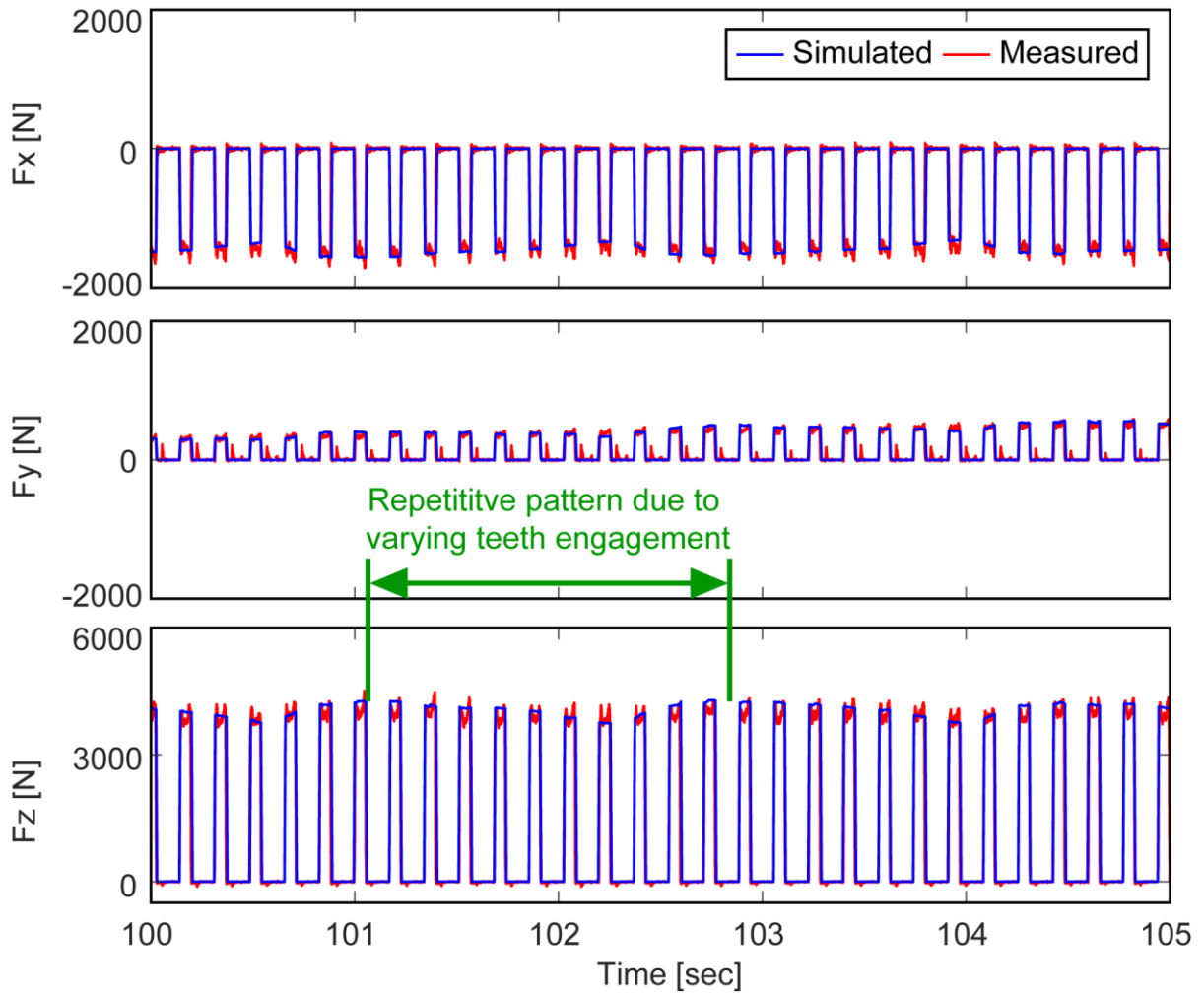


**Figure 4.34:** Comparison of simulated and measured cutting forces for internal spur gear, one-pass, AISI 5130 steel process, zoomed in.

#### 4.6.3.4 Internal Spur Gear, Two-Pass, AISI 5130 Steel

Figure 4.35 and Figure 4.36 shows the simulated and measured cutting force profiles for the internal spur, two-pass process with AISI 5130 steel workpiece material. The RMS of the error for the roughing and finishing passes are given in Table 4.9. Very similar trends can be seen as with the internal spur, two-pass process with 1141 steel.

**Table 4.9:** RMS error for internal spur gear, two-pass, AISI 5130 steel process.

	$E_x$ [N]	$E_y$ [N]	$E_z$ [N]
Roughing Pass	99.8 (4.4%)	109 (4.8%)	301 (4.8%)
Finishing Pass	42.9 (14.0%)	49.1 (15.7%)	149 (16.7%)

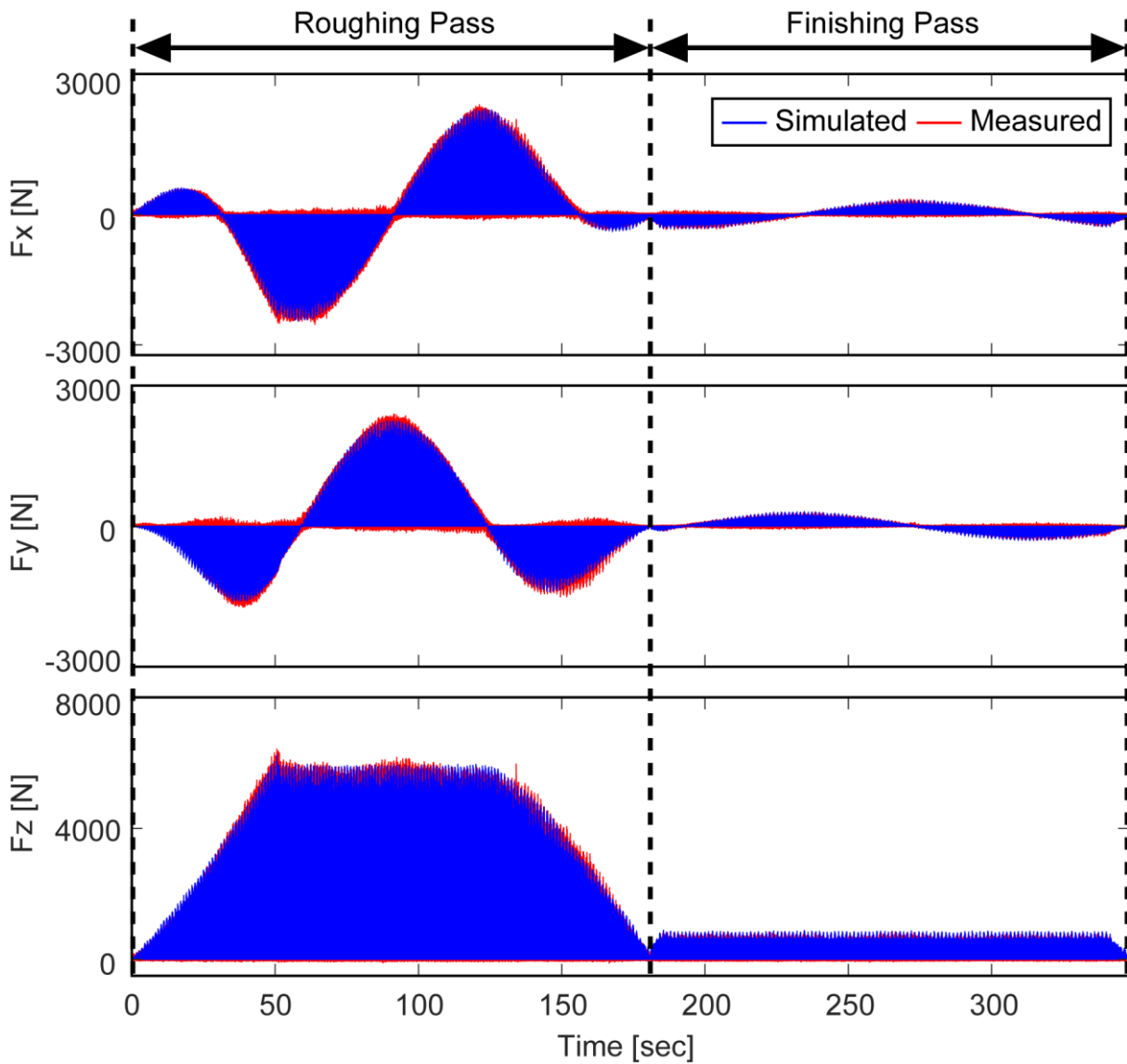


**Figure 4.35:** Comparison of simulated and measured cutting forces for internal spur gear, two-pass, AISI 5130 steel process.

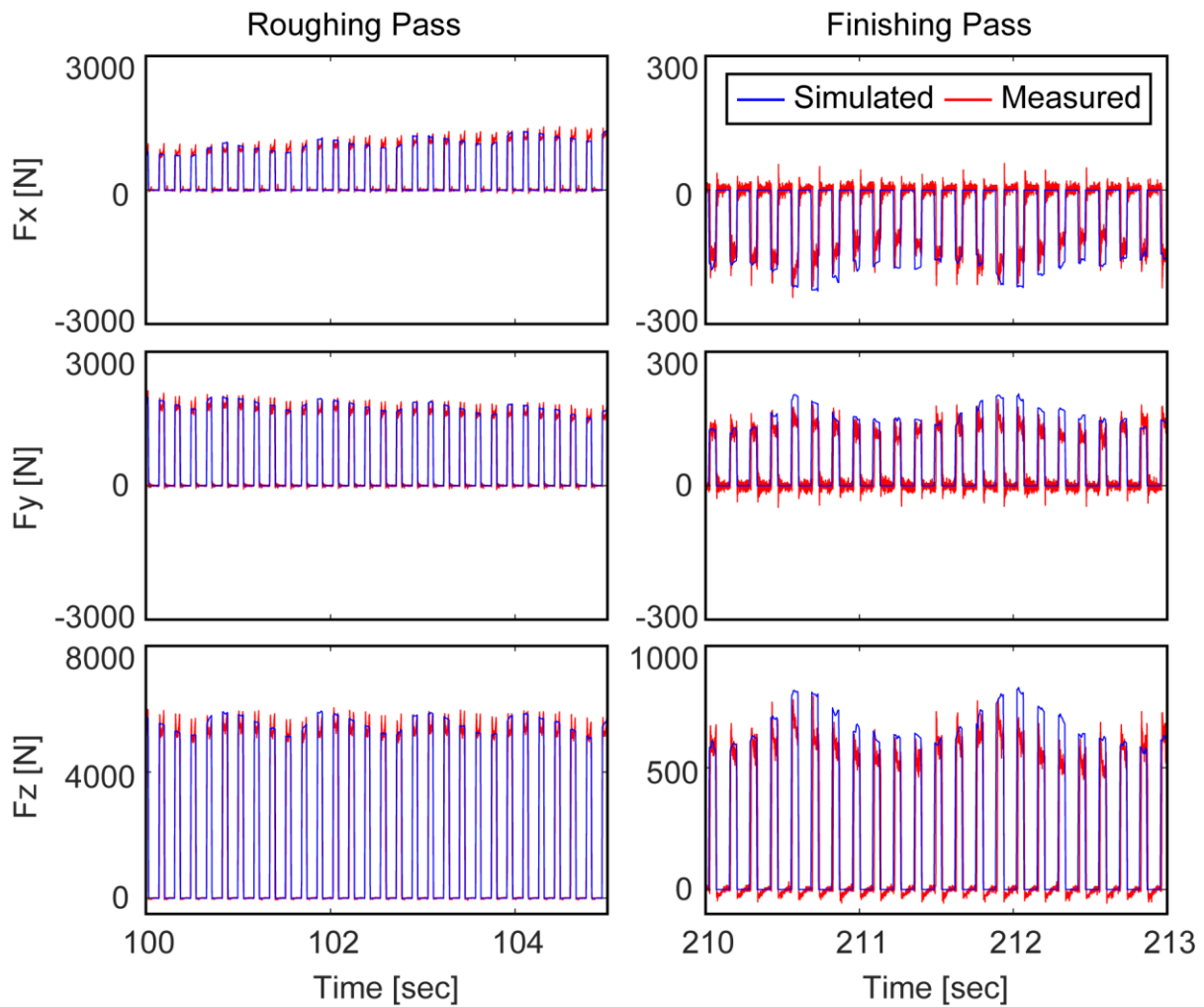


**Figure 4.36:** Comparison of simulated and measured cutting forces for internal spur gear, two-pass, AISI 5130 steel process, zoomed in.

#### 4.6.3.5 External Spur Gear, One-Pass, AISI 8620 Steel

Figure 4.37 shows the overall simulated and measured cutting forces for the external gear, one-pass process with AISI 8620 steel workpiece. Similar trends can be seen as with the internal case. The infeed, steady-state and completion phases can be seen, however the repetitive pattern due to the varying teeth engagement is much more pronounced in this case. This is due to the module being larger and the workpiece being an external gear which results in a smaller contact ratio. In this case, there are only 2-3 tool teeth in contact with the workpiece at once, whereas in the internal case there are 4-5 teeth in contact at once. This results in less uniform chip engagement throughout the process and, therefore, less uniform cutting forces. Figure



4.38 shows the zoomed in cutting force profiles and Table 4.10 gives the RMS error. As can be seen, the simulated and measured profiles correlate well, however there is more error compared to the internal spur one-pass process (5-6% compared to 3-4%). This can be seen particularly in the magnitude of the peak forces at the beginning of the repeating waves. It is hypothesized that this error may be caused by thermal effects; due to the cutting forces being large, the workpiece may be undergoing temperature increase which would change the cutting properties of the material. Further research is needed for confirmation of this hypothesis.

**Table 4.10:** RMS error for external spur gear, one-pass, AISI 8620 steel process.

	$E_x$ [N]	$E_y$ [N]	$E_z$ [N]
Single Pass	207 (6.1%)	210 (6.0%)	410 (4.8%)

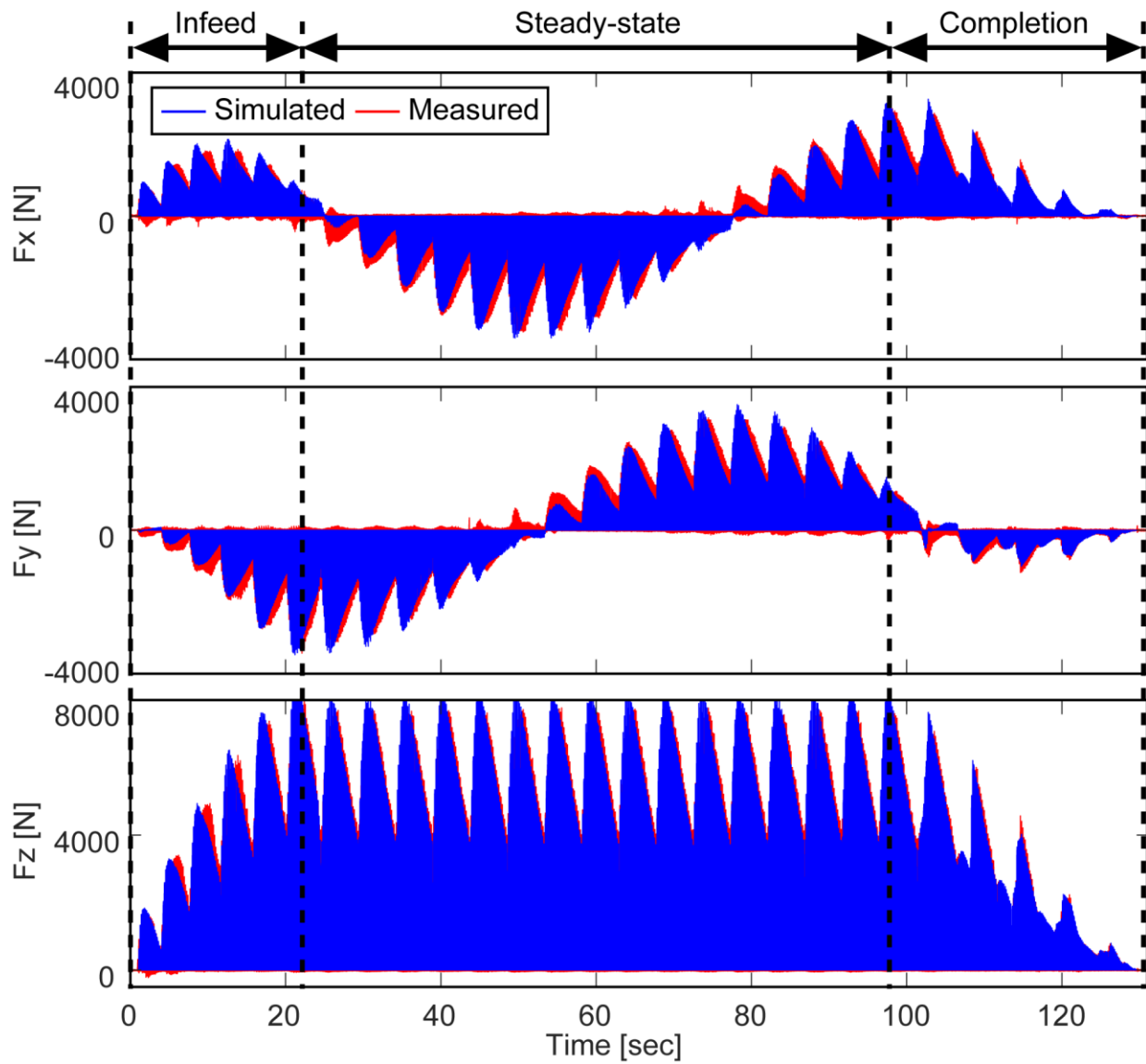


**Figure 4.37:** Comparison of simulated and measured cutting forces for external spur gear, one-pass, AISI 8620 steel process.

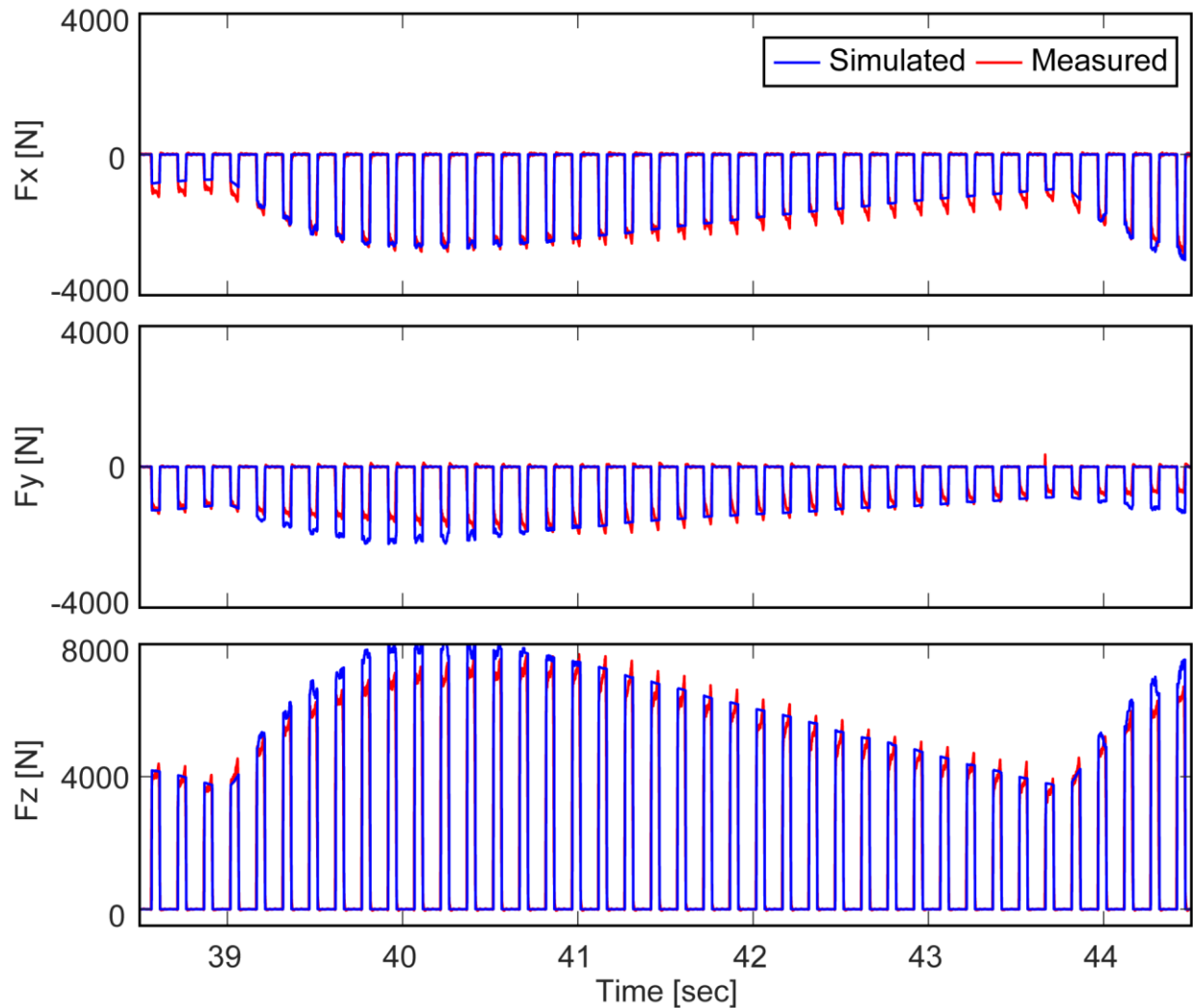


**Figure 4.38:** Comparison of simulated and measured cutting forces for external spur gear, one-pass, AISI 8620 steel process, zoomed in.

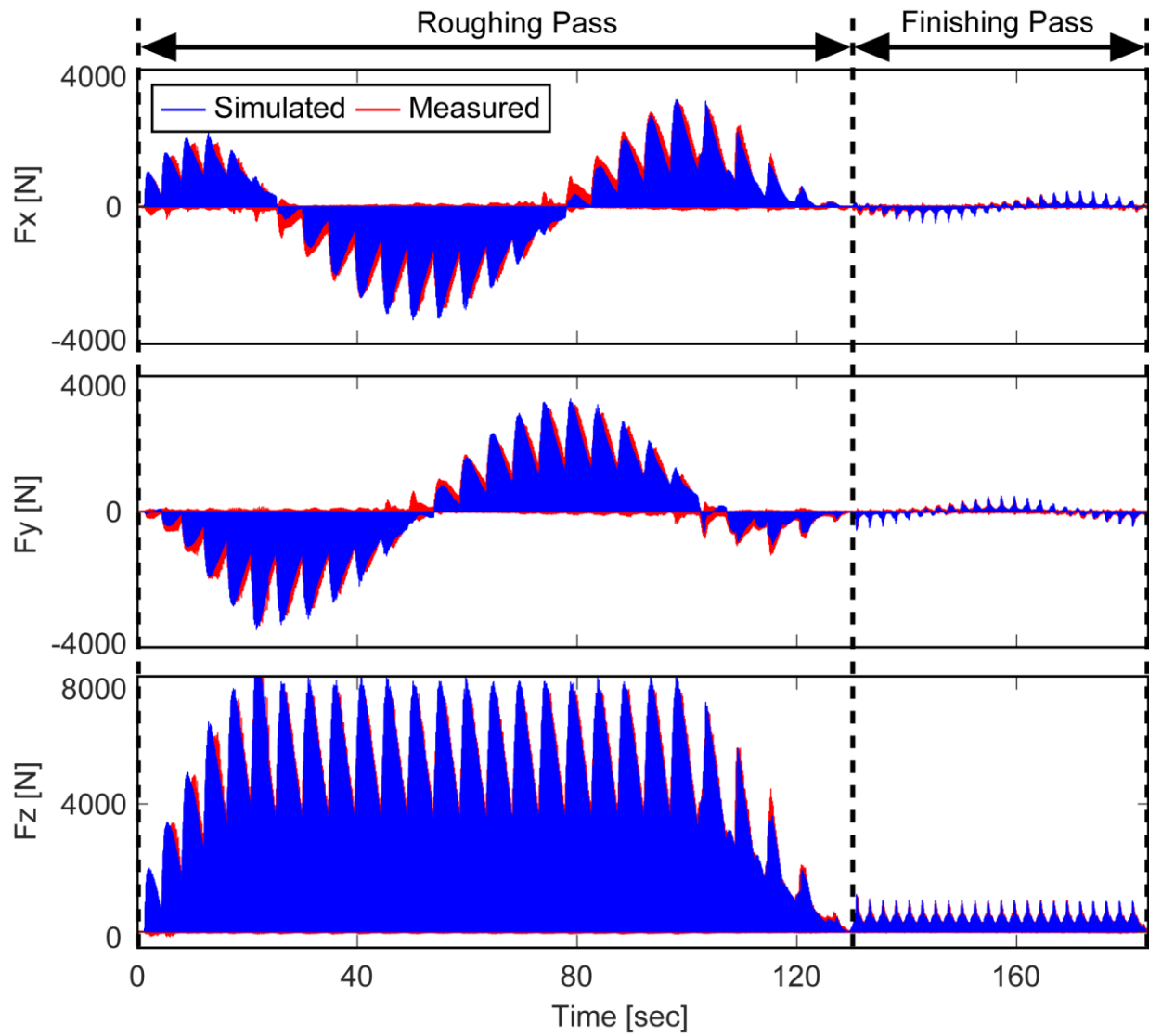
#### 4.6.3.6 External Spur Gear, Two-Pass, AISI 8620 Steel

Figure 4.39 and Figure 4.40 shows the simulated and measured cutting forces for the external gear, two-pass process. Similar trends can be seen in both of the passes as seen in the external single pass process. However, better correlation can be seen in the finishing pass in this case than the finishing pass of the internal gear two-pass processes. In this experiment (and all of the external gear case studies), commanded kinematic profiles from the servo controller of the shaping machine tool were captured and used directly as

the kinematic profiles in simulation. Because of this, the transition period before and after each pass is accurate and the repetitive patterns match well. Table 4.11 gives the RMS error for each of the passes.

**Table 4.11:** RMS error for external spur gear, two-pass, AISI 8620 steel process.

	$E_x$ [N]	$E_y$ [N]	$E_z$ [N]
Roughing Pass	202 (6.0%)	191 (5.5%)	420 (4.9%)
Finishing Pass	46.6 (9.8%)	44.0 (8.0%)	67.9 (5.8%)



**Figure 4.39:** Comparison of simulated and measured cutting forces for external spur gear, two-pass, AISI 8620 steel process.

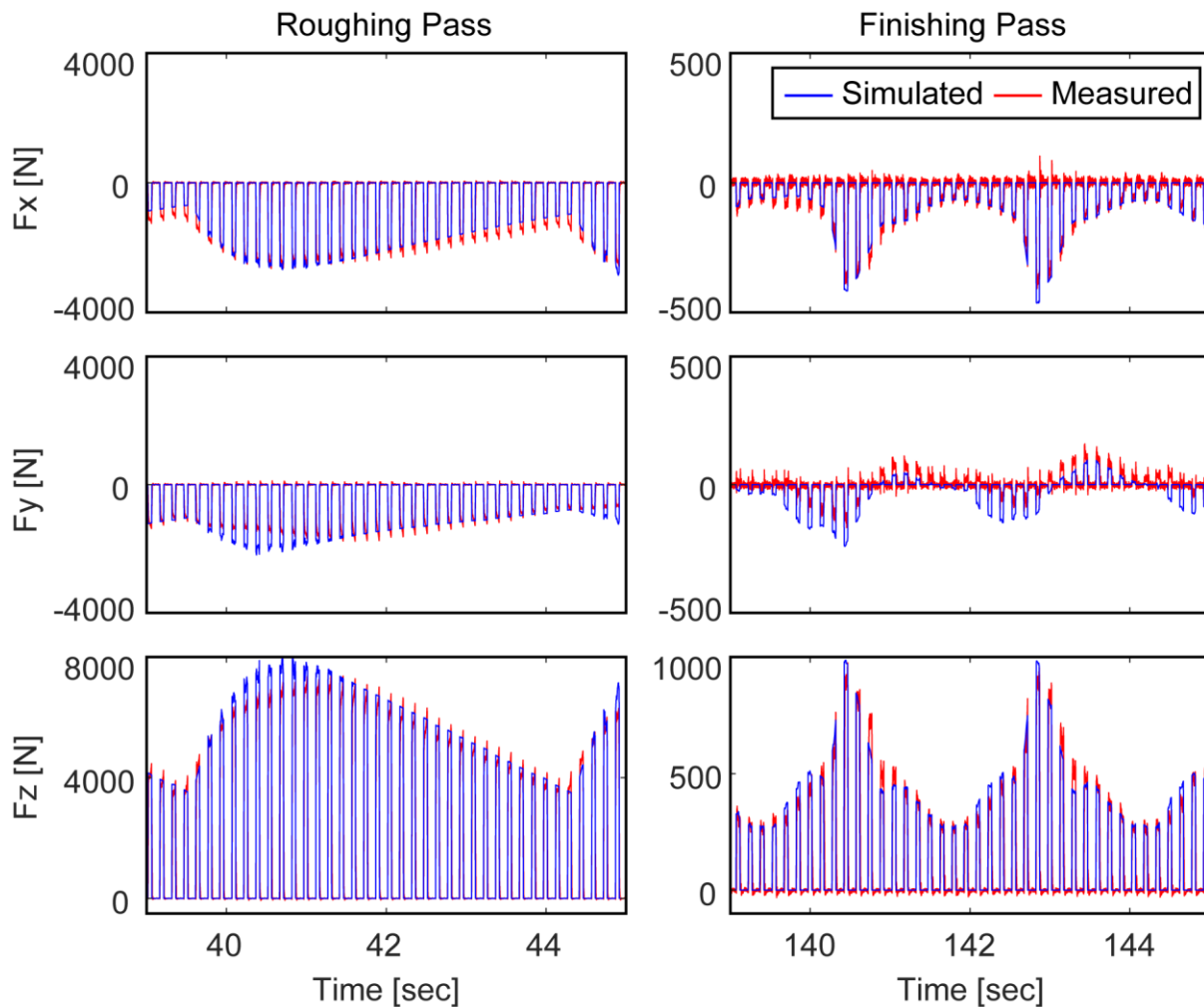


**Figure 4.40:** Comparison of simulated and measured cutting forces for external spur gear, two-pass, AISI 8620 steel process, zoomed in.

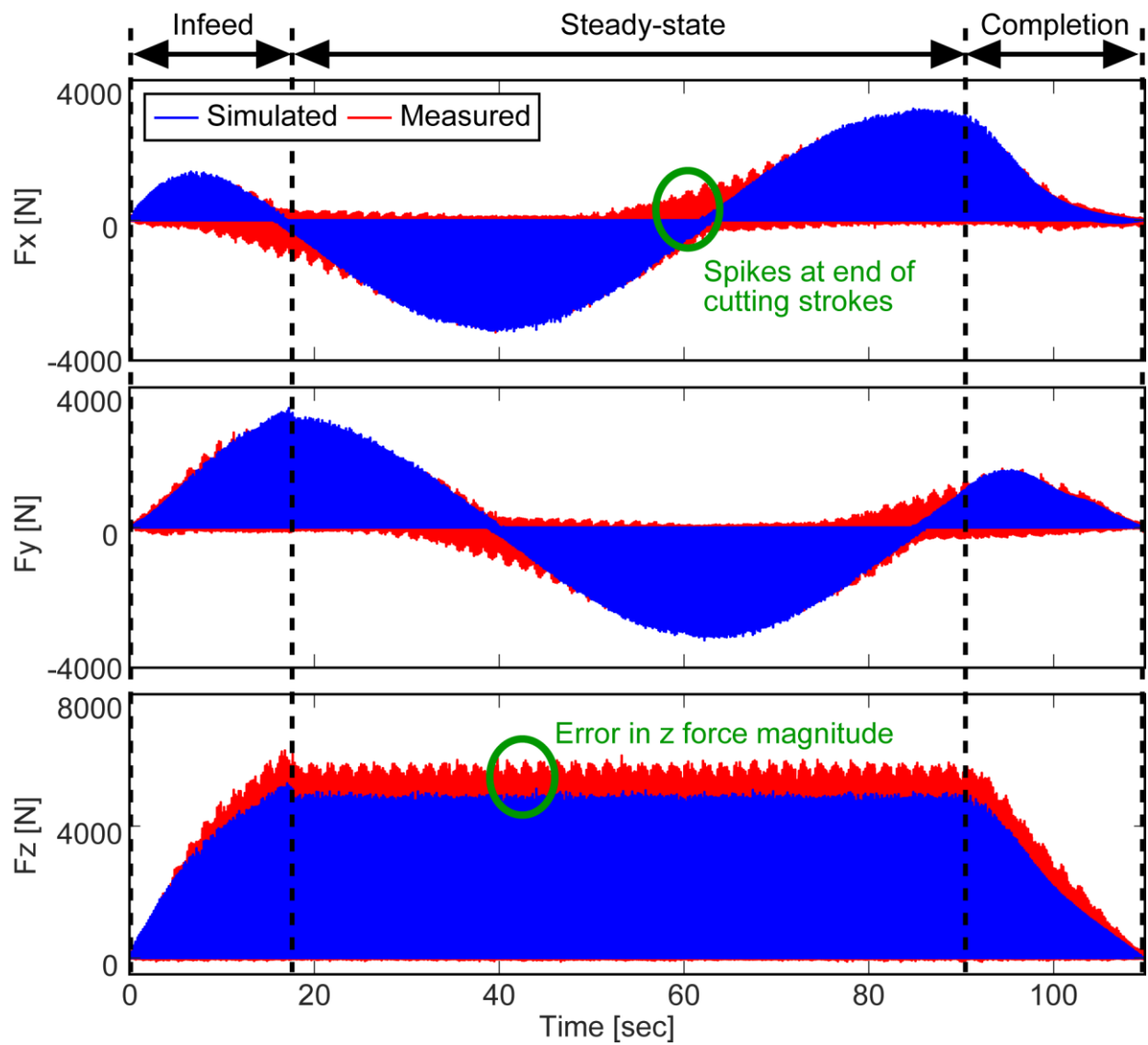
#### 4.6.3.7 External Helix Gear, One-Pass, AISI 8620 Steel

Figure 4.41 and Figure 4.42 shows the simulated and measured cutting force profiles for the external helical gear, one-pass process. In this case, the same cutting coefficients are used as with the external spur gear with AISI 8620 steel material. It can be seen that the overall trends of the profiles correlate well, however there is some noteworthy error in the magnitude of the  $z$  forces and there are sometimes spikes at the end of the cutting strokes in the  $x$  and  $y$  directions. It is hypothesized that a lot of this error is attributed due to rubbing / interference of the tool during cutting which is evident by gouges and scratches appearing in the finished workpiece (Figure 4.43). The interference would cause additional friction as the cutter moves down

the workpiece thus increasing the cutting force in the  $z$  direction. Once the cutter is finished the cutting stroke, than the built up pressure from the tool interference is released which may explain the measured cutting force spikes in the  $x$  and  $y$  directions. Other possible sources of error include visible tool wear on the helical gear shaper (see Figure 4.19) which can affect the cutting forces, and the cutting speed during the external helical gear cases is almost double that of the external spur gear cases due to larger cutting stroke length. Of course, the cutting force model for helical cutting may also be inaccurate; therefore more experiments are needed to investigate the cause of the discrepancy. For example, designing a helical cutting test where there is no resulting gouges or scratches on the workpiece would help differentiate whether the error is due to tool rubbing. Nevertheless, there is still good correlation between the measured and simulated cutting forces. Table 4.12 shows the RMS error and percentage for the process.

**Table 4.12:** RMS error for external helix gear, one-pass, AISI 8620 steel process.

	$E_x$ [N]	$E_y$ [N]	$E_z$ [N]
Single Pass	206 (6.5%)	210 (6.1%)	697 (13.2%)



**Figure 4.41:** Comparison of simulated and measured cutting forces for external helix gear, one-pass, AISI 8620 steel process.



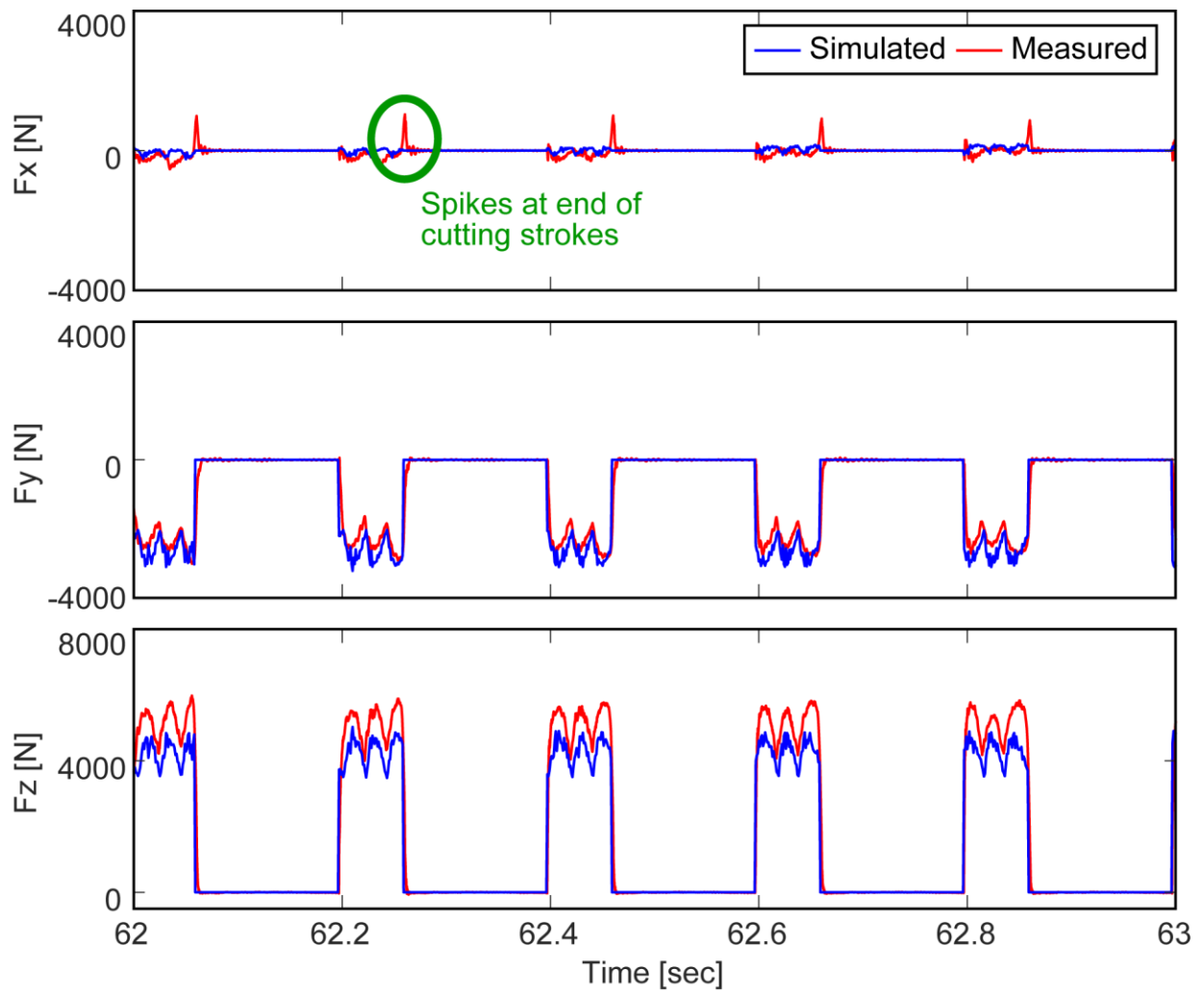


**Figure 4.42:** Comparison of simulated and measured cutting forces for external helix gear, one-pass, AISI 8620 steel process, zoomed in.

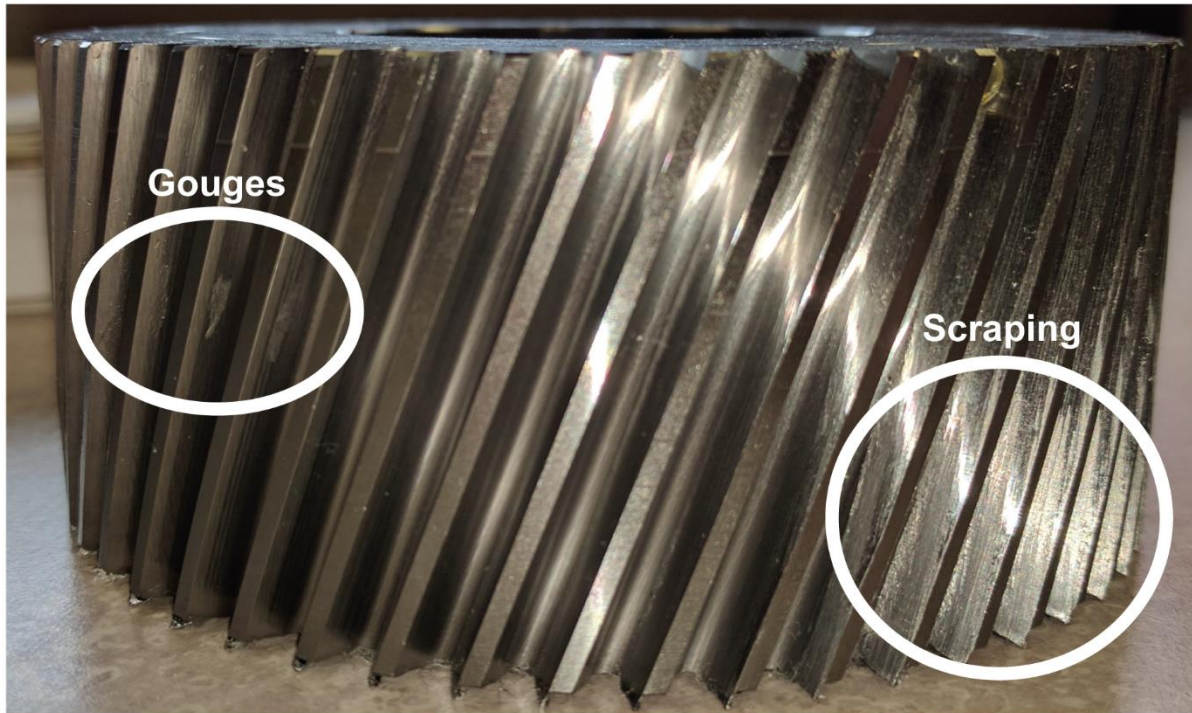


**Figure 4.43:** Gouges and scraping as seen on the finished external helix gear, one-pass process.

#### 4.6.3.8 External Helix Gear, Two-Pass, AISI 8620 Steel

Figure 4.44 and Figure 4.45 shows the simulated and measured cutting forces for the external helical gear, two-pass process. Similar trends can be seen for each of the passes as with the helical one-pass process. There is error in the magnitude of the  $z$  (although less than the one-pass process which could be due to the decreased rotary feedrate), and there are similar spikes in the forces at the end of the cutting strokes in the  $x$  and  $y$  directions. The finishing pass shows good correlation in all three directions and does not have the spikes in the  $x$  and  $y$  directions. Table 4.13 gives the RMS error and percentage for each of the passes.

**Table 4.13:** RMS error for external helix gear, two-pass, AISI 8620 steel process.

	$E_x$ [N]	$E_y$ [N]	$E_z$ [N]
Roughing Pass	137 (6.2%)	155 (6.7%)	338 (8.7%)
Finishing Pass	13.8 (8.7%)	12.0 (7.6%)	20.6 (7.1%)

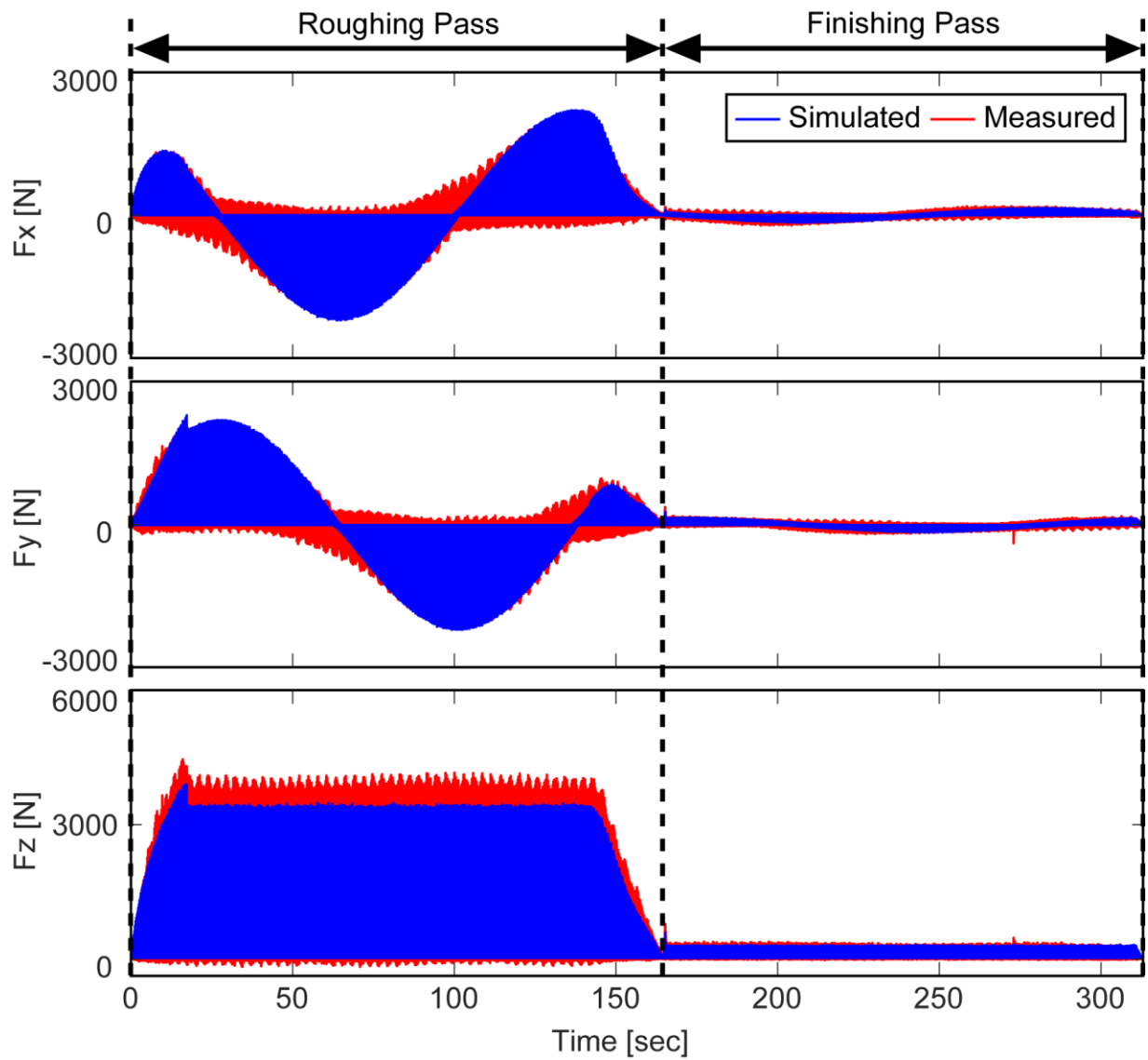


**Figure 4.44:** Comparison of simulated and measured cutting forces for external helix gear, two-pass, AISI 8620 steel process.

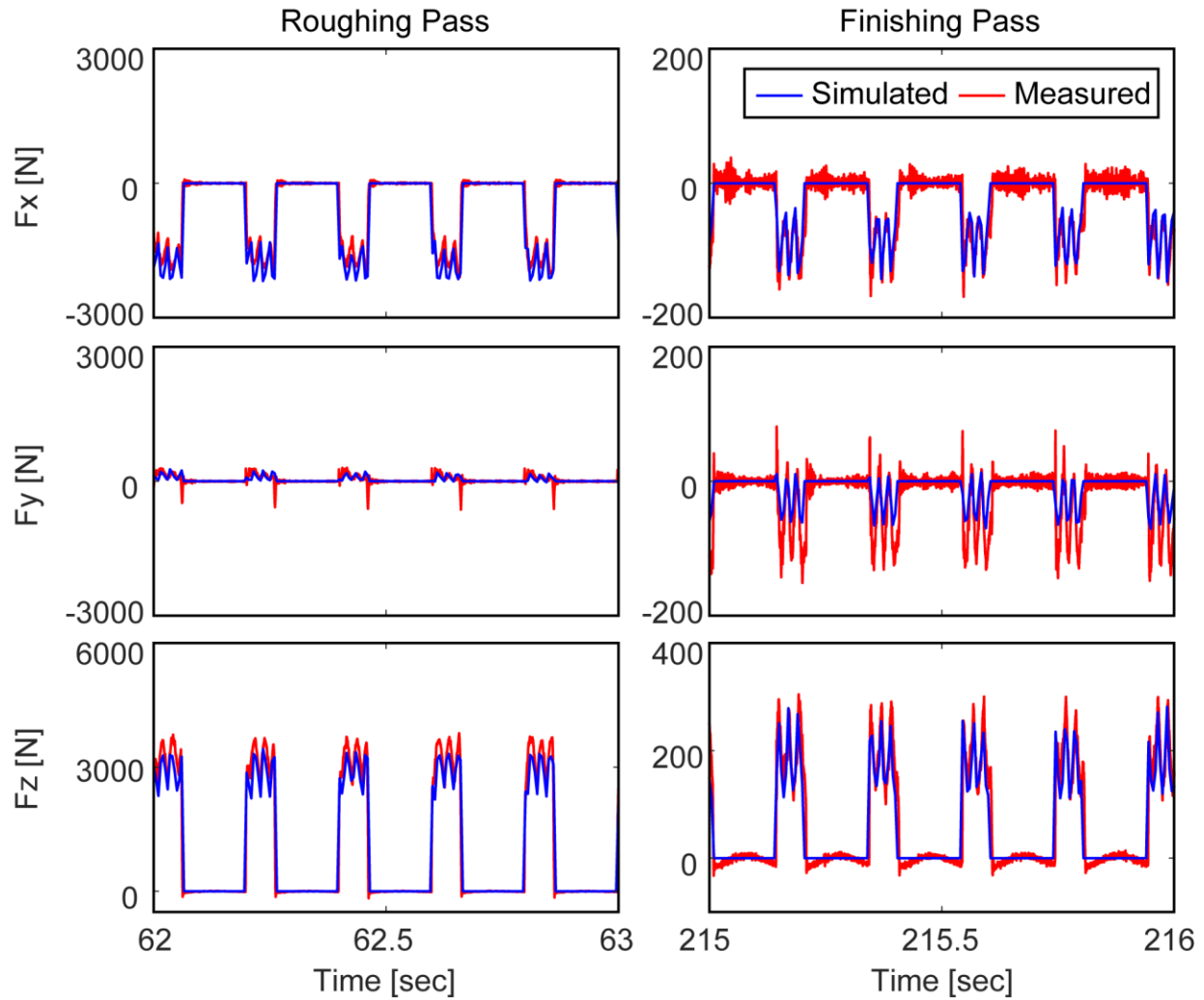


**Figure 4.45:** Comparison of simulated and measured cutting forces for external helix gear, two-pass, AISI 8620 steel process, zoomed in.

## 4.7 Conclusions

In this chapter, an algorithm to predict the cutting forces in gear shaping was presented. The cutting edge is discretized into nodes with varying cutting directions (tangential, feed, and radial), local inclination angle, and local rake angle. Each node represents an oblique cutting force model and, if engaged in cutting, contributes a three dimensional cutting force vector. The cutter-workpiece engagement is calculated using a dixel based modeller called ModuleWorks at discrete time steps. From the cutter-workpiece engagement, the two-dimensional chip geometry is reconstructed using the alpha shape method and the area of the

triangles constitute the undeformed chip area for the time step. Several case studies were used to experimentally verify the cutting force prediction which included an internal spur gear, external spur gear, and external helical gear. Each gear was manufactured with two different processes (a single pass process and a two-pass process with a roughing and finishing pass). Using a 3-axis dynamometer mounted on the gear workpiece table, experimental cutting forces were recorded for each case and compared against simulated forces. The simulated cutting forces show very good correlation with the measured forces, with the most discrepancy occurring in the helical external gear case. It is hypothesized that these discrepancies are due to rubbing of the tool during cutting, tool wear, and differing cutting speed compared to the process for which the cutting coefficients were calibrated.

## Chapter 5

### Elastic Deformation and Form Error Prediction

#### 5.1 Introduction

Due to cutting forces, the tool and/or workpiece in any machining operation will elastically deform away from their nominal position, which results in extra material being left on the surface. This deflection of the tool relative to the workpiece is one of the major contributors to dimensional part inaccuracies in machining. In this chapter, the elastic deflection and its effect on the machined gear's quality is investigated. Furthermore, using a developed virtual gear measurement module, the effect of tool deflection on the gear's profile deviation is examined. Profile deviations can cause transmission error, vibrations, and noise during gear operation [72], therefore it is important to study and mitigate sources of profile error in gear manufacturing. In the remainder of this chapter, Section 5.2 describes the elastic deformation model, Section 5.3 briefly describes the developed virtual gear measurement module, and Section 5.3.1 shows experimental validation of predicted profile deviation.

#### 5.2 Elastic Deformation Model

In this study, the gear shaper is modelled as an elastic beam as depicted in Figure 5.1. The stiffness of the tool is characterized at the bottom of the tool in the  $x$  and  $y$  direction ( $K_x$  and  $K_y$ ). Since cutting in gear shaping only occurs at the bottom of the cutter, only the bottom of the cutter is characterized. The stiffness in the  $z$  direction is assumed rigid. Then, based on the predicted cutting forces, the deflection of the tool is calculated and a feedback loop is established which adds the deflection of the tool from the previous time step to the current time step.

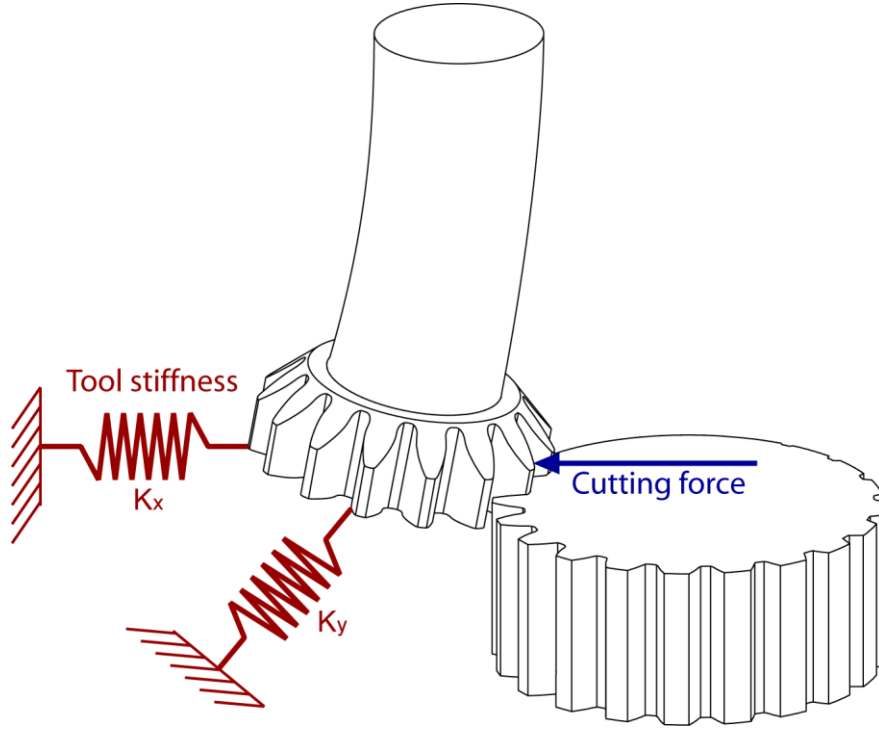


**Figure 5.1:** Elastic deformation of cutting tool due to cutting forces.

### 5.2.1 Impact Hammer Testing

To obtain an estimate of the tool's stiffness, the vibratory dynamics at the bottom of the tool are identified through impact hammer testing which obtains the frequency response of the system. The acceleration of the system (acceleration per force) can be considered a summation of second order systems (modes) [73]:

$$A(\omega) = \frac{\ddot{X}(\omega)}{F(\omega)} = \sum_{i=1}^N \frac{-(\omega/\omega_{ni})^2 K_i}{1 - (\omega/\omega_{ni})^2 + j2\zeta_i(\omega/\omega_{ni})} \quad (5.1)$$

Here,  $N$  is the number of vibration modes,  $\omega_{ni}$  is the mode's natural frequency,  $\zeta_i$  is the mode's damping ratio, and  $K_i = \omega_{ni}^2/k_i$  is the mode's contribution factor where  $k_i$  is the mode's stiffness. This frequency response function (FRF) can also be rewritten as the receptance (displacement per force) [73]:

$$R(\omega) = \frac{X(\omega)}{F(\omega)} = \frac{A(\omega)}{-\omega^2} = \sum_{i=1}^N \frac{(1/k_i)}{1 - (\omega/\omega_{ni})^2 + j2\zeta_i(\omega/\omega_{ni})} \quad (5.2)$$

From this form, the static stiffness of the system  $K_{\text{static}}$  (i.e. inverse of the receptance at zero frequency) can be approximated as the inverse of the sum of each mode's inverse stiffness:

$$K_{\text{static}} = \frac{1}{R(0)} = 1 / \sum_{i=1}^N \frac{1}{k_i} \quad (5.3)$$

Using an accelerometer and impact hammer, the accelerance FRF is experimentally measured in the machine's  $x$  and  $y$  directions. Then, using CUTPRO® software's modal analysis module, numerous modes are fit to the experimentally measured FRF. This is seen in Figure 5.2 for the 5.08 module spur gear shaper used in the external spur gear case studies. In total, 9 modes are fit in the  $x$  direction and 7 modes are fit in the  $y$  direction which can be found in Table 5.1 and Table 5.2, respectively. Negative modes, which show as positive peaks in the imaginary component, are not included in the fit model as they are likely due to rotational (not bending) modes of the tool being activated. Subsequently, the static stiffnesses are calculated based on the fit modes ( $K_x = 33.3$  [N/ $\mu\text{m}$ ] and  $K_y = 39.2$  [N/ $\mu\text{m}$ ]).

Similarly, the FRF of the workpiece has been experimentally measured (Figure 5.3) and 10 modes have been fit in each direction (Table 5.3 and Table 5.4) resulting in static stiffnesses of  $K_{x,wp} = 151$  [N/ $\mu\text{m}$ ] and  $K_{y,wp} = 193$  [N/ $\mu\text{m}$ ]. In the case of this study, the effect of workpiece deformation has not been considered, however given that the workpiece is only about 5x stiffer than the tool, including workpiece deflection may improve the accuracy of the simulation. On the other hand, it is likely that a lot of the compliance in the measured workpiece stiffness is due to the extra fixturing needed to mount the dynamometer on the gear worktable, thus the workpiece in a production process would likely be significantly stiffer.



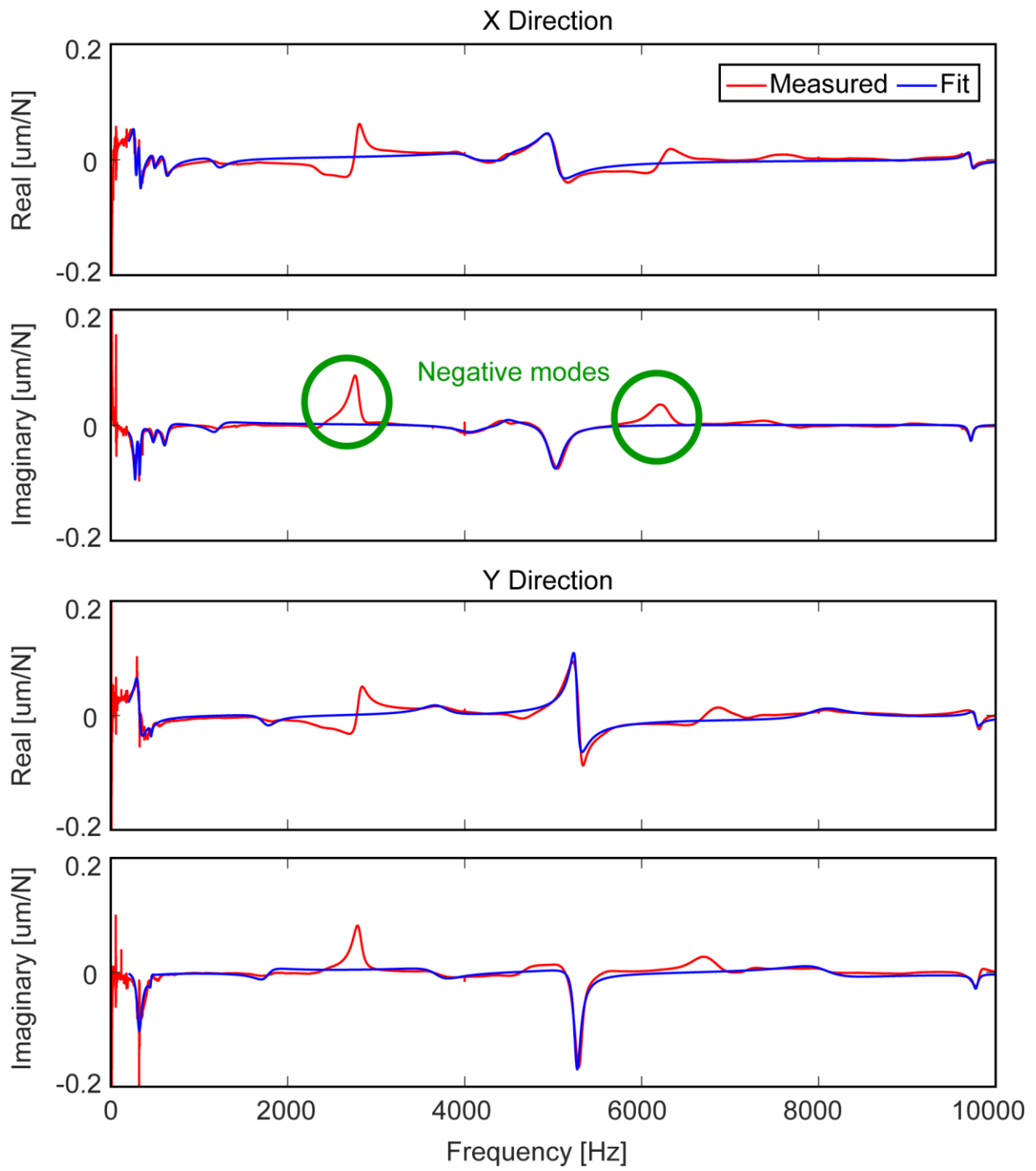


**Figure 5.2:** Measured and fit receptance FRF of the 5.08 module spur gear shaper.

**Table 5.1:** Fit modes and static stiffness in  $x$  direction of 5.08 module spur gear shaper.

Mode	Frequency [Hz]	Damping Ratio [%]	Mass [kg]	Stiffness [N/ $\mu\text{m}$ ]
1	279.3	6.0	32.2	99.0
2	326.9	3.7	37.7	159.1
3	487.7	5.0	44.8	420.6
4	615.9	6.3	14.2	213.0
5	1202.3	7.0	10.1	578.6
6	4088.6	4.8	1.3	836.2
7	4456.9	2.3	3.5	2757.0
8	5016.5	2.0	0.3	318.8
9	9720.8	0.3	1.7	6376.4
<b>Static stiffness:</b>				<b>33.3</b>

**Table 5.2:** Fit modes and static stiffness in  $y$  direction of 5.08 module spur gear shaper.

Mode	Frequency [Hz]	Damping Ratio [%]	Mass [kg]	Stiffness [N/ $\mu\text{m}$ ]
1	320.9	10.0	12.5	50.8
2	452.9	2.7	275.4	2230.5
3	1761.4	5.6	8.4	1034.0
4	3712.0	4.9	2.2	1205.5
5	5265.2	0.9	0.3	349.4
6	8048.3	3.7	0.7	1814.3
7	9777.7	0.3	1.6	6153.1
<b>Static stiffness:</b>				<b>39.2</b>

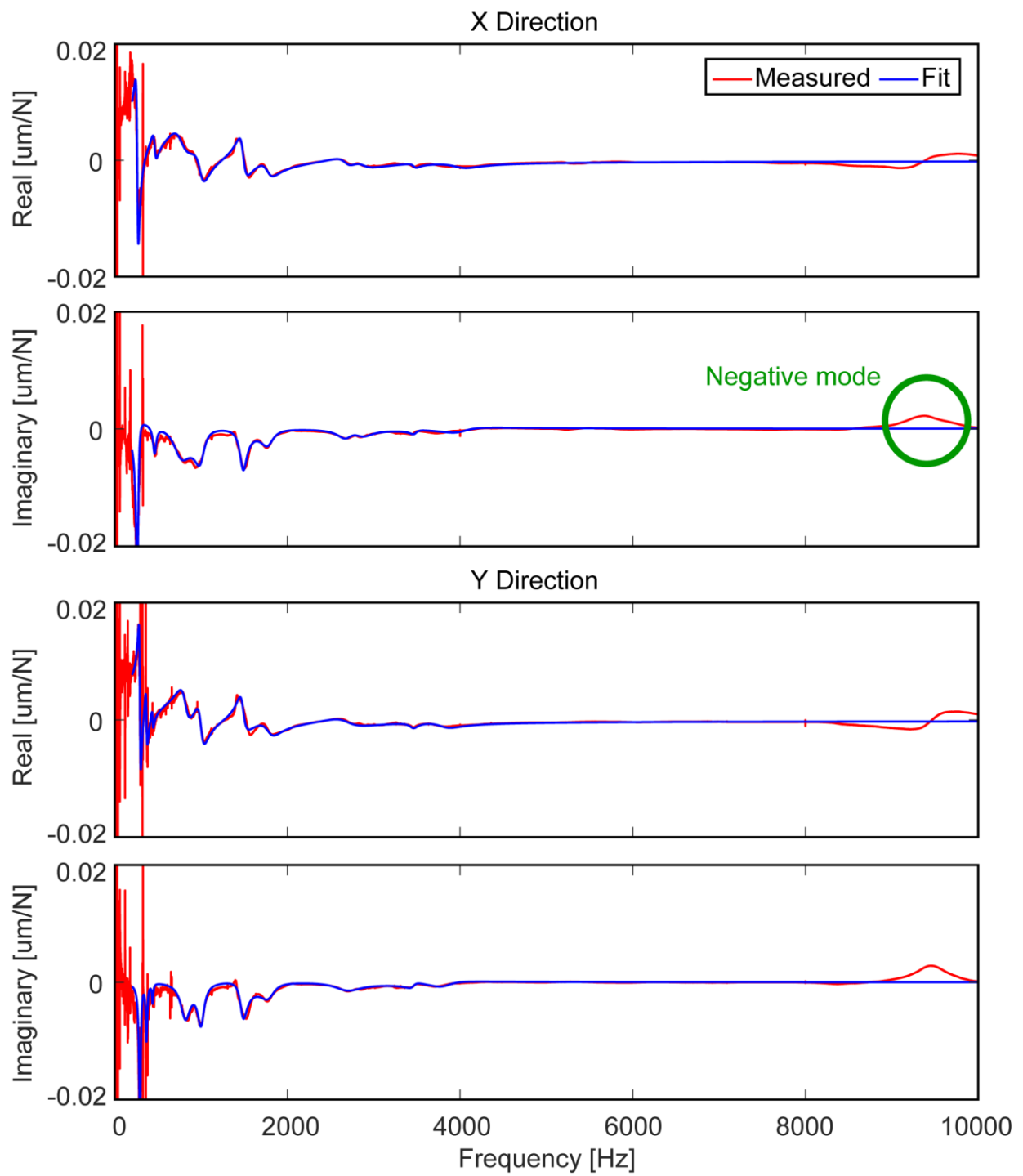


**Figure 5.3:** Measured and fit receptance FRF of the workpiece.

**Table 5.3:** Fit modes and static stiffness in  $x$  direction of workpiece.

Mode	Frequency [Hz]	Damping Ratio [%]	Mass [kg]	Stiffness [N/ $\mu\text{m}$ ]
1	263.3	6.0	114.2	312.5
2	463.0	5.0	260.6	2204.9
3	769.7	15.6	31.7	742.4
4	1000.5	7.0	40.2	1588.8
5	1485.8	3.5	25.0	2180.1
6	1778.1	5.0	32.7	4082.2
7	2685.3	3.8	32.0	9098.7
8	2856.3	4.5	31.3	10088.0
9	3474.3	1.4	148.4	70709.0
10	4011.8	4.9	29.8	18913.0
<b>Static Stiffness</b>				<b>151</b>

**Table 5.4:** Fit modes and static stiffness in  $y$  direction of workpiece.

Mode	Frequency [Hz]	Damping Ratio [%]	Mass [kg]	Stiffness [N/ $\mu\text{m}$ ]
1	292.0	4.0	149.0	501.6
2	368.3	3.0	319.2	1709.3
3	438.3	2.0	1014.2	7690.9
4	821.3	8.3	38.2	1018.4
5	1001.1	4.7	39.4	1558.9
6	1482.0	3.4	32.4	2809.6
7	1792.9	5.7	32.7	4149.4
8	2687.0	6.9	20.3	5791.9
9	3456.8	1.7	306.1	144380.0
10	3820.0	4.3	28.9	16651.0
<b>Static stiffness:</b>				<b>193</b>

### 5.2.2 Deflection Calculation

Using the estimated static stiffness from the modal testing, the deflection of the tool due to the predicted cutting forces can be calculated. Accordingly, a feedback loop is established which adds the deflection calculated at the previous time step to the nominal position of the tool at the current time step:

$$\begin{array}{ccccc} \bar{p}_t & = & \bar{p}'_t & + & \bar{d}_{t-1} \\ \text{actual current} & & \text{nominal current} & & \text{tool deflection} \\ \text{position of tool} & & \text{position of tool} & & \text{at last time step} \end{array} \quad (5.4)$$

Here,  $t$  denoted the current time step, and  $t - 1$  denotes the previous time step. To get the true deflection at the current time step, the simulation would need to iterate through the cutter-workpiece engagement and cutting force calculation (reverting the workpiece geometry each time) until the solution converges, which would be computationally expensive. Therefore, the deflection based off the cutting force at the previous time step is used for the sake of efficiency. To calculate the tool deflection, the cutting force is simply divided by the static stiffness of the tool. However, since the cutting force prediction algorithm calculates the cutting force in the workpiece coordinate system and the modal testing is performed in the machine coordinate system, the cutting force is first transformed into the machine coordinate system:

$$\bar{F}_t^{MCS} = R_{WCS}^{MCS} \bar{F}_t^{WCS} = \begin{bmatrix} \cos \phi_g(t) & -\sin \phi_g(t) & 0 \\ \sin \phi_g(t) & \cos \phi_g(t) & 0 \\ 0 & 0 & 1 \end{bmatrix} \bar{F}_t^{WCS} \quad (5.5)$$

Above,  $\bar{F}_t^{MCS}$  is the cutting force vector in the machine coordinate system,  $\bar{F}_t^{WCS}$  is the cutting force vector in the workpiece coordinate system, and  $R_{WCS}^{MCS}$  is the rotation matrix between the workpiece coordinate system and machine coordinate system. Then, the tool deflection is calculated by elemental division (denoted by  $\oslash$ ) of the cutting force vector and tool stiffness vector ( $\bar{K}^{MCS} = [K_x \ K_y \ K_z]^T = [K_x \ K_y \ \infty]^T$ ):

$$\bar{d}_t^{MCS} = \bar{F}_t^{MCS} \oslash \bar{K}^{MCS} \quad (5.6)$$

Finally, the tool deflection is transformed back into the workpiece coordinate system:

$$\bar{d}_t^{WCS} = [R_{WCS}^{MCS}]^T \bar{d}_t^{MCS} = \begin{bmatrix} \cos \phi_g(t) & \sin \phi_g(t) & 0 \\ -\sin \phi_g(t) & \cos \phi_g(t) & 0 \\ 0 & 0 & 1 \end{bmatrix} \bar{d}_t^{MCS} \quad (5.7)$$

### 5.3 Virtual Gear Measurement

To examine the effect of tool deflection on the gear's quality, a virtual gear measurement module has been developed which is capable of predicting the types of error which are used in industry to classify the quality of gears. There are two main types of error which are considered in gear quality measurement: deviations in the profile curve, and deviations in the lead/helix curve. As depicted in Figure 5.4, the profile curve is the curve on the flank of each tooth on the transverse plane (normally the involute of the base circle), and the lead curve is the curve along the width of each flank which is a straight line for spur gears or a helix for

helical gears. The lead curve is normally evaluated at a diameter halfway between the addendum and dedendum called the tolerance diameter.

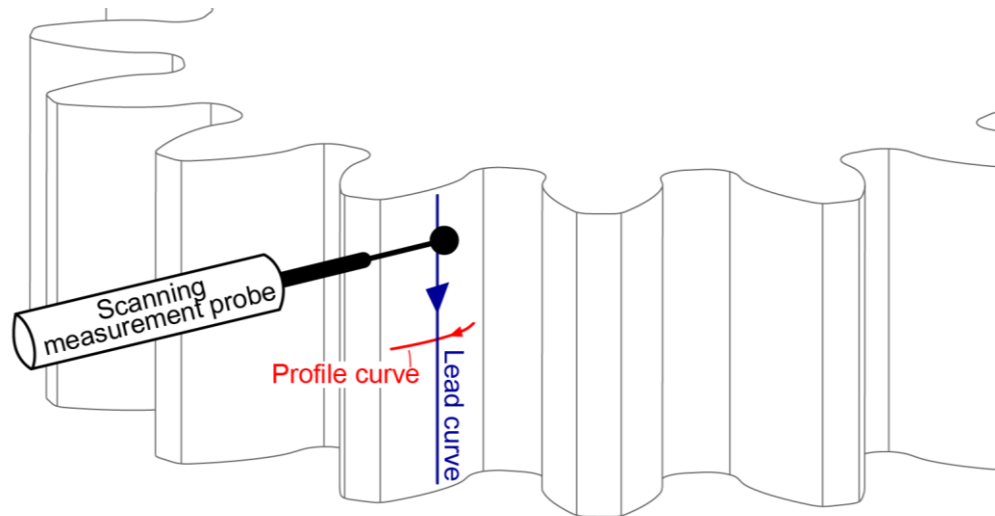


**Figure 5.4:** Scanning measurement of gears.

The ANSI/AGMA 2015-1-A01 standards [74] define several metrics to evaluate profile and lead deviations, which are illustrated in Figure 5.5. After unwrapping the nominal and actual profiles, the total error is defined as the distance between two nominal profiles that completely enclose the actual profile. The form error is defined as the horizontal distance between two mean profiles which enclose the actual profile where the mean profile is the line of best fit of the unwrapped actual profile determined by least squares. The slope error is defined as the horizontal distance between the two points at which the mean profile intersect the evaluation range lines. Finally, the pitch error (illustrated in Figure 5.6) is the error in the position of each flank relative to the corresponding flank of an adjacent tooth, and the index error (not illustrated) is the error in the position of each flank relative to a datum tooth (i.e. the cumulative pitch error). Although only illustrated for profile deviations, total error, form error, and slope error are also metrics used to evaluate lead deviations. By analyzing cross-sections taken from the virtually machined gear in the ModuleWorks engine, the virtual gear measurement module is able to predict the profile deviations, lead deviations, and corresponding metrics.

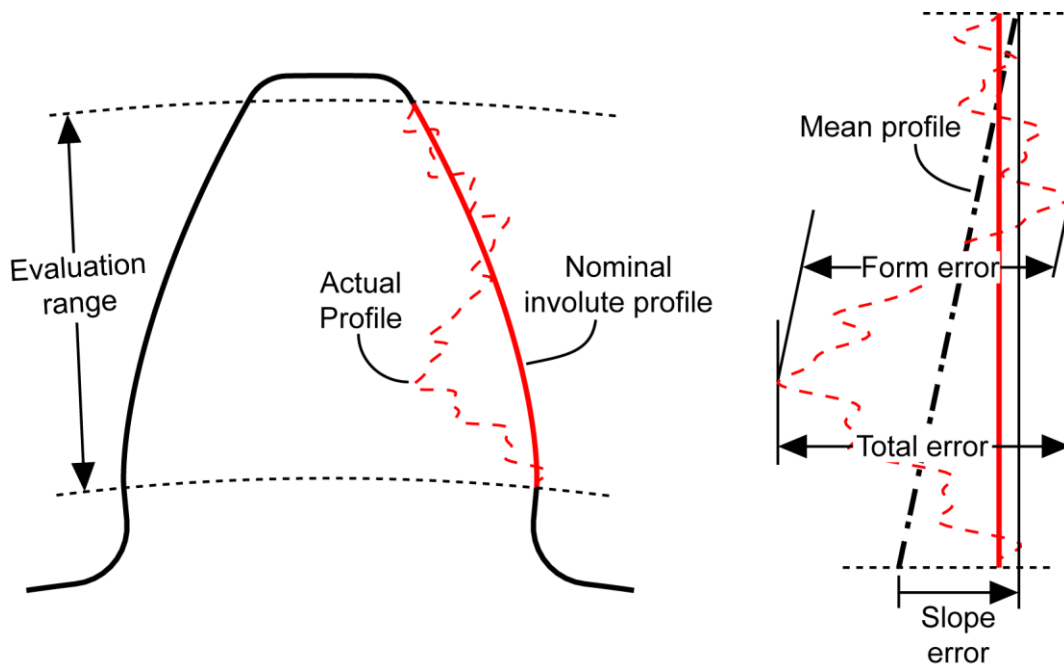


**Figure 5.5:** Profile errors in gear inspection.

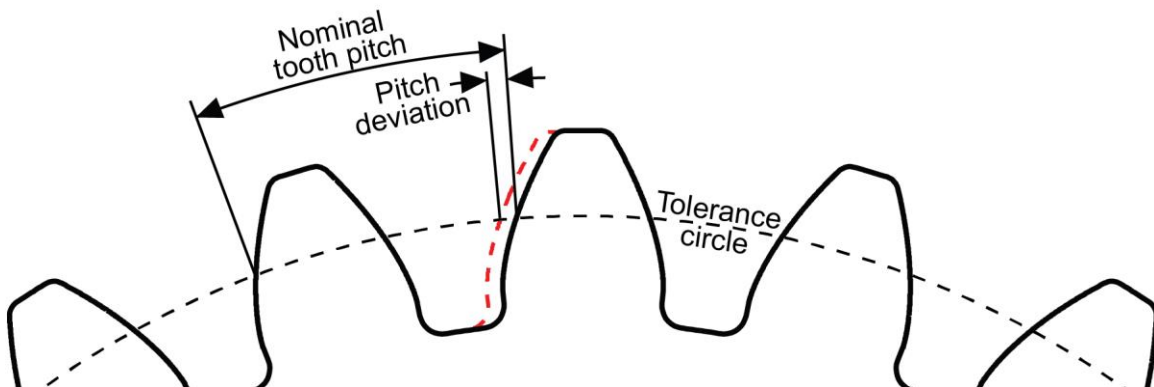


**Figure 5.6:** Pitch deviation in gear inspection.

### 5.3.1 Experimental Validation

In this investigation, the effect of tool deflection is examined on the profile deviations in the external spur gear one-pass and two-pass case studies defined in the previous chapter. In spur gear shaping, lead curve deviations are usually not prominent due to the nature of the process unless the rotary feed is set exceptionally high, there are chatter vibrations, or the workpiece is not clamped flatly. Therefore, profile deviations is the focus of this study. Figure 5.8 to Figure 5.10 show a comparison of simulated and measured

profile deviations in the external spur gear one-pass process for both flanks on the workpiece. Here, the left flank corresponds to the flank which is cut by the leading flank of the tool, and the right flank corresponds to the flank which is cut by the trailing flank of the tool as depicted in Figure 5.7. Simulated profiles are shown for an infinitely rigid tool and a flexible tool as identified in the previous section. The measured profile deviations were determined by measuring a cross-section of the manufactured gear with a coordinate measurement machine (CMM), and then inputting the cross-section through the same virtual gear measurement algorithm.

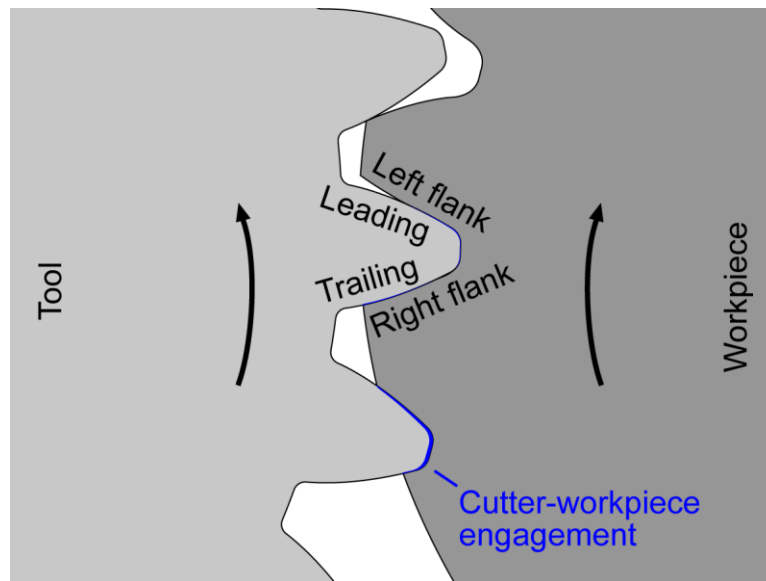


**Figure 5.7:** Leading/left and Trailing/right flank in gear shaping.

It can be seen that there is good correlation in the shape and magnitude of the profile deviations on the left flanks, however there is discrepancy in the prediction of the shapes and magnitudes of the right flanks (particularly for teeth 6-22). Although the simulated tool deflections improve the match between the simulated and measured profiles, there are evidently other major sources of error affecting the measured profiles. The major discrepancies on the right flank show that there is additional material being left on the surface of the machined gear. This suggests that there are likely other deformations occurring during the process which are not being considered in the model. These deformations could include:

- Deformation of individual teeth on the tool: in the current model, the entire tool profile is translated due to cutting forces, however, in reality, each individual tooth on the gear shaper can also deform relative to its adjacent tooth.

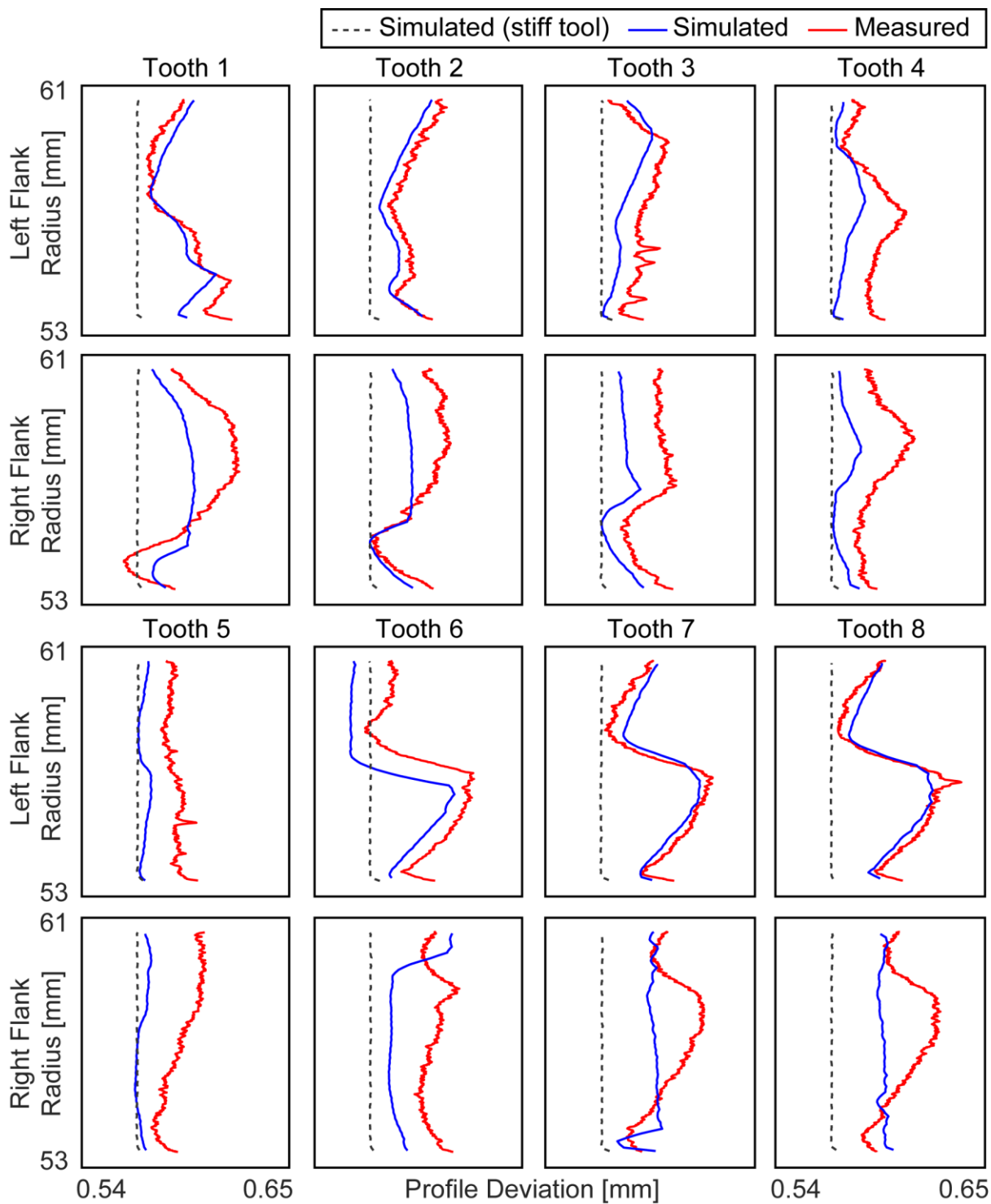


- Rotational deformation of the tool: due to the torque created from the cutting force, the tool post can rotationally deform.
- Workpiece deformations: in the current model, the workpiece is assumed rigid, however, in reality the workpiece will also deform.

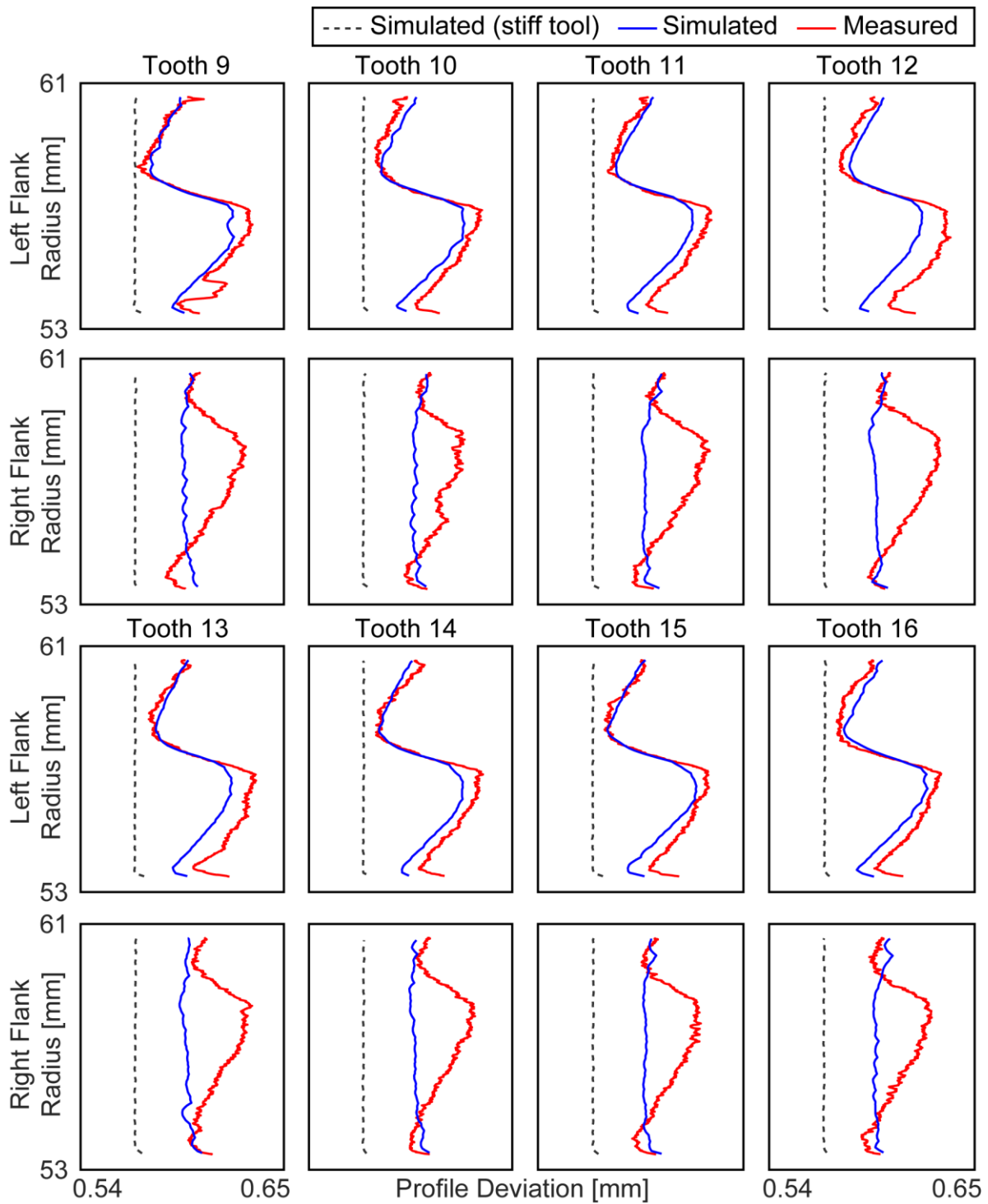
Further development of the model to include these effects may yield more accurate predictions. The overall shift of all flanks of about 0.6 mm shows that the teeth are larger than they nominally should be for a gear of that module. This is due to the nominal center-to-center distance of the process not being set correctly by the technician to properly account for the profile shifting of the tool.

Figure 5.11 gives the total error, form error, slope error, pitch error, and index error for the simulated and measured profile deviations. As expected from qualitatively comparing the profile deviations, the left flank values correlate closely while there are discrepancies in the right flank.

Figure 5.12 to Figure 5.15 show the measured and simulated profile deviations for the two-pass process. As expected, the magnitude of the errors are smaller compared to the one-pass process due to the finishing pass having smaller cutting forces. Similar to the one-pass process, the profile deviations show very good correlations in shape, however there is more discrepancy in the right flanks. The measured index deviations are significantly larger than the simulated index deviations. This could be due to runout of the workpiece when machining the gear, or the part may not have been exactly centered and clamped on the CMM when measuring the cross-section, though the best care was taken to do so.



**Figure 5.8:** Comparison of measured and simulated profile deviations in external spur gear, one-pass process (Teeth 1-8).



**Figure 5.9:** Comparison of measured and simulated profile deviations in external spur gear, one-pass process (Teeth 9-16).

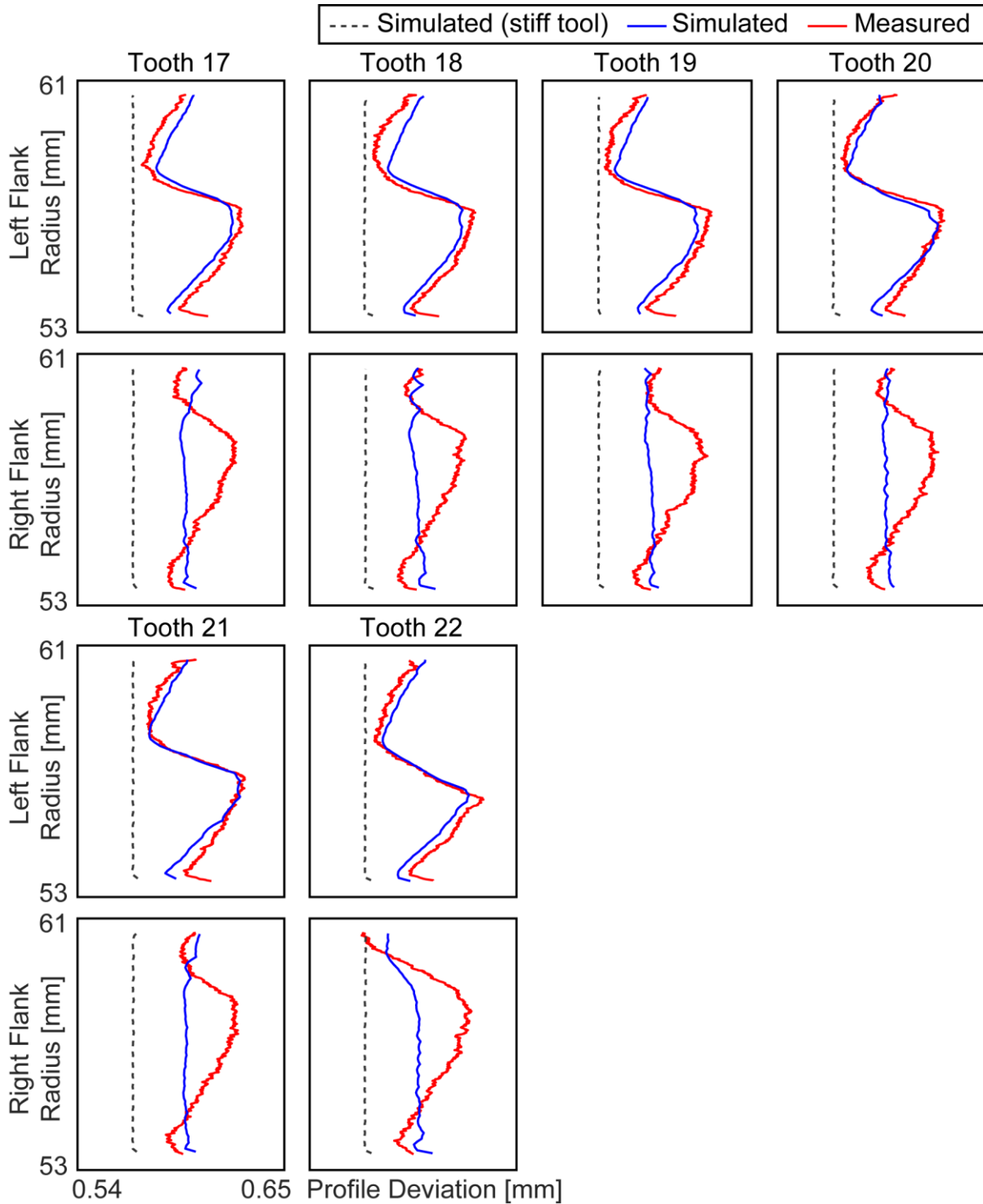


**Figure 5.10:** Comparison of measured and simulated profile deviations in external spur gear, one-pass process (Teeth 17-22).

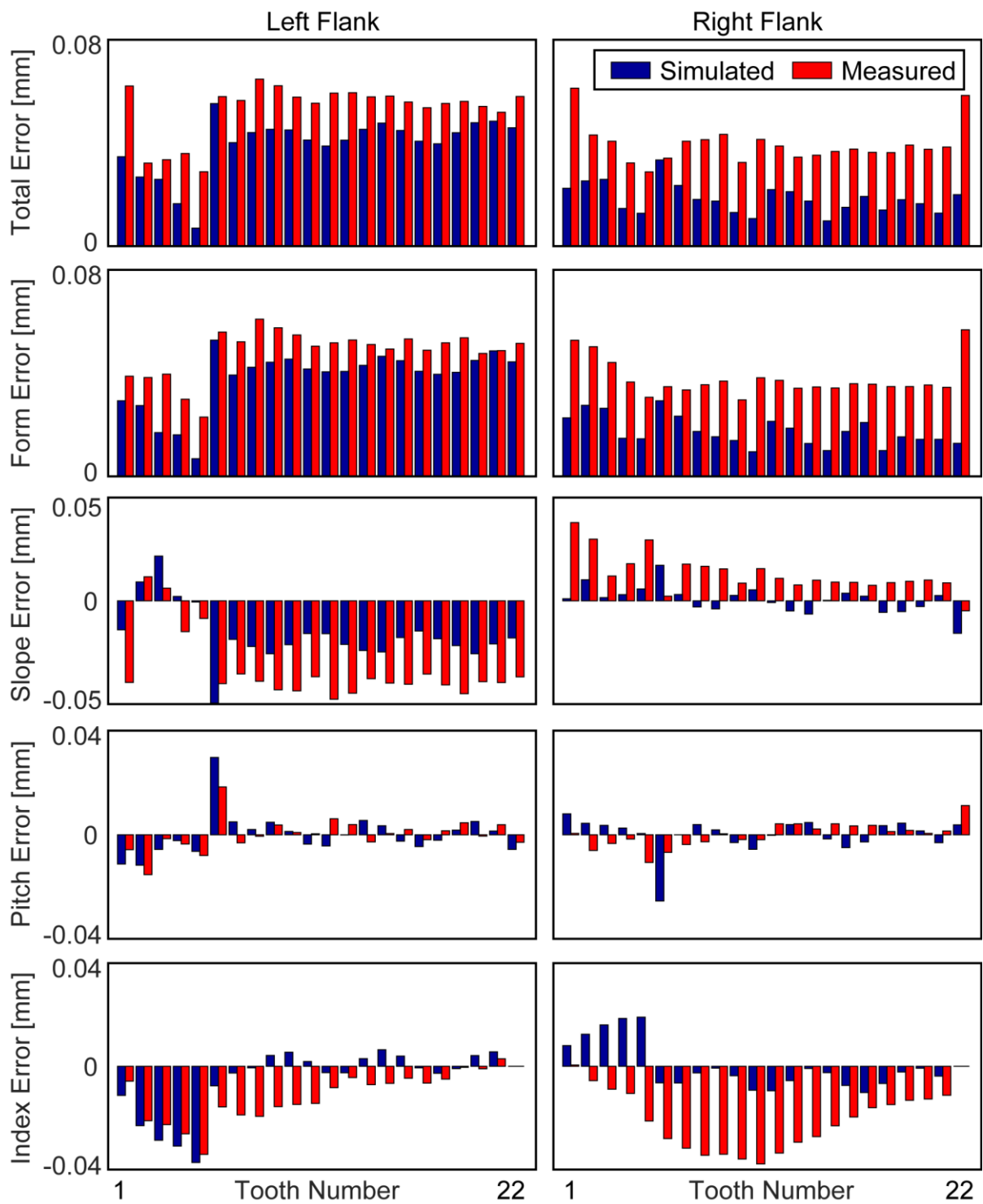


**Figure 5.11:** Measured and simulated profile error metrics in external spur gear, one-pass process.

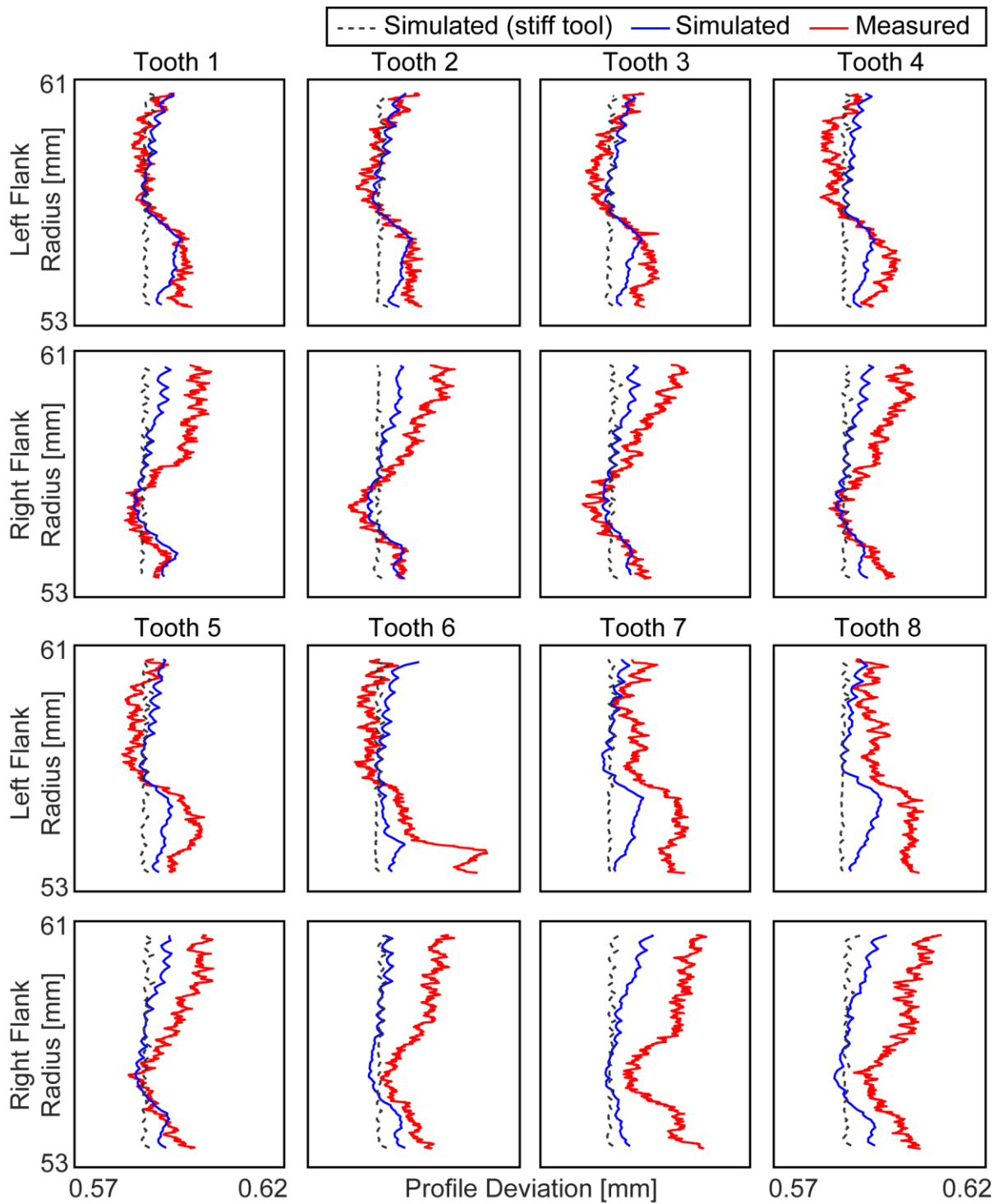


**Figure 5.12:** Comparison of measured and simulated profile deviations in external spur gear, two-pass process (Teeth 1-8).

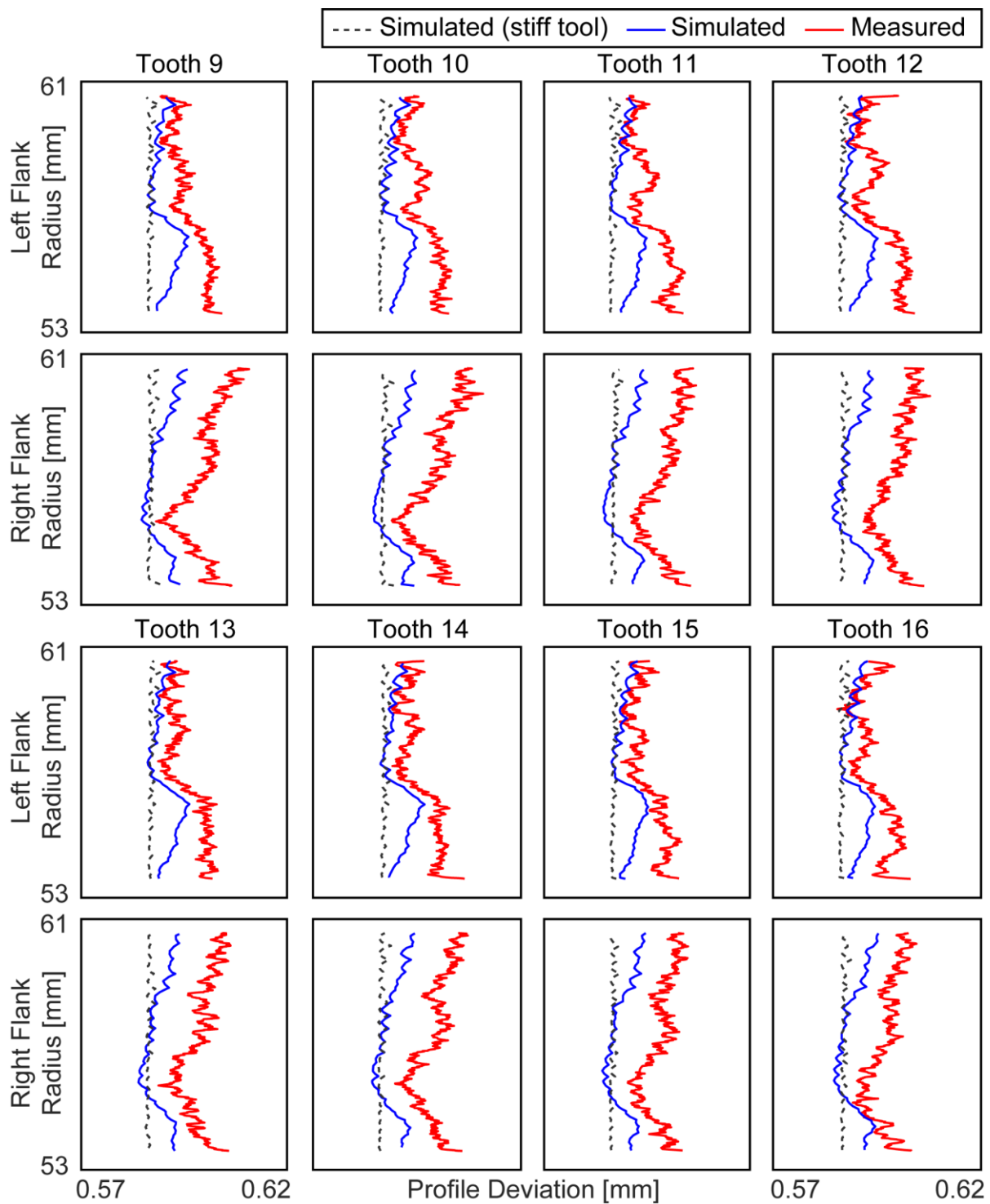


**Figure 5.13:** Comparison of measured and simulated profile deviations in external spur gear, two-pass process (Teeth 9-16).

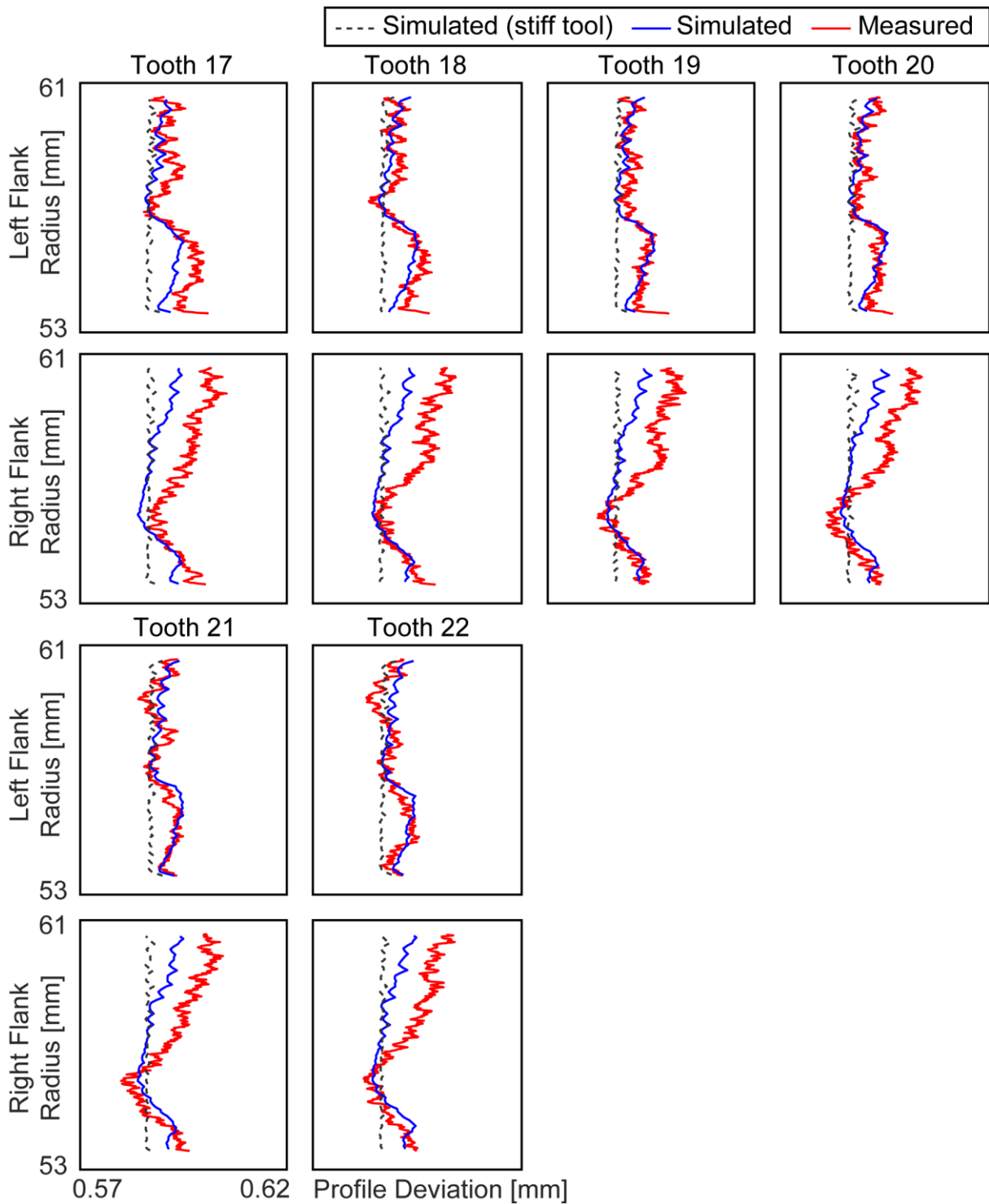


**Figure 5.14:** Comparison of measured and simulated profile deviations in external spur gear, two-pass process (Teeth 17-22).



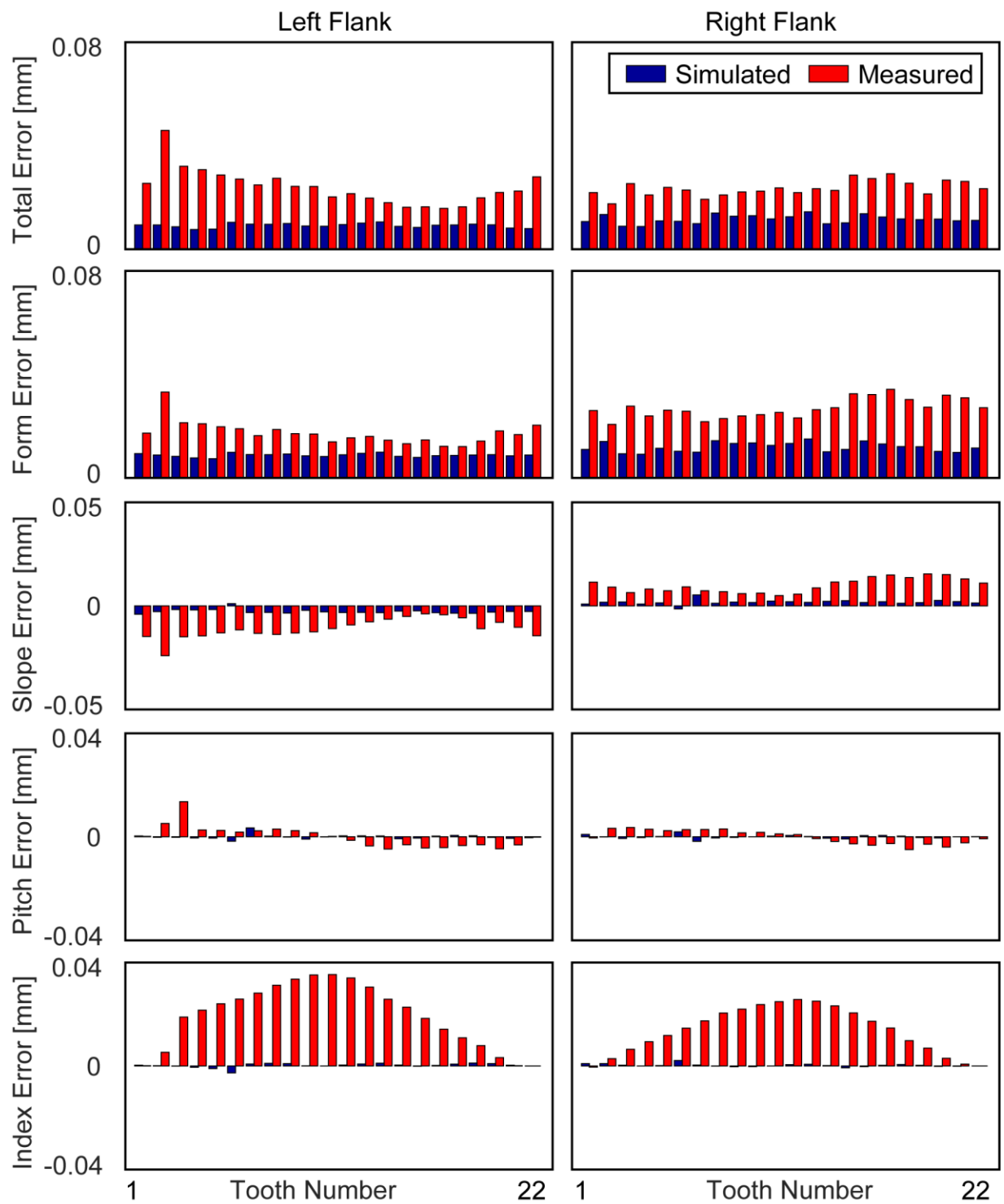


**Figure 5.15:** Measured and simulated profile error metrics in external spur gear, two-pass process.

## 5.4 Conclusions

In this chapter, a model for predicting elastic tool deflection and its effect on profile deviations in gear shaping is presented. The stiffness of the gear shaper is characterized in the machine's  $x$  and  $y$  axis through impact hammer testing. Using the estimated tool stiffness and predicted cutting force, the tool deflection can be calculated. The tool deflection from the previous time step is added to the nominal position of the tool at the current time step to simulate the effect in gear shaping. To investigate the effect of tool deflection on the manufactured gear quality, a virtual gear measurement module is used to evaluate the profile deviations. Measured and simulated profile deviation curves are compared. The simulated profiles show good correlation for the left flanks, however discrepancies can be seen particularly for the right flanks suggesting there are other major sources of dimensional error which is an area of future research. The research presented in this chapter also serves as a basis for future research in vibrations in gear shaping.

# Chapter 6

## ShapePRO Software

### 6.1 Introduction

The algorithms presented in this thesis have been integrated into a program called ShapePRO (Figure 6.1) which is designed to be used by process planners in industry. Similar to MachPro® and CutPro® software (developed by Manufacturing Automation Lab at the University of British Columbia for milling, drilling, and turning), ShapePRO allows planners to virtually machine their parts and then inspect the resulting part quality. This is extremely valuable as process planners waste less machine time and material iterating through process parameter changes to achieve the desired part quality.

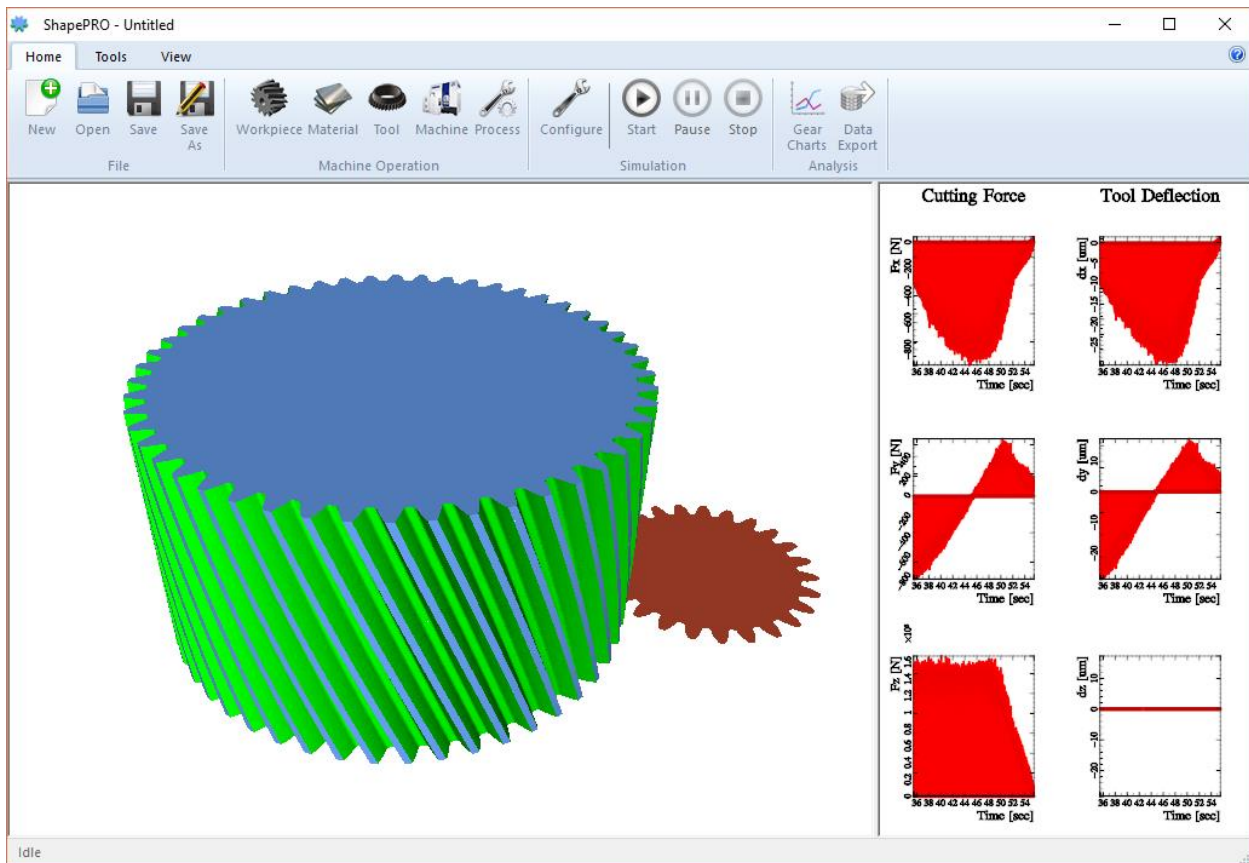
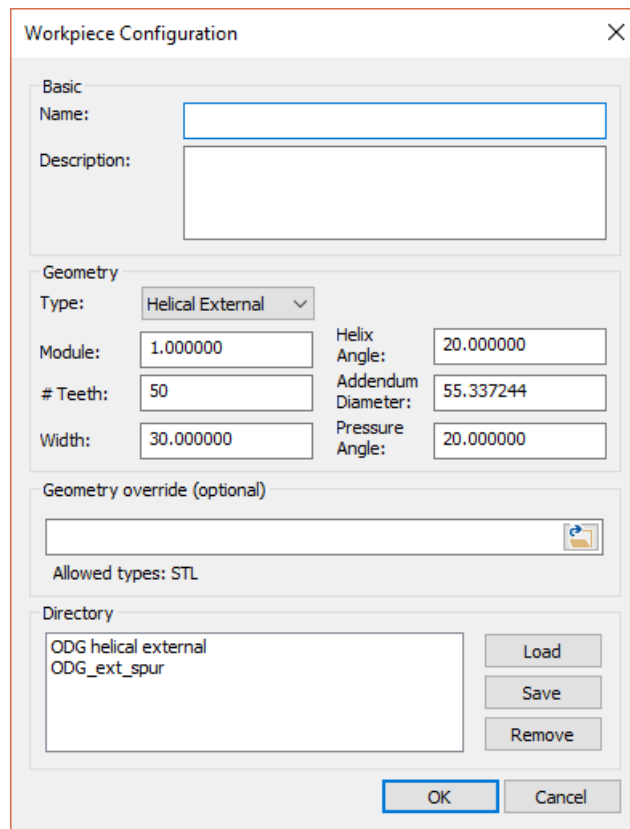


Figure 6.1: ShapePRO software main screen.

## 6.2 User Workflow

The software (developed in C++) integrates with the ModuleWorks engine and is able to calculate the cutter-workpiece engagement, cutting forces, static tool deflections, and (soon) dynamic vibrations. To use the software, the user follows a simple workflow. First, the gear data is set with the workpiece configuration dialog as seen in Figure 6.2. Here, any type of cylindrical gear can be configured and saved in the directory for future use. The software will automatically generate the workpiece geometry (cylinder for external gear or ring for internal gear), however the geometry can also be imported into the software using an STL file.



The screenshot shows the 'Workpiece Configuration' dialog box with the following fields and options:

- Basic:**
  - Name: [Text input field]
  - Description: [Text input field]
- Geometry:**
  - Type: Helical External (dropdown menu)
  - Module: 1.000000
  - # Teeth: 50
  - Width: 30.000000
  - Helix Angle: 20.000000
  - Addendum Diameter: 55.337244
  - Pressure Angle: 20.000000
- Geometry override (optional):**
  - [Text input field with file icon]
  - Allowed types: STL
- Directory:**
  - ODG helical external
  - ODG\_ext\_spur
  - Buttons: Load, Save, Remove
- Buttons:** OK, Cancel

**Figure 6.2:** ShapePRO workpiece configuration dialog.

Next, the workpiece material is set through the material configuration dialog as seen in Figure 6.3. Here, the user may enter the material properties and cutting force coefficients, or the user may pick a material from the material database. The material database has been integrated with the database in CutPro which is very extensive and includes many steels, aluminum, titanium, and other materials. Of course, it is possible to not choose a material and, in this case, only the effect of kinematics is included in the simulation.

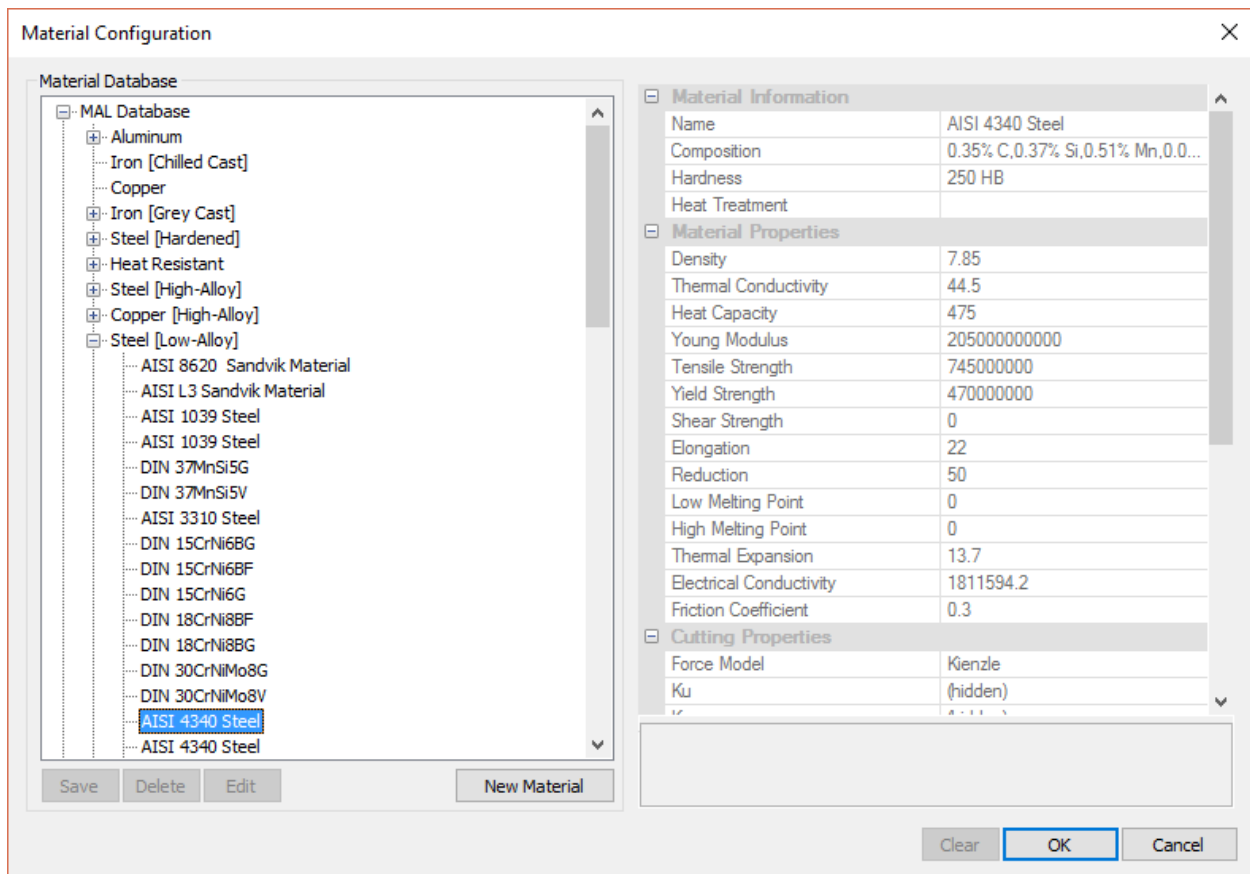


**Figure 6.3:** ShapePRO material configuration dialog.

Next, the tool data and geometry is set with the tool configuration dialog as seen in Figure 6.4. Certain profile modifications can be applied through the software (profile shift, tip fillet, and root fillet), however custom tool geometry may also be imported with an STL, CSV, or TXT file. It is also planned to add other profile modifications such as protuberance and chamfering.

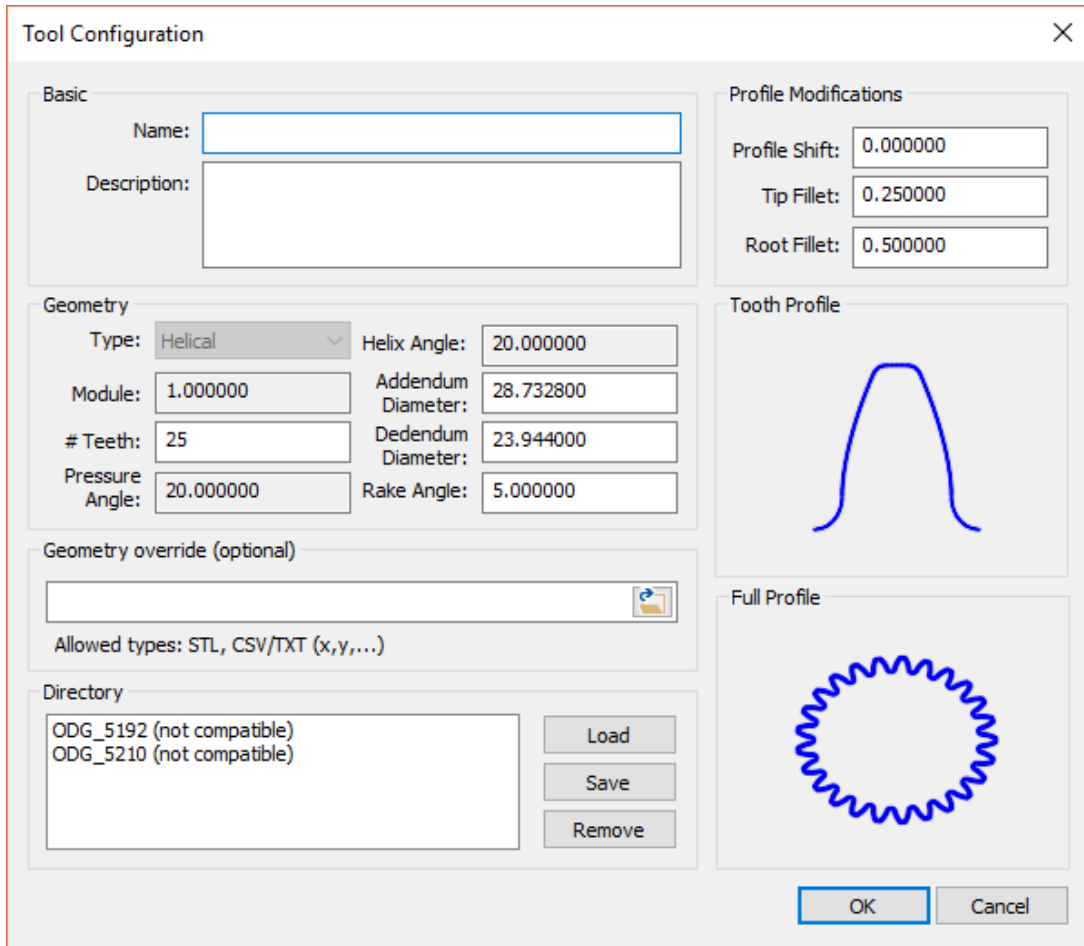


**Figure 6.4:** ShapePRO tool configuration dialog.

Next, the machine properties are entered into the machine configuration dialog as seen in Figure 6.5. Here, the frequency response function of the tool is entered. The modes of the system can be entered manually, imported with a CMP file which is the file type used in CutPro's modal analysis module, or the tool can be set as rigid. In the future, it is planned that the workpiece transfer functions can also be imported to simulate workpiece deformations in gear shaping.

Lastly, the process data is entered in the process configuration dialog as seen in Figure 6.6. Any number of cutting passes can be entered and each pass is configured with its cutting frequency, depth of cut, rotary feed, and radial feed. Additionally, this dialog gives the estimated machine time for each pass and the entire process.

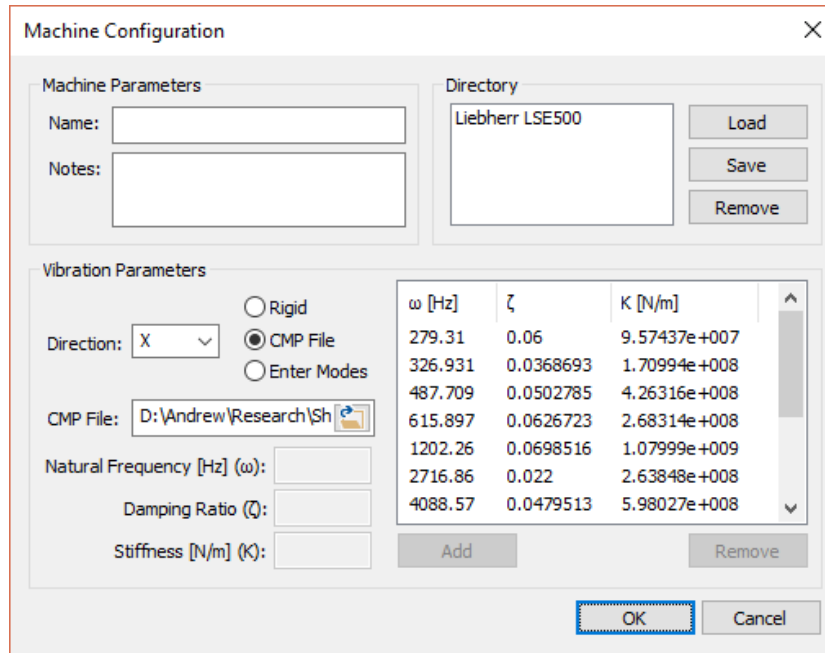


**Figure 6.5:** ShapePRO machine configuration dialog.

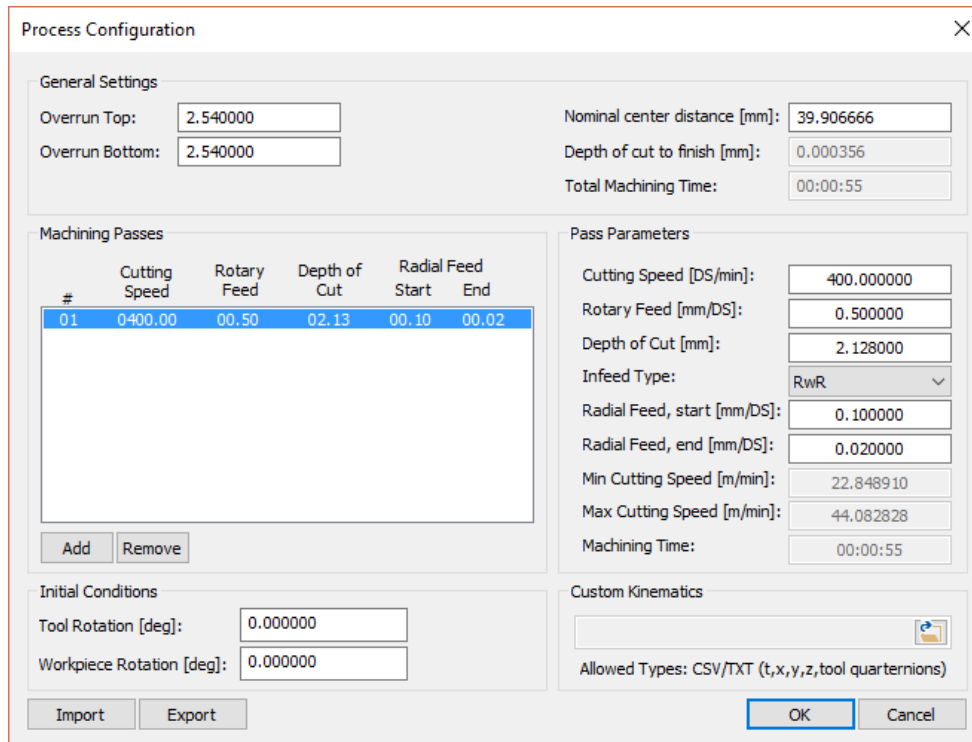


**Figure 6.6:** ShapePRO process configuration dialog.

### 6.3 Virtual Gear Measurement

After the simulation is complete (which usually simulates faster than real-time), then the quality of the machined gear can be inspected using the virtual gear measurement module as seen in Figure 6.7. Here, the profile deviations, lead deviations and pitch deviations can be inspected. Additionally, the module calculates the AGMA quality grade based on the ANSI/AGMA 2015-1-A01 standards [74].

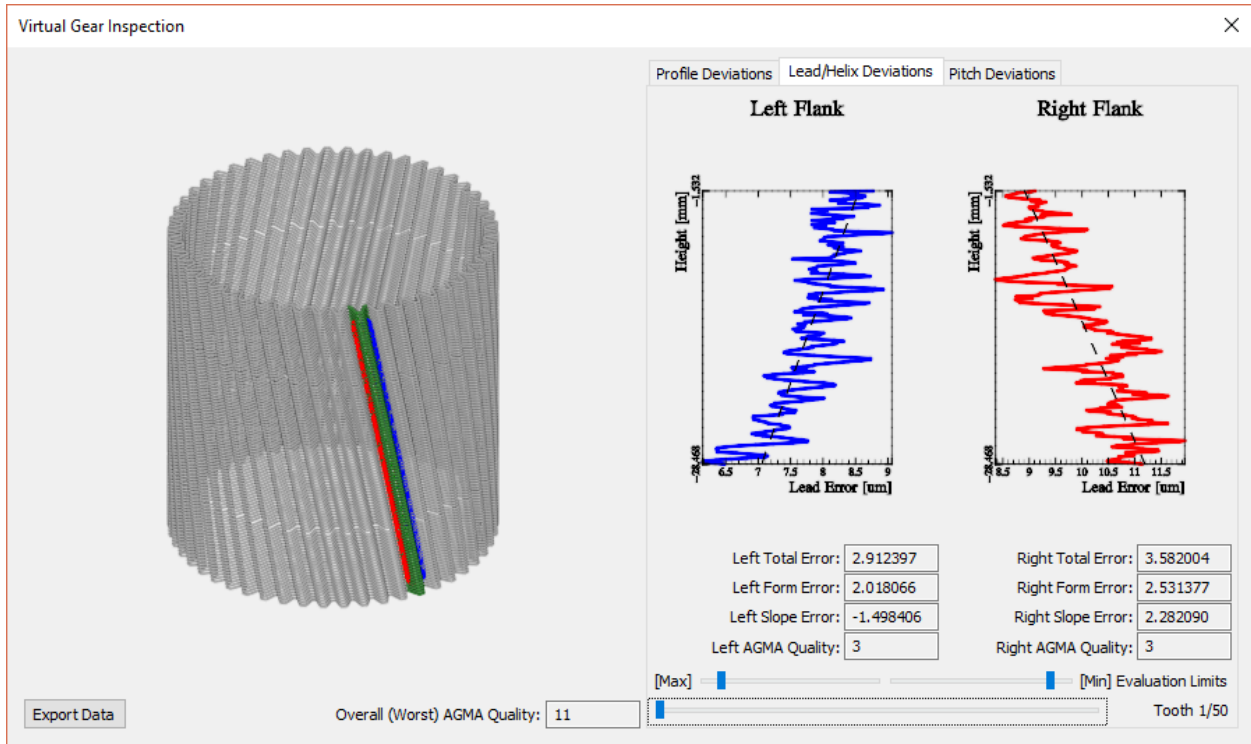


Figure 6.7: ShapePRO virtual gear measurement module.



## Chapter 7

### Conclusions and Future Work

#### 7.1 Conclusions

In this thesis, the three different kinematic components of gear shaping (reciprocating motion, rotary feed, and radial feed) have been mathematically modelled. The kinematic model was then experimentally verified using commanded signals captured from the Siemens 840D controller in a Liebherr LSE500 gear shaping machine. Although it is extremely difficult to model the machine's proprietary kinematic generator exactly, the linear acceleration profile for the radial infeed matched the commanded signal from the machine very closely. The other axes (reciprocating feed, tool rotation, and workpiece rotation) also matched closely, however the nominal feedrates had to be manually adjusted to match the commanded feedrate of the machine. This can be due to various optimizations or parameter rounding effects which take place inside the machine's controller.

Next, a new algorithm to predict the cutting forces in gear shaping was presented. Based on a model of the cutting rake face, the cutting edge is discretized into nodes. Each node represents a generalized oblique cutting force model with its own cutting directions (tangential, feed, and radial), local rake angle, and local inclination angle. At each time step, the cutter-workpiece engagement is calculated using a discrete solid modeller called ModuleWorks. From the cutter-workpiece engagement in dextral form, the two dimensional chip geometry is reconstructed using Delaunay triangulation and alpha shapes. Each triangle in the alpha shape is associated to its closest node and forms the undeformed chip area for that node. Finally, incremental cutting forces are summated along the cutting edge to determine the total cutting force for that time step. To experimentally verify the model, cutting forces were measured on the Liebherr LSE500 gear shaping machine using a 3-axis dynamometer for a variety of processes and gear types. The measured and simulated cutting force profiles match very closely with an RMS error of about 3-10%. The helical gear shaping case showed the most discrepancy. It is hypothesized that the discrepancy may be due to tool rubbing during cutting, tool wear, and larger cutting speeds than the process for which the cutting coefficients were calibrated. More experiments are needed to test the hypothesis.

Lastly, a model for predicting the elastic deformations of the cutting tool was presented. Based on experimentally measured frequency response functions of the machine, the static stiffness of the tool is estimated. Then, the deflection of the tool is calculated by dividing the predicted cutting force with the

static stiffness. The deflection is then added to the nominal position of the tool to simulate tool deflections in gear shaping. The effect of tool deflections on the gear's quality was also investigated by developing a virtual gear measurement module to predict the profile deviation on each of the gear's teeth following established ANSI/AGMA standards. The simulated involute profile deviation showed very good correlation to experimentally measured profiles on one of the flanks, however further research is needed to improve the accuracy of the model for both flanks.

## **7.2 Future Work**

The future work of this project includes further research into sources of profile deviation, and dynamic vibration prediction during gear shaping.

The elastic tool deflection model presented in this thesis was simplistic. The deflection of the tool is added to the entire cutting edge geometry. However, each gear tooth on the cutting edge can deform relative to its adjacent teeth. By modelling each individual tooth as a flexible beam and updating the tool's geometry at each time step, it is hypothesized that better agreement between the simulated and measured profile deviations could be achieved. Furthermore, effects of workpiece deformation could be included in the simulation.

Using the already identified frequency response function of the tool, the dynamic response of the machine could be simulated to predict chatter vibrations in gear shaping. If the natural frequencies of the machine get excited by cutting forces, then the tool will vibrate and leave a wavy surface pattern on the machined part. During the next cutting stroke, the wavy surface pattern will produce an oscillatory cutting force which will further excite the machine's dynamics resulting in chatter vibrations, poor gear quality, and tool wear/breakage. If this effect can be predicted virtually, then process planner will be able to plan their cutting speed, engagement conditions, and feedrates to maximize the potential of the machine more effectively without fear of damaging the tool or machine.

## Bibliography

- [1] F. Klocke and C. Kobialka, "Reducing Production Costs in Cylindrical Gear Hobbing and Shaping," *Gear Technology*, pp. 26-31, March/April 2000.
- [2] F. Klocke and T. Köllner, "Hard Gear Finishing with a Geometrically Defined Cutting Edge," *Gear Technology*, pp. 24-29, November/December 1999.
- [3] E. Armarego and M. Uthaichaya, "A mechanics of cutting approach for force prediction in turning operations," *Journal of Engineering Production*, vol. 1, no. 1, pp. 1-18, 1977.
- [4] R. G. Reddy, S. G. Kapoor and R. E. DeVor, "A Mechanistic Force Model for Contour Turning," *Journal of Manufacturing Science and Engineering*, vol. 122, no. 3, pp. 398-405, 1997.
- [5] R. Meyer, J. Köhler and B. Denkena, "Influence of the tool corner radius on the tool wear and process forces during hard turning," *The International Journal of Advanced Manufacturing Technology*, vol. 58, no. 9, pp. 933-940, 2012.
- [6] Y. Altintas and P. Lee, "A general mechanics and dynamics model for helical end mills," *CIRP Annals - Manufacturing Technology*, vol. 45, no. 1, pp. 59-64, 1996.
- [7] E. Budak, Y. Altintas and A. Armarego, "Prediction of Milling Force Coefficients From Orthogonal Cutting Data," *Journal of Manufacturing Science and Engineering*, vol. 118, no. 2, pp. 216-224, 1994.
- [8] O. Omar, T. El-Wardany and M. Elbestawi, "An improved cutting force and surface topography prediction model in end milling," *International Journal of Machine Tools and Manufacture*, vol. 47, no. 7-8, pp. 1263-1275, 2007.
- [9] M. R. Khoshdarregi and Y. Altintas, "Generalized modeling of chip geometry and cutting forces in multi-point thread turning," *International Journal of Machine Tools and Manufacture*, vol. 98, pp. 21-32, 2015.
- [10] V. Chandrasekharan, S. Kapoor and R. DeVor, "A Mechanistic Model to Predict the Cutting Force System for Arbitrary Drill Point Geometry," *Journal of Manufacturing Science and Engineering*, vol. 120, no. 3, pp. 563-570, 1998.

- [11] L. López de Lacalle, A. Rivero and A. Lamikiz, "Mechanistic model for drills with double point-angle edges," *The International Journal of Advanced Manufacturing Technology*, vol. 40, no. 5, pp. 447-457, 2009.
- [12] J. Sutherland, E. Salisbury and F. Hoge, "A model for the cutting force system in the gear broaching process," *International Journal of Machine Tools and Manufacture*, vol. 37, no. 10, pp. 1409-1421, 1997.
- [13] O. Ozturk and E. Budak, "Modeling of broaching process for improved tool design," in *ASME International Mechanical Engineering Congress*, Washington, 2003.
- [14] B. Imani, M. Sadeghi and M. Elbestawi, "An improved process simulation system for ball-end milling of sculptured surfaces," *International Journal of Machine Tools and Manufacture*, vol. 38, no. 9, pp. 1089-1107, 1998.
- [15] S. D. Merdol and Y. Altintas, "Virtual cutting and optimization of three-axis milling processes," *International Journal of Machine Tools and Manufacture*, vol. 48, no. 10, pp. 1063-1071, 2008.
- [16] A. D. Spence, F. Abrari and M. Elbestawi, "Integrated solid modeller based solutions for machining," *Computer-Aided Design*, vol. 32, no. 8-9, pp. 553-568, 2000.
- [17] E. Budak, E. Ozturk and L. Tunc, "Modeling and simulation of 5-axis milling processes," *CIRP Annals - Manufacturing Technology*, vol. 58, no. 1, pp. 347-350, 2009.
- [18] A. Hosseini and H. Kishawy, "Parametric simulation of tool and workpiece interaction in broaching operation," *International Journal of Manufacturing Research*, vol. 8, no. 4, pp. 422-442, 2013.
- [19] H. Müller, T. Surmann, M. Stautner and K. Weinert, "Online Sculpting and Visualization of Multi-Dexel Volumes," in *Proceedings of the Eighth ACM Symposium on Solid Modeling and Applications*, Seattle, 2003.
- [20] E. Budak and Y. Altintas, "Peripheral milling conditions for improved dimensional accuracy," *International Journal of Machine Tools and Manufacture*, vol. 34, no. 7, pp. 907-918, 1994.
- [21] E. Budak and Y. Altintas, "Modeling and avoidance of static form errors in peripheral milling of plates," *International Journal of Machine Tools and Manufacture*, vol. 35, no. 3, pp. 459-476, 1995.

- [22] A.-V. Phan, L. Baron, J. Mayer and G. Cloutier, "Finite element and experimental studies of diametral errors in cantilever bar turning," *Applied Mathematical Modelling*, vol. 27, no. 3, pp. 221-232, 2003.
- [23] S. Tobias, *Machine Tool Vibrations*, New York: J. Wiley, 1965.
- [24] J. Tlustý and M. Poláček, "The stability of machine tools against self-excited vibrations in machining," *International research in production engineering*, ASME, pp. 465-475, 1963.
- [25] H. Merritt, "Theory of Self-Excited Machine-Tool Chatter," *Journal of Engineering for Industry*, vol. 87, no. 4, pp. 447-454, 1965.
- [26] J. Tlustý, W. Zaton and F. Ismail, "Stability Lobes in Milling," *CIRP Annals - Manufacturing Technology*, vol. 32, no. 1, pp. 309-313, 1983.
- [27] Y. Altintas and E. Budak, "Analytical Prediction of Stability Lobes in Milling," *CIRP Annals - Manufacturing Technology*, vol. 44, no. 1, pp. 357-362, 1995.
- [28] F. Abrari, M. Elbestawi and A. Spence, "On the dynamics of ball end milling: modeling of cutting forces and stability analysis," *International Journal of Machine Tools and Manufacture*, vol. 38, no. 3, pp. 215-237, 1998.
- [29] Y. Altintas and J. Ko, "Chatter Stability of Plunge Milling," *CIRP Annals - Manufacturing Technology*, vol. 55, no. 1, pp. 361-364, 2006.
- [30] K. Ahmadi and F. Ismail, "Machining chatter in flank milling," *International Journal of Machine Tools and Manufacture*, vol. 50, no. 1, pp. 75-85, 2010.
- [31] E. Budak and E. Ozlu, "Analytical Modeling of Chatter Stability in Turning and Boring Operations: A Multi-Dimensional Approach," *CIRP Annals - Manufacturing Technology*, vol. 56, no. 1, pp. 401-404, 2007.
- [32] D. Axinte, "An experimental analysis of damped coupled vibrations in broaching," *International Journal of Machine Tools and Manufacture*, vol. 47, no. 14, pp. 2182-2188, 2007.
- [33] C. Brecher, F. Klocke, M. Brumm and A. Hardjosuwito, "Simulation based model for tool life prediction in bevel gear cutting," *Production Engineering*, vol. 7, no. 2, pp. 223-231, 2013.

- [34] C. Brecher, M. Brumm and F. Hübner, "Approach for the Calculation of Cutting Forces in Generating Gear Grinding," *Procedia CIRP*, vol. 33, pp. 287-292, 2015.
- [35] F. Klocke and T. Schröder, "Gear Shaving—Process Simulation Helps to Comprehend an Incomprehensible Process," *Gear Technology*, pp. 46-54, September 2006.
- [36] F. Klocke, C. Gorgels, R. Schalaster and A. Stuckenberg, "An Innovative Way of Designing Gear Hobbing Processes," *Gear Technology*, pp. 48-53, May 2012.
- [37] F. Klocke, C. Gorgels and A. Stuckenberg, "Investigations on Surface Defects in Gear Hobbing," *1st CIRP Conference on Surface Integrity (CSI)*, vol. 19, pp. 196-202, 2011.
- [38] F. Klocke, C. Brecher, C. Löpenhaus and M. Krömer, "Calculating the workpiece quality using a hobbing simulation," *Proceedings of the 48th CIRP Conference on Manufacturing Systems*, vol. 41, pp. 687-691, 2016.
- [39] N. Tapoglou and A. Antoniadis, "CAD-Based Calculation of Cutting Force Components in Gear Hobbing," *Journal of Manufacturing Science and Engineering*, vol. 134, no. 3, May 2012.
- [40] N. Sabkhi, C. Pelaingre, C. Barlier, A. Moufki and M. Nouari, "Characterization of the cutting forces generated during the gear hobbing process: Spur gear," *15th CIRP Conference on Modelling of Machining Operations*, vol. 31, pp. 411-416, 2015.
- [41] A. Antoniadis, N. Vidakis and N. Bilalis, "FEM Modeling Simulation of Gear Hobbing and Failure Types of Cutting Materials".
- [42] K. D. Bouzakis, O. Friderikos and I. Tsiafis, "FEM-supported simulation of chip formation and flow in gear hobbing of spur and helical gears," *CIRP Journal of Manufacturing Science and Technology*, vol. 1, no. 1, pp. 18-26, 2008.
- [43] X. Dong, C. Liao, Y. Shin and H. Zhang, "Machinability improvement of gear hobbing via process simulation and tool wear predictions," *The International Journal of Advanced Manufacturing Technology*, vol. 86, no. 9, pp. 2771-2779, 2016.

- [44] K. D. Bouzakis, S. Kombogiannis, A. Antoniadis and N. Vidakis, "Gear Hobbing Cutting Process Simulation and Tool Wear Prediction Models," *Journal of Manufacturing Science and Engineering*, vol. 124, no. 1, pp. 42-51, 2001.
- [45] K. -D. Bouzakis, A. Antoniadis, S. Kombogiannis and N. Vidakis, "Modeling of Gear Hobbing-Part II A Computer Supported Experimental-Analytical Determination of the Wear Progress to Optimize the Tool Life Time," *Manufacturing Science and Engineering*, vol. 10, pp. 251-269, 1999.
- [46] C. Fetvaci, "Generation Simulation of Involute Spur Gears Machined by Pinion-Type Shaper Cutters," *Strojniski Vestnik- Journal of Mechanical Engineering*, vol. 56, no. 10, pp. 644-652, September 2010.
- [47] C.-B. Tsay, W.-Y. Liu and Y.-C. Chen, "Spur gear generation by shaper cutters," *Journal of Materials Processing Technology*, vol. 104, no. 3, pp. 271-279, August 2000.
- [48] M. S. Shunmugam, "Profile Deviations in Internal Gear Shaping," *International Journal of Machine Tool Design and Research*, vol. 22, no. 1, pp. 31-39, 1982.
- [49] S.-L. Chang and C.-B. Tsay, "Computerized Tooth Profile Generation and Undercut Analysis of Noncircular Gears Manufactured With Shaper Cutters," *Journal of Mechanical Design*, vol. 120, no. 1, pp. 92-99, 1998.
- [50] W. König and K. Bouzakis, "Chip Formation in Gear-Shaping," *Annals of CIRP*, vol. 26, no. 1, pp. 17-20, 1977.
- [51] P. P. Datta, T. K. Chattopadhyay and R. N. Banerjee, "Computer aided stress analysis of fellow's gear-shaping cutter at different stages of a cutting stroke," *Proceedings of the Institution of Mechanical Engineers Part B Journal of Engineering Manufacture*, vol. 218, no. 10, pp. 1297-1306, October 2004.
- [52] P. Datta, R. Banerjee and T. Chattopadhyay, "Computer aided stress and deflection analysis of Fellow's gear-shaping cutter, for different cutting process parameters," *Proceedings of the Institution of Mechanical Engineers, Part B: Journal of Engineering Manufacture*, vol. 218, no. 12, pp. 1755-1765, 2004.

- [53] F. L. Litvin and A. Fuentes, *Gear Geometry and Applied Theory*, 2nd ed, Cambridge University Press, 2004.
- [54] International Organization for Standardization, *ISO 53:1998, Cylindrical gears for general and heavy engineering -- Standard basic rack tooth profile*, 1998.
- [55] N. C. Ainsworth, "Design Implications for Shaper Cutters," *Gear Technology*, pp. 30-33, July/August 1996.
- [56] Nachi America, "Gear Tools: Shaper Cutter," [Online]. Available: <http://www.nachiamerica.com/p-80/Gear-Tools/Shaper-Cutter/>.
- [57] Star SU, "Gear Shaper Cutters," [Online]. Available: <http://www.star-su.com/cutting-tools/gear-cutting-tools/gear-shapers>.
- [58] K. Erkorkmaz and Y. Altintas, "High speed CNC system design. Part I: jerk limited trajectory generation and quintic spline interpolation," *International Journal of Machine Tools and Manufacture*, vol. 41, no. 9, pp. 1323-1345, 2001.
- [59] Liebherr Group, "LSE 500," [Online]. Available: <https://www.liebherr.com/en/dnk/products/gear-cutting-technology-automation/gear-cutting-machines/gear-shaping-machines/details/lse500.html>.
- [60] Liebherr Group, *LSE Training Manual*, 2013.
- [61] Y. Altintas, *Manufacturing Automation: Metal Cutting Mechanics, Machine Tool Vibrations, and CNC Design*, Cambridge: Cambridge University Press, 2012.
- [62] G. V. Stabler, "The chip flow law and its consequences," in *Proceedings of 5th Machine Tool Design and Research Conference*, 1964.
- [63] O. Kienzle, "Die Bestimmung von Kräften und Leistungen an spänenden Werkzeugen und Werkzeugmaschinen," in *Z-VDI 94*, 1951.
- [64] M. Kaymakci, Z. M. Kilic and Y. Altintas, "Unified cutting force model for turning, boring, drilling and milling operations," *International Journal of Machine Tools & Manufacture*, Vols. 54-55, pp. 34-45, 2012.



- [65] ModuleWorks GmbH, ModuleWorks GmbH, [Online]. Available: <https://moduleworks.com/>.
- [66] M. O. Benouamer and D. Michelucci, "Bridging the gap between CSG and Brep via a triple ray representation," in *SMA '97 Proceedings of the fourth ACM symposium on Solid modeling and applications*, New York, 1997.
- [67] H. Edelsbrunner, D. Kirkpatrick and R. Seidel, "On the shape of a set of points in the plane," *IEEE Transactions on Information Theory*, vol. 29, no. 4, pp. 551-559, 1983.
- [68] M. d. Berg, O. Cheong, M. v. Kreveld and M. Overmars, *Computational Geometry: Algorithms and Applications*, 3rd ed. ed., Santa Clara, CA: Springer-Verlag TELOS, 2008.
- [69] D. Watson, "Computing the n-dimensional Delaunay tessellation with application to Voronoi polytopes," *Computer Journal*, vol. 24, no. 2, pp. 167-172, 1980.
- [70] E. W. Weisstein, "Circumcircle," MathWorld--A Wolfram Web Resource, [Online]. Available: <http://mathworld.wolfram.com/Circumcircle.html>.
- [71] E. W. Weisstein, "Heron's Formula," MathWorld--A Wolfram Web Resource, [Online]. Available: <http://mathworld.wolfram.com/HeronsFormula.html>.
- [72] F. Chaari, T. Fakhfakh, J. Louati and M. Haddar, "Influence of manufacturing errors on the dynamic behavior of planetary gears," *The International Journal of Advanced Manufacturing Technology*, vol. 27, no. 7, pp. 738-746, 2006.
- [73] D. J. Inman, *Engineering Vibration*, Upper Saddle River, NJ: Pearson Education Inc., 2014.
- [74] American Gear Manufacturers Association, *ANSI/AGMA 2015-1-A01, Accuracy Classification System - Tangential Measurements for Cylindrical Gears*, 2002.